PROPERTIES OF THE URANIAN ATMOSPHERE AS REVEALED BY OPTICAL AND INFRARED IMAGING

BY

CHARLES MARTIN WALTER, B.S., M.S.

A Dissertation submitted to the Graduate School

in partial fulfillment of the requirements

for the Degree

Doctor of Philosophy

Major Subject: Astronomy

Minor Subject: Physics

New Mexico State University

Las Cruces, New Mexico

December 1997

"Properties of the Uranian Atmosphere as Revealed by Optical and Infrared Imaging," a dissertation prepared by Charles Martin Walter in partial fulfillment of the requirements for the degree, Doctor of Philosophy, has been approved and accepted by the following:

Timothy J. Pettibone
Dean of the Graduate School

Mark S. Marley
Chair of the Examining Committee

Date

Committee in charge:

Dr. Mark S. Marley

Dr. Kurt S. Anderson

Dr. Erich Karkoschka

Dr. Viatcheslav S. Solomatov

Dr. Reinirus A. Walterbos

ACKNOWLEDGEMENTS

Grad school was not the experience I thought it would be, but through lots of help and just plain luck I survived it. Please indulge me as I take a few pages to thank the people and institutions who contributed to the completion of this project and my growth as a scientist and person.

I'm prevented by reasons of sheer space to mention all the friends and teachers that touched my life in a positive way prior to grad school but a hearty thanks goes out to all of them, especially these three. Coming to the University of Arizona reawakened my boyhood love for astronomy, as I got to study in one of the top schools in the field. I'd like to thank Ray White for guiding a clueless undergrad and demonstrating the joy of astronomy. Sometimes cynicism can conquer youthful idealism in early adulthood, but thanks to Joe Hermann, my band director for the first two years in the Pride of Arizona marching band for helping me delay it a while longer. Our Band Day performance my freshman year is still possibly my proudest moment. Kudos go to William Hoffmann for taking an insecure kid with few practical skills, and giving him a chance to work in a real research environment. He more than anyone is responsible for my continuation into graduate school. In addition I'd like to take a moment to give thanks for the excitement and entertainment provided by my favorite basketball teams, in the 1992-93 Western Conference Champion Phoenix Suns and last year's National

Collegiate Men's Basketball Champion Arizona Wildcats.

In the present no one deserves more credit for the completion of this project than Mark Marley, who more than anyone I've ever met has the ability to bring clarity to the toughest topics, both academic and personal. He gave me the freedom to choose my own path and encouraged me to pursue my own funding when I thought it was just a long shot. And of course, he dealt with all of my angst. He, along with Reta Beebe and Anatoly Klypin have the all too rare knowledge that just sometimes, substance is worth more than show, and I am indebted to them for that. I'd also like to thank my committee members for their help, advice, and primarily for actually reading this text and listening to my talks without laughing – too hard. Thanks to those who served on my committee at earlier stages but were unavoidably absent from the final exam, Reta Beebe, Tom Hearn, and Nick Schneider. Others who made it possible were the folks at the NASA Solar System Exploration Division who trusted me enough to invest $55,000 over three years in my education, through grant NGT-51383, and Heidi Hammel, who contributed gratis sub-half-arcsec IRTF data she had no use for.

Many people made this place semi-tolerable, and I don't know how I could have survived without them. Primary thanks goes to the other four members of the Lost Class^{TM}, especially Percy Gómez and Matt Carlson for seeing it through with me to the bitter end. Also from the Lost Class was a very special friend and officemate who was always there for me when I was down, even after she left, Sue

Lederer. Others who made it all a little better were Pedro Sada, Kevin Marvel, Jason Kendall, Nichole King (4+ years in the same office with no major injuries or fights), Amy Simon, Matt Templeton, Salman Hameed, Mark Bliton, Charles Hoopes, Neal Miller, Vanessa Galarza, Andrey Kravtsov, Qing Bin "Ben" Xie, Chris Gatton, Star, Jenna, Jill Leonardi, the gang at Chameleon's on Tuesday nights, and the office staff in my last year (my only link to the real world): Cheryl Beer, Dacia Pacheco, Mendy Fowler, and Merrilee Saige, along with all their predecessors. Also thanks to AnnaClaire Marley for keeping her father too busy to notice how much I was goofing off.

When one grows up, it's important to have someone you can alternately love, hate, play with, and fight with. My sister Sarah filled all these roles. Thanks to her, and all my (at the time of this writing) little first cousins, who shared their energy, enthusiasm, and unconditional love, Leslie, Steven, Teddy, Eric, Adam, and Jeffrey Spector. In the end the people who can have the most positive influence in a young person's life are the parents, so I'd like to thank most of all Myrna Spector and Severin Walter for bringing me the gift of life, and for always being there whenever I needed them.

This research has made use of NASA's Astrophysics Data System Abstract and Article Services, and observations obtained by the ARC 3.5-m Telescope, NASA's Infrared Telescope Facility, and the Hubble Space Telescope.

VITA

March 15, 1970 – Born in Los Angeles, California

May, 1992 – B.S. in Astronomy and Physics, University of Arizona, Tucson, Arizona

1991 - 1992 – Student Assistant, University of Arizona, Tucson, Arizona

1992 - 1995 – Teaching and Research Assistant, New Mexico State University, Las Cruces, New Mexico

May, 1995 – M.S. in Astronomy, New Mexico State University, Las Cruces, New Mexico

1995 - 1997 – National Aeronautics and Space Administration Graduate Student Research Fellow, New Mexico State University, Las Cruces, New Mexico

PROFESSIONAL AND HONORARY SOCIETIES

American Astronomical Society

PUBLICATIONS

Walter, C. M., Hammel, H. B., & Marley, M. S. 1997, *A Vertically and Spatially-Resolved Model of the Scatters in the Uranian Atmosphere*, Icarus, submitted.

Walter, C. M., & Marley, M. S. 1997, *Temporal Variations in the Uranian Geometric Albedo: An Analysis of Atmospheric Scatterers in the Near-Infrared*, Icarus, submitted.

Walter, C. M., Marley, M. S., Hunten, D. M., Sprague, A. L., Wells, W. K., Dayal, A., Hoffmann, W. F., Sykes, M. V., Deutsch, L. K., Fazio, G. G., & Hora, J. L. 1996, *A Search for Seismic Waves from the Impact of the SL/9 R Fragment*, Icarus, 121, 341.

Walter, C. & Klypin, A. 1996, *Evolution of Clusters in Cold Plus Hot Dark Matter Models*, ApJ, 462, 13.

Abstracts:

Walter, C. M., Marley, M. S., & Hammel, H. B. 1997, *Spatial distribution and number density of scatterers in the upper Uranian atmosphere*, BAAS, 29, 993.

Walter, C. M., Marley, M. S., & Baines, K. H. 1996, *Temporal Variations in the Uranian Near-IR Geometric Albedo*, BAAS, 28, 1076.

Walter, C. M. & Marley, M. S. 1995, *Near-IR spatially-resolved observations of Uranus*, BAAS, 27, 1089.

Marley, M., Dayal, A., Deutsch, L., Fazio G., Hoffmann, W., Hora, J., Hunten, D., Sprague, A., Sykes, M., Walter, C.& Wells, K. 1994, *A Search for Seismic Waves Launched by the Impact of Comet Shoemaker-Levy/9*, BAAS, 26, 1580.

Marley, M., Wells, K., Hunten, D., Sprague, A., Hoffmann, W., Sykes, M., Dayal, A., Deutsch, L., Fazio, G., Hora, J., & Walter, C. 1994, *A Search for Seismic Waves Launched by the Impact of Comet Shoemaker-Levy/9*, EOS, 75, 403.

FIELDS OF STUDY

Major Field: Astronomy

Atmospheres and Interiors of Giant Planets

Infrared Observing Techniques

ABSTRACT

PROPERTIES OF THE URANIAN ATMOSPHERE AS REVEALED BY

OPTICAL AND INFRARED IMAGING

BY

CHARLES MARTIN WALTER, B.S., M.S.

Doctor of Philosophy in Astronomy

New Mexico State University

Las Cruces, New Mexico, 1997

Dr. Mark S. Marley, Chair

This dissertation describes one of the first major studies of the Uranian atmosphere to be performed since the flyby of Voyager 2 in 1986. Observations of the planet were taken from three observatories in the summers of 1995 and 1996, and the disk-averaged and latitudinal reflectivities were modeled to derive the properties of scatterers in the visible atmosphere and their changes in the intervening decade. In addition the likely changes in the temperature profile are examined and methods for detecting them described.

Narrowband images of Uranus in the near-infrared from Apache Point Observatory were acquired on three dates in 1995 and 1996. In order to best probe different levels of the stratosphere and upper troposphere the planetary geometric albedo was measured and modeled using 7 filters ranging from 1.28 – 2.36 μm. At the time of the 1996 observations there had been an 20 ± 5 times increase in the stratospheric haze column density since Voyager. The results suggest an upper limit on the optical thickness , $\tau \leq 15$ of the lower H_2S cloud at 1.58 μm. In addition the drastic increase in the haze column density masked the visual asymmetry of the CH_4 cloud deck seen by Voyager (Rages et al. 1991).

High-resolution images spanning 0.4–2.4 μm were made in the summer of 1995 with the Hubble Space Telescope and the Infrared Telescope Facility. In 1995 the haze column density above the CH_4 cloud was a factor of 6 larger than during the 1986 Voyager flyby. In addition the CH_4 cloud retained the asymmetry seen by Voyager, however the total cloud optical depth at visible wavelengths had decreased, to 0.2 ± 0.1 at -22.5° and 1.2 ± 0.4 at -65° latitude, possibly due to continuous heating of the southern hemisphere in that time.

As a result of the decrease in CH_4 cloud thickness and increase in haze particles the troposphere (and likely the effective temperature of the planet) is expected to have increased by 1–2 K, while the upper stratospheric temperature has increased by several degrees, depending upon the amount of haze at the time of observation.

TABLE OF CONTENTS

LIST OF TABLES

LIST OF APPENDIX TABLES

LIST OF FIGURES

LIST OF APPENDIX FIGURES

Chapter 1

INTRODUCTION

Uranus was discovered on March 13, 1781 by William Herschel, a musician and amateur astronomer, using a 0.2 m telescope of his own design at his residence in Bath, England. This was the first discovery of a planet in the modern era, as Mercury, Venus, Mars, Jupiter, and Saturn have been known since antiquity. As a 5.5 visual magnitude object, Uranus can be seen from dark sites with the naked eye, but is dim and small enough to be confused for a star without telescopic aid. Herschel was in fact conducting a star survey of the Milky Way when he noticed an object in Gemini that was too large and bright to be a star. Initially he thought he had discovered a comet, but a month's observing confirmed that the object had a circular orbit outside of Saturn and was thus a planet. Herschel initially named the star Georgium Sidus, or "George's Star." after his king George III. The honored monarch appropriately endowed Herschel with a lifelong pension enabling him to devote his energies full-time to astronomy, an important historical lesson for young astronomers in any era.

Uranus is but one of four giant planets in the solar system, along with Jupiter, Saturn, and Neptune. Because of their greater size, greater proximity, and greater disk contrast and therefore visual appeal, Jupiter and Saturn have been much better studied. However to understand the processes of planetary formation as it applies to our own solar system and others in formation it is important to be able to understand the current nature of as many giant planets as possible as well as their evolution.

With direct imaging we can probe the atmospheres of these planets down to pressures of several bars, a region known as the visible atmosphere. This region can be broken up into several sub-regions as defined in a pressure-temperature (P-T) diagram (the atmospheric structure of Uranus as determined by Voyager 2 is shown in figure 1.1). The lowest part of the atmosphere is known as the troposphere, and is defined as that region where the temperature decreases with height. The temperature minimum is the tropopause, above which lies the stratosphere, where the temperature increases with height. It is these regions that will be the focus of this study.

The primary constituents of the visible atmosphere of Uranus are gas and condensed ices. The gas is primarily H_2, He, and CH_4, as the low temperatures cause other highly abundant molecules such as NH_3 and H_2O to condense well below the visible atmosphere. The ices (their actual thermodynamical phase un-

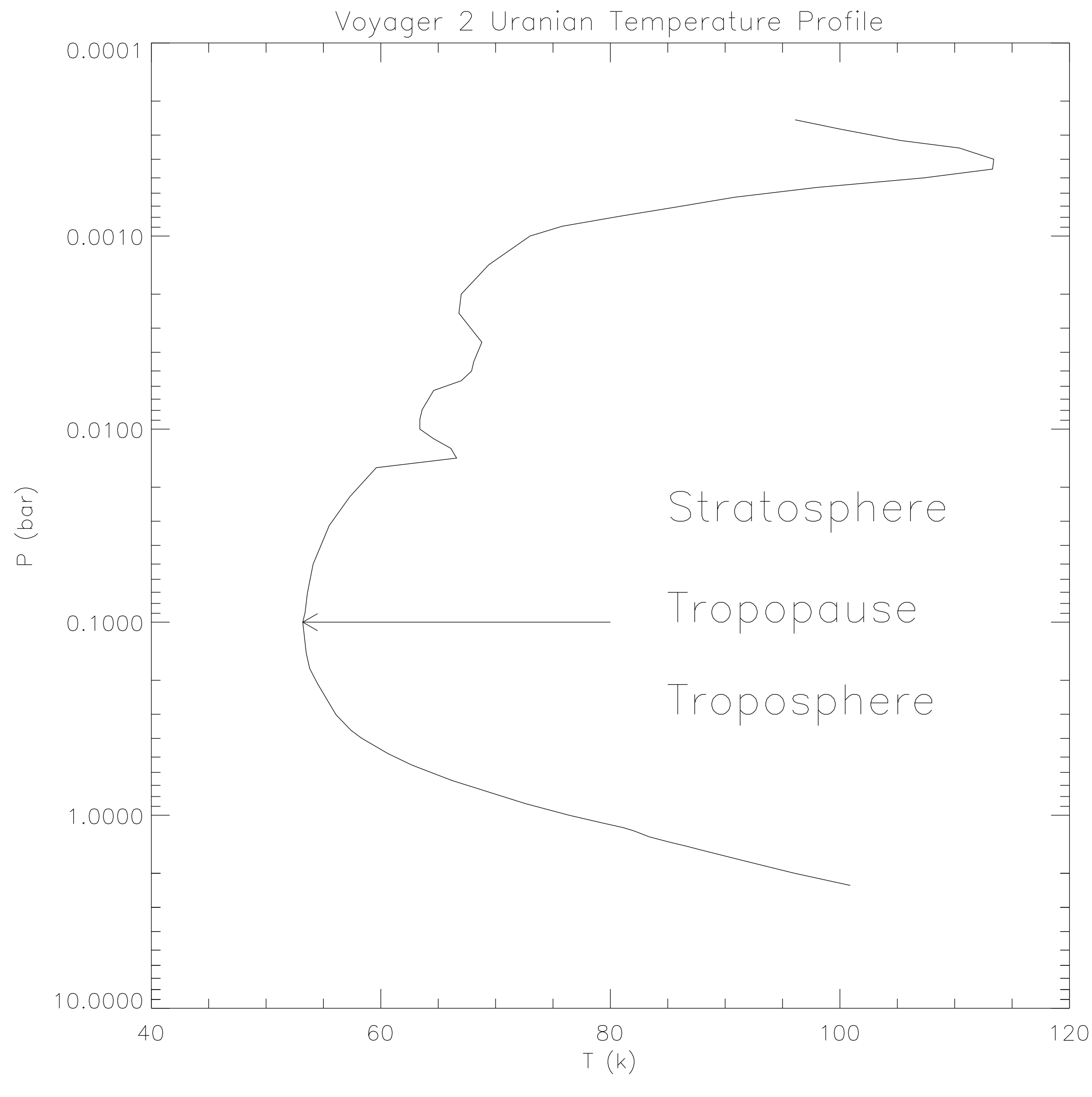

Figure 1.1: The temperature as a function of pressure in the Uranian atmosphere, as determined the Voyager 2 RSS occultation experiment.

known) are typically referred to as being in hazes or clouds, with the primarily distinction solely being the optical depth, as hazes are optically thin and clouds are optically thick. The sources of these ices typically differ in the stratosphere and troposphere. High in the stratosphere photochemistry of CH_4 driven by solar UV photons results in higher order hydrocarbons. These precipitate at higher temperatures than CH_4 and free-fall until vaporizing in the upper troposphere. In the troposphere, thermochemical analysis predicts a multi-layered cloud structure. In Uranus there is a CH_4 cloud high in the troposphere, that overlies a more optically thick cloud that is thought to consist of H_2S ices. Information about this cloud is difficult to discern without properly understanding the contents of the CH_4 cloud, which defines the edge to the visible atmosphere.

Like the earth, the outer planets have seasons, although their great distance gives them long orbital periods that spread the effects out over greater time intervals and thus they appear to be less dynamic. Uranus has an orbital period of 84 years, so it has not been studied in detail for entire orbit. Still it is likely to have different weather patterns than the other giant planets due to its unique rotational obliquity of 98°. This causes the polar regions, defined at latitudes $> \pm 8°$ to alternate receiving 42 continuous years of sunlight. Unlike any other major solar system object, over the course of an orbit the average insolation at the poles is greater than at the equator.

Prior to 1986 not a great deal was known about the planet due to its great distance. In particular the region beyond 600 nm was difficult to probe using imaging because of the severe gaseous molecular absorption in this region by CH_4 that gave the planet a blue-green appearance.

Voyager 2 was launched on its grand tour of the outer planets on August 20, 1977. The closest approach to Uranus was 81,500 km on January 24, 1986. It carried a wide variety of instruments that allowed the planet to be examined from the ultraviolet to the far-infrared. Data was transmitted back via radio to be received by the three 64-m antennas that comprise the NASA Deep Space Network. This signal also proved useful scientifically by studying its modulation as it was occulted by the planet on ingress and egress. This experiment, the Radio Science Subsystem (RSS), along with the InfraRed Imaging Spectrometer (IRIS), the UltraViolet Spectrometer (UVS) and the PhotoPolarimeter Subsystem (PPS) provided the bulk of the new data about the planet's atmosphere.

The planet Jupiter has a very distinctive banded structure, with alternating bright zones and dark belts. The zones result from localized upwellings of fresh NH_3 gas which condenses, whereas the belts are situated in a region of subsidence and are thought to be dark because of the accumulated effects of irradiation. At Uranus Voyager discovered a planet with a uniform upper cloud deck. Whereas Jupiter, Saturn and Neptune all have internal heat sources of the same order of magnitude as the energy absorbed from the sun, the heat flow from the Uranian interior is almost negligible compared to absorbed sunlight. This remains one of the biggest problems with our knowledge of the planet. While the winds in mid-latitudes blow in the direction of rotation as velocities from 40–160 m/s, in the equatorial region the winds blow counter to the rotation at 100 m/s.

The temperature at a point on a planet depends upon the current radiative equilibrium, the relationship between the incoming sunlight, and how quickly it is redistributed throughout the atmosphere and reradiated. Because the emission of a planet resembles a blackbody to first order, the time required to effectively redistribute the energy is dependent upon the effective temperature, which the temperature of a blackbody producing the identical amount of emission observed. Uranus has an effective temperature of 59 K (Pearl et al. 1990), so it does not radiate effectively, having a time constant in the upper troposphere on the order of 100 years. This is the amount of time required for a temperature perturbation to drop to 1/e of its initial value. Because cooling takes so long a seasonal lag is built up. For Uranus this almost an entire season, i.e., at summer solstice, a region would be experiencing the equivalent of autumnal equinox. For Earth this lag is 1.3 months, causing temperatures in the northern hemisphere to peak in late July. When viewed by Voyager the south pole was at summer solstice, yet both poles and the equator had identical temperatures within the measurement errors in the upper troposphere (the region that dominates thermal emission), while the mid-latitude regions were a few degrees cooler. The equality of temperatures is thus consistent with the seasonal lag.

When Uranus is at its closest and brightest (at opposition), the planet has a phase angle (the angle between the sun and earth as viewed from Uranus) of $0°$, and its visible spectrum is solar radiation that has been back-scattered. Because the planet is so far from the sun, only phase angles as high as $3°$ can be viewed. Characteristics of non-gaseous material in an atmosphere can be learned by studying its scattering characteristics over all angles. Voyager had an unprecedented opportunity to view the planet at a variety of phase angles. The resultant data confirmed the existence of high altitude haze particles by the variation of brightness at the limb of the planet.

Our knowledge about the planet including the Voyager results was summarized in the University of Arizona Press book Uranus, (Bergstralh et al. 1991). Little work has been done since the Voyager era because limits had been reached on what could be done with ground-based optical imaging and spectroscopy. In the past several years improvements in detector technology have expanded our capabilities. Optical imaging has improved with the launch and subsequent refurbishment of the Hubble Space Telescope (HST), which imaged Uranus, in 1994 and 1995. By observing above the earth's atmosphere the spatial resolution that can be achieved on the planetary disk improved by an order of magnitude. In addition, the continuing development of infrared detectors has made their use much more practical in terms of feasible observing times required and greater resolution provided.

A blackbody is an infinitely thick object in thermodynamic equilibrium, with the amount of energy absorbed and emitted in balance at a characteristic temperature. This serves as useful tool for examining the emission spectrum of a large body, because if it is thick enough all internal radiation will be reabsorbed before reaching the surface, and the observed spectrum will be that of a blackbody of the surface temperature. This blackbody spectrum as shown in figure 1.2, drops off quickly at shorter wavelengths, but slowly tails off at higher wavelengths. The region of the electromagnetic spectrum where the emission from our sun is the greatest is defined to be the optical. By Wien's law the product of the peak wavelength of emission and blackbody temperature is a constant. Since the planets in our solar system are at least an order of magnitude cooler than the sun, their emission peaks in the infrared. As seen in figure 1.3 there is very little overlap in the observed spectrum of a planet between the reflected sunlight and the thermal emission. Although the total intensity at any wavelength increases as the temperature increases, the flux of the solar part of the spectrum viewed from the Earth is attenuated $\propto \mathrm{r}^{-4}$ where r is the distance between the planet and Earth, because it travels from the sun to the planet and back to the Earth, while the thermal emission only traverses the distance once, so is attenuated as $\propto \mathrm{r}^{-2}$. Because of this the intensities are of similar orders of magnitude. As seen in the figure both spectra are minimal at 5μm. Shortward of this the spectrum can be interpreted as reflected sunlight, while longward is emission from the planet itself.

This relationship greatly simplifies the process of using the measured spectrum to determine the properties of a planetary atmosphere.

Our knowledge of the planet dates back to its conditions a decade ago. Since then the south pole has passed from solstice towards equinox. This work uses observations of reflected sunlight to infer the characteristics of scattering agents in the Uranian atmosphere, primarily the stratospheric hazes and tropospheric clouds. We are interested in gaining all possible knowledge about the distribution of these particles over the planetary surface, and how this has changed since Voyager. By using the highest resolution data available in the optical from HST as well as unprecedented sensitivity in narrow and broadband coverage in the near-infrared we can test the changes in the Voyager distribution findings while using the greater spread in observed wavelengths to yield information about the particle sizes. In addition, observations in the near-infrared offer sensitivity to the stratosphere unattainable by optical imaging.

The goal of this dissertation is to obtain a consistent model that describes the amounts of scatterers in the atmosphere, their vertical location, their distribution over the planetary disk, and by comparison to Voyager the possible relation to season. Chapter 2 describes the basic observing techniques and theoretical background to modeling the radiative transfer that were used in the analysis. Chapters 3 and 4 discuss two separate observational studies that were carried out and their ultimate results. In these chapters use of the pronoun we refers to myself and my

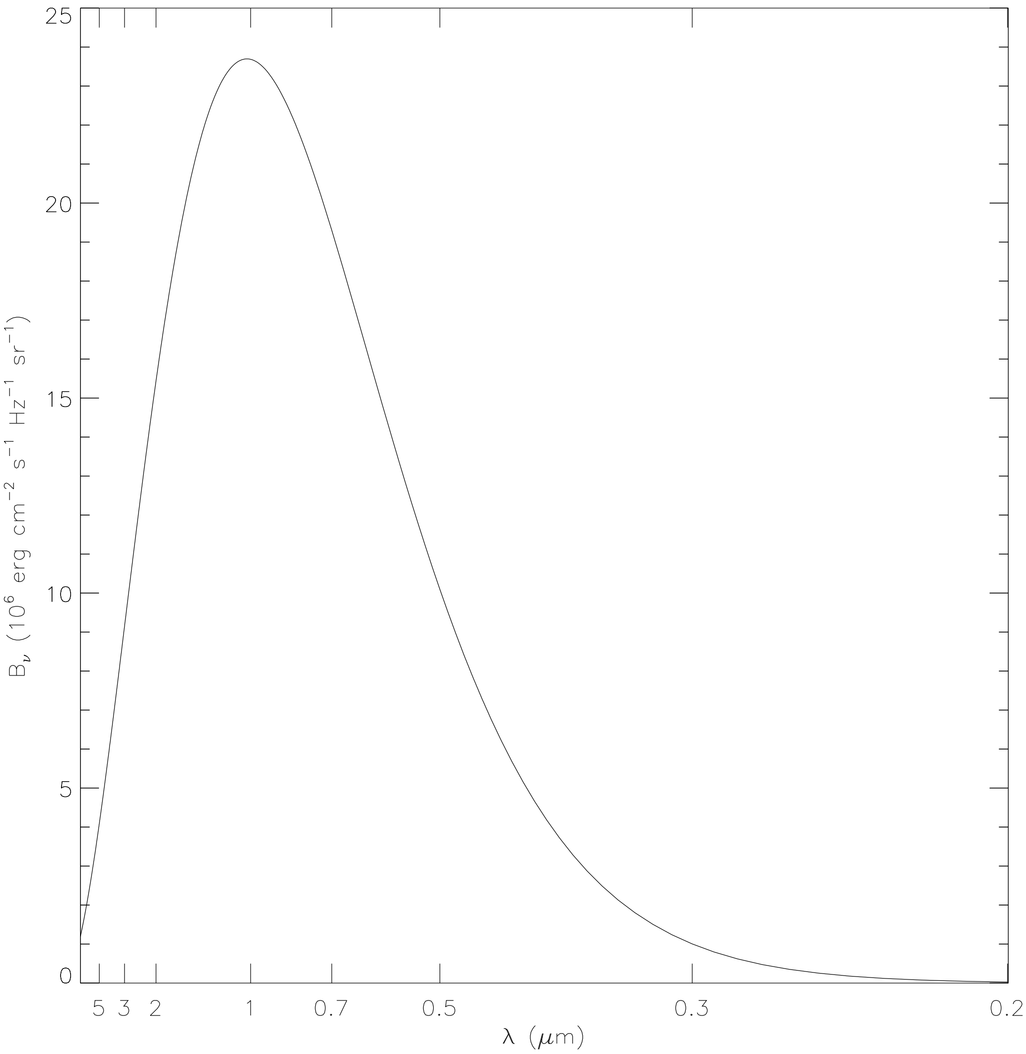

Figure 1.2: A blackbody curve calculated for a temperature of 5000K.

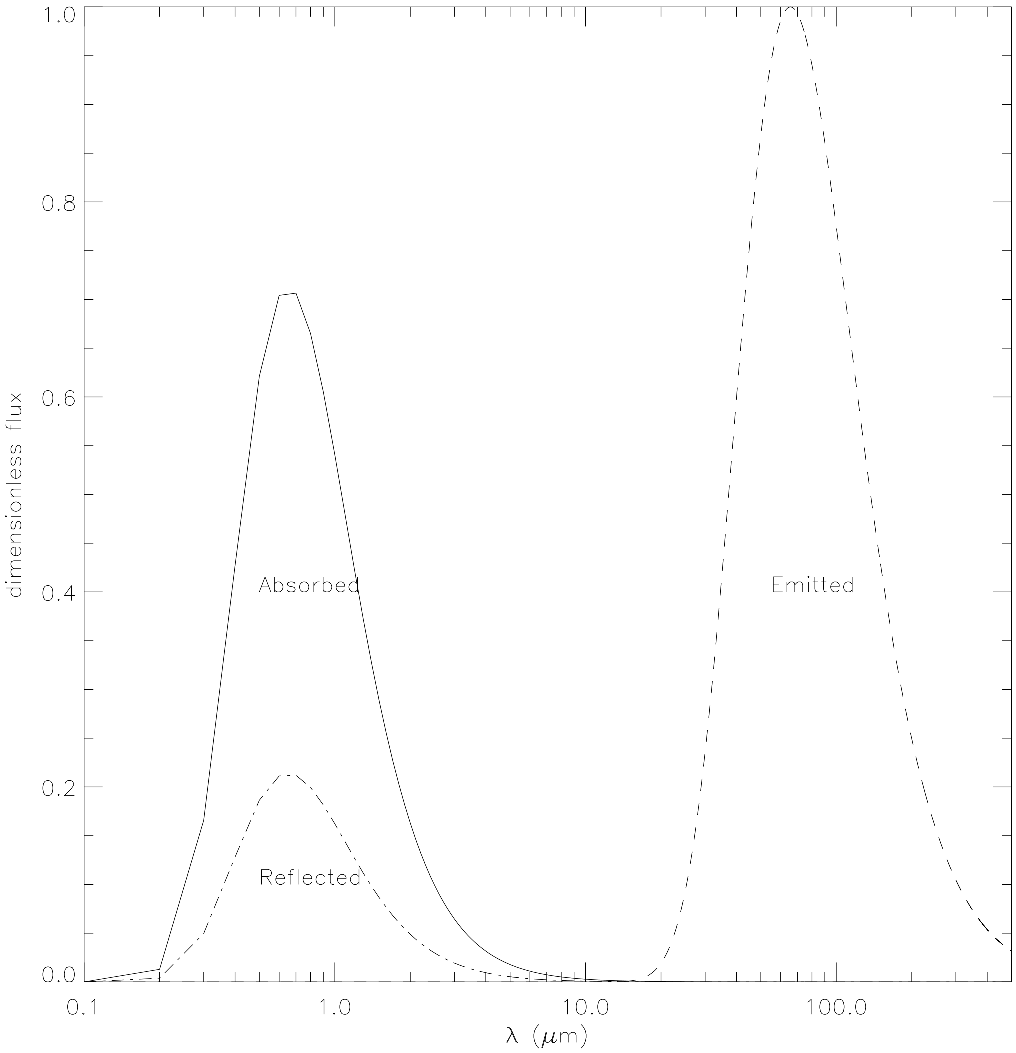

Figure 1.3: A simplistic representation of the energy balance in the atmosphere of Uranus. The flux is given in units of erg cm^{-2} (log cm^{-1})$^{-1}$ sr^{-1} s^{-1} and scaled to give a maximum of 1. curve peaking at 0.6 μm represents the solar spectrum as a blackbody with a temperature of 5800K (the sun's effective temperature) as received by Uranus at its mean solar distance. The bolometric albedo of Uranus is 0.3, treated as a constant over wavelength and represented by the lower curve. To the right of the figure is the spectrum of Uranus, given as a blackbody with a temperature of 59.1 K.

advisor Mark Marley in both, and also Heidi Hammel in Chapter 4, although I performed all data reduction and analysis. In Chapter 5 the likely changes of the planetary thermal emission since the Voyager era are predicted, and Chapter 6 draws the conclusions of all studies together.

Chapter 2

THEORY AND TECHNIQUES

2.1 Radiative Transfer

The amount of radiation emitted from an object can be quantified by its specific intensity I_ν,

$$I_\nu = \frac{dE}{dAdtd\Omega d\nu}, \qquad (2.1)$$

defined as the amount of energy dE passing through a unit area dA that is normal to its direction, coming from a solid angle $d\Omega$ in a monochromatic frequency $d\nu$ in a time dt. Intensity has the units erg s^{-1} cm^{-2} $ster^{-1}$ Hz^{-1} in the cgs system which will be used throughout this work.

The radiative transfer equation treats the change of specific intensity of a beam due to emission and/or absorption from the media it passes through en route to the observer. The emission coefficient j_ν is defined as,

$$j_\nu = \frac{dE}{dVdtd\Omega d\nu}, \qquad (2.2)$$

the increase change in energy per volume dV over the solid angle dΩ in a monochromatic frequency in a unit of time, and has the units erg s^{-1} cm^{-3} ster^{-1} Hz^{-1}. It does not have an explicit dependence upon the specific intensity of the background beam it encounters because it is spontaneous emission.

The absorption (and negative absorption, or stimulated emission) are quantified using the absorption coefficient α_ν, which is defined as the loss of intensity dI$_\nu$ over the path length traveled ds, and is dependent upon the intensity of the incident beam I$_\nu$,

$$-\alpha_\nu I_\nu = \frac{dI_\nu}{ds}, \tag{2.3}$$

where α_ν has the units cm^{-1}.

The radiative transfer equation combines these two coefficients to treat the variation of the specific intensity along the line of sight

$$\frac{dI_\nu}{ds} = -\alpha_\nu I_\nu + j_\nu. \tag{2.4}$$

To simplify this equation it is useful to express the absorption in dimensionless terms. It is with this desire that the concept of optical depth is introduced. The optical depth is the integral of the absorption coefficient over the path traveled,

$$\tau_\nu = \int_{s1}^{s2} \alpha_\nu ds. \tag{2.5}$$

An optical depth $\tau \ll 1$ means the medium is optically thin, or virtually transparent to incoming or outgoing radiation, while an optical depth $\tau \gg 1$

conversely yields an optically thick or opaque medium. These approximations can be useful at times, but a great deal of this work is in the area in between.

Dividing the radiative transfer equation by α and introducing the source function $S_\nu = j_\nu\ \alpha_\nu^{-1}$ leaves a much more usable form,

$$\frac{dI_\nu}{d\tau_\nu} = -I_\nu + S_\nu. \tag{2.6}$$

By intergrating over the optical depth, it is possible to arrive at the formal solution,

$$I_{\nu,\tau_\nu} = I_{\nu,0}e^{-\tau_\nu} + \int_0^{\tau_\nu} e^{-\tau_\nu - \tau'_\nu} S_{\nu,\tau_\nu} d\tau'_\nu. \tag{2.7}$$

2.1.1 Scattering

In many cases scattering is an significant source of photon attenuation. We can therefore define a total extinction coefficient $\alpha_\nu + \sigma_\nu$ where σ_ν is the scattering coefficient. It is thus useful to define a single scattering albedo $\tilde{\omega}_\nu$ to determine what fraction of the entire absorption process is due to scattering,

$$\tilde{\omega}_\nu = \frac{\sigma_\nu}{\alpha_\nu + \sigma_\nu}. \tag{2.8}$$

Because at the conditions treated in this work the atmosphere is mostly in local thermodynamic equilibrium (LTE), an amount of energy (1 - $\tilde{\omega}_\nu$) $I_{\nu,\odot}$ absorbed from the sun is reemitted in the thermal infrared.

Atmospheric scattering can be described by a phase function that gives the distribution of scattered radiation as a function of scattering angle. This is typically defined as $P(\cos\Theta)$ which is normalized as

$$\frac{1}{4\pi}\int_0^{4\pi} P(\cos\Theta)d\Omega = \tilde{\omega}_\nu, \tag{2.9}$$

where Θ is the scattering angle, determined from spherical trigonometry,

$$\cos\Theta = -\cos\theta\cos\theta_0 - \sin\theta\sin\theta_0\cos(\varphi - \varphi_0), \tag{2.10}$$

where the radiation is incident from direction (θ_0, φ_0) and scattered in direction (θ, φ), with θ and φ representing the elevation and altitude respectively. The latitude is often written as $\mu = \cos\theta$, leaving the equation in the form

$$\cos\Theta = -\mu\mu_0 - (1-\mu^2)^{1/2}(1-\mu_0^2)^{1/2}\cos d\varphi. \tag{2.11}$$

For isotropic scattering, the phase function is simple to compute, $\mathrm{P}(\cos\Theta) = \tilde{\omega}_\nu$. For this work two separate phase functions are used, those of Rayleigh scattering and the Henyey-Greenstein function.

Rayleigh scattering comes from scattering of radiation by individual molecules of gas, and is important for those regimes where the particle size $\mathrm{r} \ll \lambda$, the wavelength in question. The resultant phase function is symmetric across the origin, with twin lobes as seen in Figure 2.1. Mathematically this is

$$P(\cos\Theta) = \frac{3}{4}(1+\cos^2\Theta). \tag{2.12}$$

Because it is difficult to derive an analytic phase function that is correct over the entire range of scattering angles, one technique to overcome this is to define

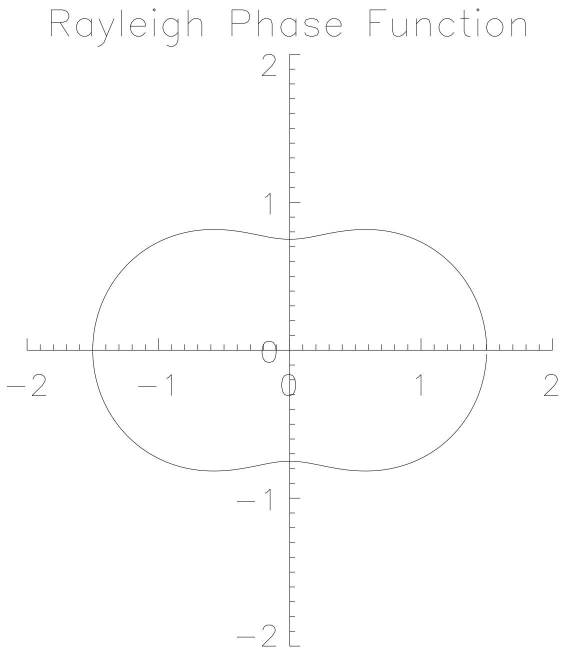

Figure 2.1: The phase function of Rayleigh scattering. Forward scattering is to the right and backward scattering to the left.

an asymmetry parameter g,

$$g =< \cos\Theta >= \frac{1}{2\tilde{\omega}_\nu}\int_{-1}^{1} P(\cos\Theta)\cos\Theta d(\cos\Theta), \tag{2.13}$$

where a system with $g = 1$ is a perfect forward scatterer, one with $g = -1$ is a perfect backward scatter, and one with $g = 0$ is symmetrically isotropic.

This then serves as input to the empirical Henyey-Greenstein phase function,

$$P(\cos\Theta) = \frac{\tilde{\omega}_\nu(1-g^2)}{(1+g^2-2g\cos\Theta)^{3/2}}. \tag{2.14}$$

Frequently the Henyey-Greenstein phase function fails to reproduce the backscatter peak effectively. The solution for this is to use a double Henyey-Greenstein phase function,

$$P(\cos\Theta) = fP(\cos\Theta, g_1) + (1-f)P(\cos\Theta, g_2), \tag{2.15}$$

where f is the fractional contribution assigned to each component and g_2 a negative value to produce significant backscattering.

Rayleigh theory is merely a limiting case of Mie theory, which is a full treatment of the interaction of an electromagnetic wave with a spherical particle. Mie theory is typically used for aerosols with size parameters $x=2\pi r/\lambda$ between 0.1 and 10, and is an empirical evaluation that assumes spherical particles. Below this the Rayleigh formulation is used, and above this the particle is sufficiently larger than the radiation wavelength to use geometric optics. The Mie computation involves an infinite series that seeks to reproduce the effects of all reflections and refractions given a size parameter and real and imaginary indices of refraction. For small size parameters scattering is largely isotropic, but becomes highly forward scattering as x increases, reaching a limit of g=0.83.

2.1.2 Extinction

Absorption in the Uranian atmosphere is caused by the interaction of radiation with molecular CH_4 and H_2. In the visible and near-infrared are molecular rotovibrational transitions. Their absorption coefficients, or opacities, are typically given in units of cm^{-1} for CH_4 but cm^{-2} for H_2 because the H_2 optical depth is dependent upon the column densities of both particles involved in the collision (see below). It is frequently useful to have molecular opacities in terms of a standard atmosphere, and most laboratory results are published in this manner. The process involved is to convert the molecular column densities from cm^{-2} to what is known as cm-amagat by dividing by Loschmidt's number $\mathrm{n}_0 = 2.687 \times 10^{19}$ cm^{-3},

$$\xi = \frac{N}{n_0} \mathrm{cm} - \mathrm{amagat}, \tag{2.16}$$

giving the new density in terms of ξ. Loschmidt's number is simply the number density to be expected in STP, a pressure of 1 atm (1013250 dyne cm^{-2}) and temperature of 0°C (273.15 K). In these cases then the absorption coefficients will have units of $(\text{cm-amagat})^{-1}$.

CH_4 is a tetrahedral molecule that has two important fundamental modes, with bandheads of the ν_3 mode at 3.3 μm and ν_4 at 7.8 μm. Overtones of these features combine to give a rich spectrum across the region of interest. For computational ease in dealing with the large number of lines when high resolution is not necessary these opacities are often cast in terms of k-coefficients. The line strengths are broken up so that the total contribution can be obtained from 8 or 10 Gaussian quadrature points, necessary to determine the emission strength from different groups on lines. When studying extinction however, summation over each coefficient k_i and Gaussian weight W_i can give the total transmission T and the total effective optical depth τ,

$$T = \sum_i W_i e^{-k_i \xi} = \sum_i W_i e^{-\tau_i}, \tag{2.17}$$

$$\sum_i W_i \ln e^{-k_i \xi} = \sum_i W_i \ln e^{-\tau_i}, \tag{2.18}$$

$$\sum_i \ln e^{-W_i k_i \xi} = \sum_i \ln e^{-W_i \tau_i}, \tag{2.19}$$

$$\xi \sum_i W_i k_i = \sum_i W_i \tau_i = \tau, \tag{2.20}$$

so the total optical depth from CH_4 can be computed from a weighted sum of the absorption coefficients multiplied by the number density.

For H_2 the procedure is more complicated. Because H_2 is a homonuclear molecule, it has no permanent dipole moment, prohibiting vibrational and rotational interactions with the electric field. However a temporary dipole can be established upon collision with another molecule. In a dense atmosphere largely consisting of H_2 this pressure-induced absorption (PIA) can be a significant source of opacity.

The fundamental vibrational bandhead of H_2 is near 2.3 μm, but the rotovibrational spectrum is complicated further by the two states of molecular hydrogen. The lower energy ground state (j=0) is called para, where the nuclear spins are anti-parallel, while the other ground state (j=1) is ortho, with parallel spins. The level populations are generally defined as either being normal, where the ortho-para ratio is equivalent to the 3:1 statistical weight ratio, or in equilibrium, dependent upon the local temperature. The rotational transitions allowed are Δj $= -2, 0, 2$, known as the O, Q, and S branches. Contributions from the O branch are weak, but the typical spectrum of the fundamental band has three peaks, Q_1(j) (2.40 μm), S_1(0), 2.25 μm, and S_1(1) (2.12 μm). The format is X_vj with X the bandtype, and v and j the initial vibrational and rotational states.

The formulation is a little different than that for CH_4 because the opacity is dependent upon the number density of H_2 and the other molecule involved in the collision. It is then given in units of $(\text{cm}^{-1}\text{-amagat}^{-1})^2$. The path length ds must then be in units of $(\text{cm-amagat})^2$,

$$ds = \frac{N_1 N_2}{n_0^2}, \tag{2.21}$$

where N_1 and N_2 are the column densities of the two gasses.

In the condition of hydrostatic equilibrium over small pressure differences the column density N between two levels can be approximated effectively as dP g^{-1} μ^{-1} m_H^{-1} where dP is the pressure difference, g the local acceleration due to gravity, m_H the mass of a hydrogen atom (1.673×10^{-24} gm), and μ the mean molecular weight in atoms of hydrogen (the atomic mass unit, or amu).

2.1.3 Thermal Emission

When a body is in thermal equilibrium the source function S_ν can be replaced by the Planck function B_ν. In an optically thick medium the specific intensity I_ν is then replaced by B_ν – the required condition for blackbody emission,

$$B_\nu = \frac{2h\nu^3/c^2}{e^{h\nu/kT} - 1}. \tag{2.22}$$

The peak frequency ν_{max} can be solved for by differentiation, leading to the equation

$$\frac{\nu_m ax}{T} = 5.88 \times 10^{10} \frac{Hz}{K}, \tag{2.23}$$

which then converted to wavelength gives a peak λ_{max},

$$\lambda_{max}T = 0.510cmK. \tag{2.24}$$

A similar relation can be derived using B_λ that gives a different maximum intensity,

$$\lambda_{max}T = 0.290cmK. \tag{2.25}$$

This relation is known as Wien's law. B_ν and B_λ are closely related.

$$B = \int_0^\infty B_\nu d\nu = \int_0^\infty B_\lambda d\lambda. \tag{2.26}$$

When $h\nu \ll kT$, the exponential in the denominator can be expanded, giving the Rayleigh-Jeans law,

$$I_\nu = B_\nu = \frac{2\nu^2}{c^2}kT. \tag{2.27}$$

The intensity of an object can then be simplified by assigning a brightness temperature to it. This is the temperature the object would have if it were a blackbody emitting the same amount of energy at that frequency. The brightness temperature can still be used for non-optically thick emission and where $h\nu \not\ll kT$ (for instance the optical and infrared for planetary atmospheres), and can be used apart from this equation but in those cases it is no longer a physical temperature.

2.2 Atmospheric Models

To construct an atmospheric model requires the ability to define several macroscopic parameters at an adequate number of atmospheric levels to avoid improper discontinuities. Among these are pressure, temperature, and number density. These are generally defined in terms of each other in what is known as an equation of state. The simplest and most useful equation of state is the ideal gas law P=nkT, where k is Boltzmann's constant, 1.38×10^{-16} erg K^{-1}, and n is the number density, measured in cm^{-3}.

In a planetary atmosphere there is a vertical stability brought on by hydrostatic equilibrium, where the gravitational force from below dF = -g dm is balanced by the pressure over a unit area A from above dF = A dP. Over the relatively small region of the planet occupied by the visible atmosphere, the radius variation is small and the amount of mass below unchanging enough to treat g as a constant. Assuming a constant density this can be given in terms of the volume V

$$-g\rho dV = AdP, \tag{2.28}$$

or in terms of the vertical distance dz

$$\frac{dP}{dz} = -\rho g. \tag{2.29}$$

Assuming the perfect gas law P = nkT = $\frac{\rho}{\mu m_H}$kT can give the pressure as a function of height

$$\frac{dP}{P} = dlnP = -\frac{\mu m_H g}{kT}dz, \tag{2.30}$$

which integrated gives

$$P = P_0 e^{-\frac{z}{H}}, \tag{2.31}$$

where H is defined as a scale height, the e-folding distance over pressure.

In order to calculate the optical depth a photon encounters on its travel through an atmosphere it is necessary to accurately determine the path length traveled. At the each point on a planetary disc this length is a little different, from a minimum at the center to a maximum at the disk, where the object becomes optically thick higher in the atmosphere. In the solar photosphere the temperature is cooler with height, leading to the limb-darkening effect seen in the sun. In most cases it is quite appropriate to neglect the curvature of the planet in calculating this distance, known as the plane-parallel approximation as seen in figure 2.2. Thus the distance ds can be computed as $H \sec z$ where H is the path length of normal incidence and z the zenith angle. The error in this approximation is at the 1% level at a zenith angle of 76° and at the 10% level at an angle of 86°. When greater accuracy is required, it is possible to use the geometry to derive a multiplicative correction factor f,

$$f = \frac{X}{D} = \frac{H \sec^2 z}{-R_u + \sqrt{R_u^2 + \sec^2 z (2HR_u + H^2)}}. \tag{2.32}$$

2.3 Observational Constraints

To make the final atmospheric model as accurate as possible, it is necessary to derive an observable quantity to serve as a constraint on the phase space of possible models. One such observable is the geometric albedo A, defined as the fraction of sunlight incident upon a planet that is reflected compared to a uniformly lit Lambert disk at a scattering angle of 180°, i.e., opposition, where the earth and

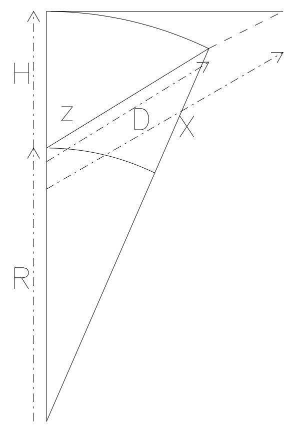

Figure 2.2: Geometric diagram of the plane parallel approximation with an exaggerated scale. This approximation computes the distance traveled by a photon with zenith angle z as X, instead of the correct value D. For zenith angles less than 76° this causes a less than 1% error. In the diagram R is the radius of the planet, and H the relevant scale height.

planet are exactly at the same solar longitude.

The solar flux H_ν (units erg s^{-1} cm^{-2} Hz^{-1}) has been tabulated at a mean Earth distance of 1 AU. The flux incident upon Uranus I_ν is then related to the ratio between the the mean heliocentric Earth distance $d_\oplus$ and the heliocentric distance to Uranus at the time of observation d_u,

$$I_\nu = H_\nu \left(\frac{d_\oplus}{d_u} \right)^2 . \tag{2.33}$$

The flux F_ν received at Earth can be determined by integrating the flux intercepted by the Uranian disk over the solid angle Uranus subtends as seen by Earth. The term $\frac{1}{\pi}$ changes the typical definition of flux to an astrophysical flux, which is the observable measured,

$$F_\nu = \frac{1}{\pi}\int_0^{4\pi} AI_\nu \cos\theta d\Omega, \tag{2.34}$$

$$F_\nu = 2\int_0^{\theta} AI_\nu \sin\theta\cos\theta d\theta, \tag{2.35}$$

$$F_\nu = \frac{1}{2}AI_\nu[1-\cos 2\theta], \tag{2.36}$$

$$F_\nu = AI_\nu \sin^2\theta. \tag{2.37}$$

From figure 2.3 it can be seen that

$$\sin\theta = \frac{r_u}{\sqrt{r_u^2 + d_{u\oplus}^2}} \simeq \frac{r_u}{d_{u\oplus}}, \tag{2.38}$$

where r_u is the planetary radius and $d_{u\oplus}$ is the geocentric distance at the time of observation. The flux received at Earth is given by

$$F_\nu = AI_\nu\left(\frac{r_u}{d_{u\oplus}}\right)^2 = AH_\nu\left(\frac{d_\oplus r_u}{d_u d_{u\oplus}}\right)^2, \tag{2.39}$$

which can be inverted to solve for the albedo in terms of the observable flux at Earth, the known solar spectrum, the cross-sectional size of Uranus, and the distances between the three objects,

$$A = \left(\frac{d_u d_{u\oplus}}{d_\oplus r_u}\right)^2 \frac{F_\nu}{H_\nu}. \tag{2.40}$$

When it is possible to achieve spatial resolution on the planet the quantity I/F, can be used. This represents the albedo of the planet over a specific region

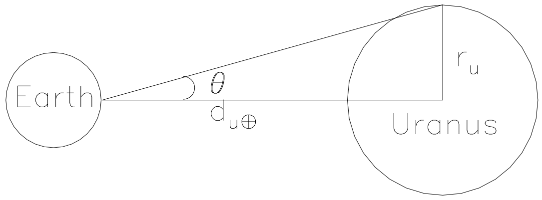

Figure 2.3: Scattered solar radiation by Uranus is observed from a point on the earth to subtend an angle θ, related to the distance between the planets $d_{u\oplus}$ and radius of Uranus r_u. Because these two values differ by orders of magnitude, the triangle hypotenuse can also be assigned a value of $d_{u\oplus}$.

of the planet. For this the angle sin θ is not resolved over the entire planet, but merely that part which corresponds to one pixel – the plate scale, measured in rad pix^{-1}, giving the final equation

$$\frac{I}{\pi F} = \left(\frac{d_u}{\theta d_\oplus}\right)^2 \frac{F_\nu}{H_\nu}, \tag{2.41}$$

or

$$\frac{I}{F} = \pi \left(\frac{d_u}{\theta d_\oplus}\right)^2 \frac{F_\nu}{H_\nu}, \tag{2.42}$$

where π F is the astrophysical flux arriving at the planet being observed.

2.4 Flux Computation

In order to obtain accurate model albedos and I/F's, a method must be developed to solve the radiative transfer equation accurately at various levels in the atmosphere. The chief difficulty is in defining the source function S_ν in Eq. (2.6). In the optical and near-infrared thermal emission is negligible, so the source function consists of two terms, radiation which is scattered by the atmosphere, and incoming solar radiation. The first term arrives from the diffuse scattering within the atmosphere. The emission coefficient j_ν is dependent upon the incoming intensity I_ν, the absorption coefficient α_ν and single-scattering albedo $\tilde{\omega}_\nu$, and the phase function P,

$$j_\nu = \frac{\tilde{\omega}_\nu \alpha_\nu}{4\pi} \int_0^{4\pi} I_\nu P(\cos\Theta) d\Omega. \tag{2.43}$$

The second term comes from attenuated incoming solar radiation scattered in each layer. It is dependent upon some of the previous terms, along with the incoming solar flux πF_ν, the optical depth at a point in the atmosphere τ, and the incoming zenith angle of the radiation μ_0,

$$j_\nu = \frac{\pi F_\nu \tilde{\omega}_\nu \alpha_\nu}{4\pi} P(\cos\Theta) e^{-\tau/\mu_o}. \tag{2.44}$$

The total source function is then

$$S_\nu = \frac{\tilde{\omega}_\nu}{4\pi} \int_0^{4\pi} I_\nu P(\cos\Theta) d\Omega + \frac{\tilde{\omega}_\nu F_\nu}{4} e^{-\tau/\mu_0} P(\cos\Theta). \tag{2.45}$$

The problem is to characterize this source function in an efficient way. In this work two separate techniques are used, the Eddington source function, and the adding-double techniques. Both compute fluxes with errors of 10%.

2.4.1 Eddington Source Function

The Eddington source function technique involves characterizing the source function substituting the intensity derived from the quadrature two-stream approximation (Toon et al. 1989). In this approximation the intensity is approximated as $I_\nu = A_\nu + B_\nu\tau$ where A_ν and B_ν are both constants, and the radiation field by two streams directed in opposite directions at angles $\mu = \pm\frac{1}{\sqrt{3}}$. The hemispheric mean approach is used to define the phase function, assigning a value P = 1 + g in the forward hemisphere and P = 1 - g in the backward hemisphere. The upward I_ν^+ and downward I_ν^- intensities for each layer are then calculated and inserted in the integral in Eq. (2.38), leaving the resultant source functions $S_\nu^\pm$ in the form

$$S_\nu = Ce^{\lambda\tau} + De^{-\lambda\tau} + E + F\tau, \tag{2.46}$$

where $\lambda = \sqrt{3(1-\tilde{\omega}_\nu)(1-\tilde{\omega}_\nu g)}$ and C, D, E, and F are all constants. The radiative transfer integral is then solved to arrive at the flux through the top and bottom of the model. The upward-directed flux from the highest atmospheric level is then calculated using Gaussian quadrature points for the incident angle μ_0 to allow direct integration of the geometric albedo.

2.4.2 Adding-doubling

The adding-doubling technique derives from the interaction principle, which states that two layers can be combined if the optical characteristics of each are known by calculating the reflection between layers as seen in figure 2.4 (Hansen and Travis 1974). The combination process of the two layers is known as adding. The reflection from two layers R has three terms, reflection from the upper layer, and the upward reflection and pure attenuation of the upward diffuse component U,

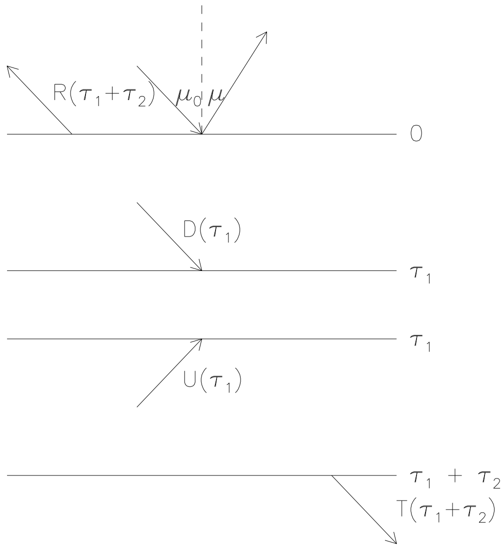

Figure 2.4: At any point on the planetary disc, the incoming radiation arrives at an angle μ_0 and departs at angle μ. The adding technique uses the interaction principle to determine the combined reflectivity R and transmission T of a component layer comprised of layers with optical depths τ_1 and τ_2, shown physically separated for effect. At the boundary between the layers is an upward diffuse field U and a downward field D.

$$R(\tau_1 + \tau_2) = R_u(\tau_1) + U(\tau_1)e^{-\tau_1/\mu} + T_u(\tau_1)U(\tau_1). \tag{2.47}$$

The subscripts 1 and 2 refer to the upper and lower layers respectively. In the reflection and transmission components R and T, the u and d subscripts refer to the direction of the reflection or transmission. For a homogeneous layer like those used in this study these terms are identical and are included here merely for completeness. U(τ_1) refers to the upward diffuse component at τ_1, or at the layer intersection. The combined transmission T of a layer is also dependent upon three terms. They are the components of emission that are not scattered by the upper layer but merely attenuated that is diffusely transmitted by the lower layer, and the portions of the downward diffuse component that are attenuated by and diffusely transmitted by the lower layer,

$$T(\tau_1 + \tau_2) = e^{-\tau_1/\mu_0} T_d(\tau_2) + D(\tau_1) e^{-\tau_2/\mu} + T_d(\tau_2) D(\tau_1). \tag{2.48}$$

The key to both these relations is proper representation of the diffuse components U and D that are determined at the layer interface. The upward component consists of radiation that is reflected upwards by the lower layer. This radiation can either have been attenuated by the upper layer or be part of the downward component. The downward component is that radiation diffusely transmitted by the upper layer or that part of the upward component diffusely reflected by the upper layer,

$$U(\tau_1) = e^{-\tau_1/\mu_0} R_u(\tau_2) + R_u(\tau_2) D(\tau_1), \tag{2.49}$$

$$D(\tau_1) = T_d(\tau_1) + R_d(\tau_1) U(\tau_1). \tag{2.50}$$

Since these two equations are interlocked an iterative solution must be found. The key involves the convolution of the components reflected downward by the upper layer and upward by the lower layer Q_1,

$$Q_1 = R_d(\tau_1)R_u(\tau_2). \tag{2.51}$$

In this equation as well as many terms in those above two terms are convolved as follows

$$Q_1 = \frac{1}{\pi}\int_0^1\int_0^{2\pi} R_d(\tau_1)R_u(\tau_1)\mu d\mu d\phi. \tag{2.52}$$

If the equation for D is expanded, a pattern becomes readily apparent,

$$D_{i+1}(\tau_1) = T_d(\tau_1) + e^{-\tau_1/\mu}[Q_1 + Q_2 + Q_3 + \cdots] + [Q_1 + Q_2 + Q_3 + \cdots]T_d(\tau_1), \tag{2.53}$$

with Q_n defined as

$$Q_n = Q_1 Q_{n-1}. \tag{2.54}$$

By defining S as the summation of these terms D can be solved for and used as input to determine the upward component U and the R and T values for two combined layers,

$$S = \sum_{n=1}^{\infty} Q_n, \tag{2.55}$$

$$D(\tau_1) = T_d(\tau_1) + e^{-\tau_1/\mu_0}S + ST_d(\tau_1). \tag{2.56}$$

In almost all cases it is not necessary to sum more than 5 terms in the computation of S,

The next step in the process is to define reflection and transmission coefficients to begin the process. In the limit of single-scattering ($\tau \ll 1$) the first term in Eq. (2.38) becomes zero. It can also be shown that in this case the reflection and transmission coefficients are equivalent. Then the reflection coefficient R is defined as

$$I_{\nu,0}^{+} = \mu_o R F_\nu, \tag{2.57}$$

and

$$R = \frac{\tilde{\omega}_\nu \tau}{4\mu\mu_0}\left[1 - \frac{\tau}{2}\left(\frac{1}{\mu} + \frac{1}{\mu_0}\right)\right] P(\cos\Theta). \tag{2.58}$$

A large homogeneous region can then quickly be computed by continually adding two layers of equal optical depth, and then adding two of the resultant layers until the desired depth is reached. This is known as the doubling technique. In this manner a inhomogeneous atmosphere can be constructed by using the doubling technique to rapidly create a few homogeneous layers that are then added.

The convolution process is discretized by evaluating the variables over a two-dimensional matrix R(μ, μ_0) where μ and μ_0 are chosen to be Gaussian quadrature points. The number of terms necessary to be stored quickly accumulates unless the phase function can be derived in terms of a Fourier series, using the property

$$\int \cos mx \sin nx dx = 0, m \neq n. \tag{2.59}$$

A Fourier series is defined as a series of coefficients a and b that are used upon successive sin and cos terms to represent a function f,

$$f(x) = \frac{a_0}{2} + \sum_{n=1}^{\infty} a_n \cos nx + \sum_{n=1}^{\infty} b_n \sin nx. \tag{2.60}$$

The Henyey-Greenstein phase function is even however, allowing for the sin terms to be discarded and the a coefficients calculated,

$$a_n = \frac{1}{\pi} \int_0^{2\pi} f(t) \cos nt dt. \qquad (2.61)$$

Substituting Eq. (2.14) for the function f(t) allows the final form to be arrived at,

$$a_n = \frac{A\tilde{\omega}_\nu}{\pi} \int_0^{2\pi} \frac{\cos nt dt}{(1 + B\cos t)^{1.5}}, \qquad (2.62)$$

where

$$A = \frac{1 - g^2}{(1 + g^2 + 2g\mu\mu_0)^{3/2}} \qquad (2.63)$$

and

$$B = \frac{2g(1-\mu^2)^{1/2}(1-\mu_0^2)^{1/2}}{1 + g^2 + 2g\mu\mu_0}. \qquad (2.64)$$

The total reflectivity is then calculated by running the model for each term of the phase function series and then summing. In most circumstances no more than 20 Fourier terms need to be carried to maintain errors under 1%. The Rayleigh phase function is simpler to represent, exactly described by 3 terms

$$P_0(\cos\Theta) = \frac{3}{4}\left[1 + \mu^2\mu_0^2 + \frac{1}{2}(1-\mu^2)(1-\mu_0^2)\right], \qquad (2.65)$$

$$P_1(\cos\Theta) = \frac{3}{4}\left[2\mu\mu_0(1-\mu^2)^{1/2}(1-\mu_0^2)^{1/2}\right], \qquad (2.66)$$

and

$$P_2(\cos\Theta) = \frac{3}{4}\left[\frac{1}{2}(1-\mu^2)(1-\mu_0^2)\right]. \qquad (2.67)$$

2.5 Observing

All experimental measurements used in this work were acquired by measuring the flux from astronomical bodies by using telescopes. The following sections detail the instruments used and the techniques involved into reducing the data from its raw form.

2.5.1 Infrared Observing

For the ground-based infrared observing two telescopes were used. First was the ARC 3.5m telescope at Apache Point Observatory in Sunspot, New Mexico, using the camera GRIM II, a 256×256 HgCdTe array sensitive from 1-2.5 μm. Second was NASA's 3 meter Infrared Telescope Facility (IRTF) at Mauna Kea Observatory in Mauna Kea, Hawaii using NSFCAM, a 256×256 InSb camera sensitive from 1-5.5 μm.

The quality of observations at an observatory can be quantified by its seeing. The seeing describes the dispersion of a point source over the detector, measured by the full width at half maximum (FWHM) of a Gaussian fit to the resultant point spread function (PSF). The two major contributors to the PSF are atmospheric turbulence and telescope and detector system effects. Because the PSF components are generally very near a Gaussian, their FWHM's add in quadrature. The diffraction contribution is dependent upon the telescope mirror diameter D, where the FWHM of the smallest resolvable angle is $1.22\ \lambda\ D^{-1}$. In the optical and near-infrared very little resolution can be gained by using a mirror with diameter greater than half a meter. The benefit however is in lowered required integration time, which scales as D^{-1}. Although the amount of object photons detected increases with the area of the telescope, the noise scales with the square root of the area, leaving the ultimate signal-to-noise ratio varying as D. The prime contributor is then small-scale turbulence in the atmosphere over the time of observation. This can be minimized by proper selection of the telescope site, ideally in dry air (to minimize water vapor absorption) at high altitudes (to minimize the amount of atmosphere to interfere and be above much of the water vapor, which condenses low in the atmosphere). The third major effect comes from the telescopic system, from jittering of the secondary mirror, to excess emission from an improperly-cooled telescope, to finite pixel sizes, to many other effects.

Figure 2.5 shows the very different effects created by observations at these two observatories. The measured median FWHM at the IRTF is $0.55''$, whereas the median FWHM at APO during the time of observations was near $1.5''$ due to some of the reasons listed above. In the lower left is a simulation of the Uranian disk and ring system, each with equal intensity, which is typical in the dark bandpasses longward of 2 μm. The middle row shows this simulation smeared with PSF's from (left) the IRTF, and (right) APO. The upper row includes the contribution of simulated noise. As can seen at this particular aspect of the ring system it is impossible separate the rings of the planet using observations at APO, demonstrated in the image at the lower right, a typical image acquired using a 1.99 μm filter, a good match to the panel in the upper right. The additional three point sources are the Uranian moons, which are very competitive compared to the planet in these filters.

The process of reducing the telescopic images to useful data involves the removal of all contributions to the final image except that from the source and then correcting to make the chip response uniform. The individual pixels then contain a signal S_i,

$$S_i = \alpha N_{o,i} + \alpha N_{s,i} + \alpha D_i + B_i + A_i, \tag{2.68}$$

of which the individual components are α, the conversion factor from the electrons produced by the incoming signal to the "analog-digital units" the system measures, $N_{o,i}$, the number of electrons produced by the object, $N_{s,i}$, the number of electrons produced by the background sky, D_i, the number of electrons produced by dark current, B_i, the camera bias, and A_i, individual artefacts, of which each will be explained shortly.

The camera array must initially be charged to a certain voltage level before it can be used. This initial voltage creates a background level known as a bias that has slight variance from pixel to pixel. In optical observing this level can be determined by taking a zero second exposure with the shutter closed. However GRIM II does not have the capability to do either, so the bias must be accounted for in determining the dark current. The dark current comes from thermal emis-

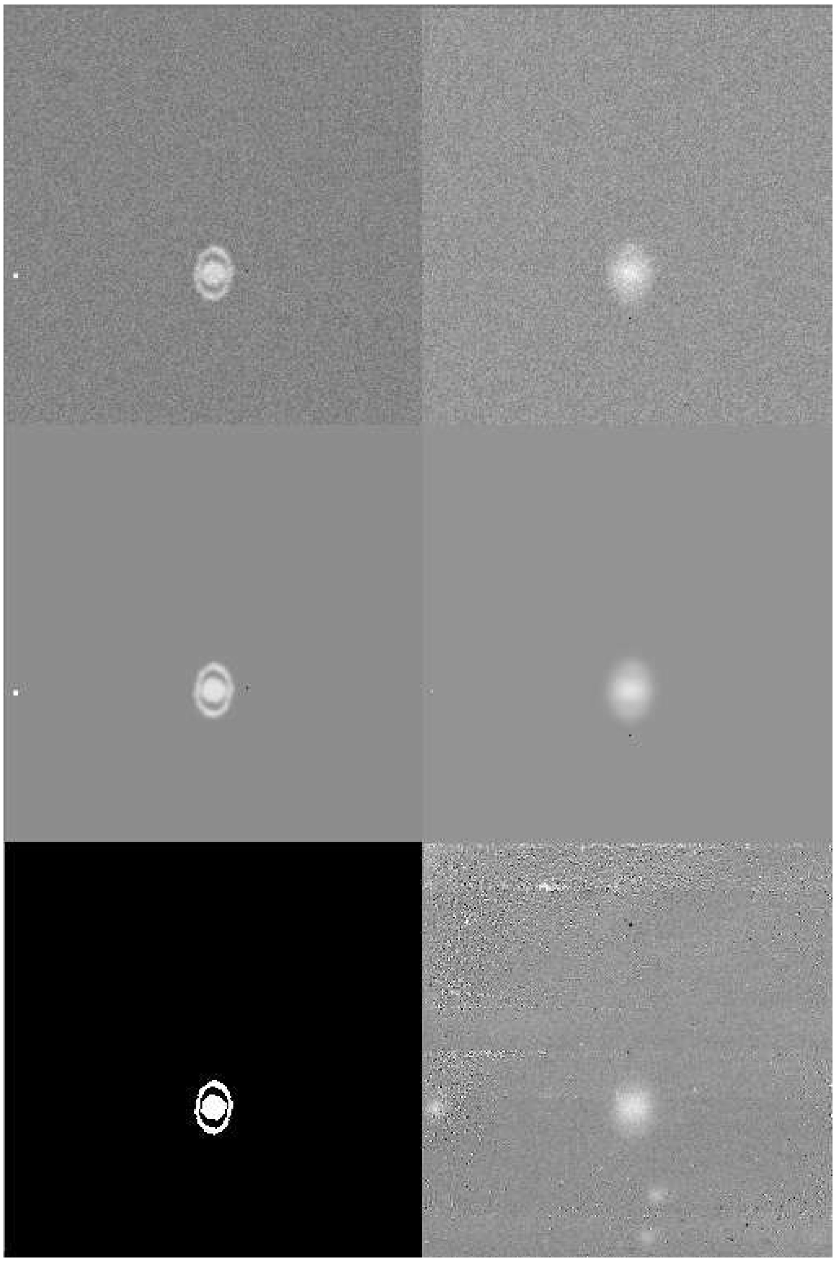

Figure 2.5: An examination of the deleterious effects of observing Uranus at Apache Point Observatory (APO) and at NASA's Infrared Telescope Facility (IRTF). The panel at lower left shows a simulation of the locations of Uranus and its ring system as seen from Earth during the period of observation. The middle panels represent the effects causes by convolving this image with a Gaussian with FWHM equal to the typical seeing disks at IRTF (left) and APO (right). In the upper panels simulated noise has been added to these images. Finally in the bottom right is an actual APO image with a 1.99 μm filter, similar to the panel at upper left.

sion from the instrument during the exposure and as such scales linearly with time. Dark frames are taken with GRIM II by placing a dark filter in front of the shutter. In order to subtract the dark and bias currents then, it is necessary to take dark exposures with the same integration time as the object images. In case the effect changes over the time, it is advisable to take this data both at the beginning and end of each observing run, in the twilight hours when no object data can be acquired.

In the near-infrared the sky is a significant background source with typically 2 orders of magnitudes more photons than in the optical. After each group of object exposures then it is desirable to shift the telescope a small distance (say $2'$) from the object and take an identical group of exposures. The first step in data reduction is then to subtract this image from the object, which in the process also removes the dark and bias contribution.

The next step is then to flat-field, i.e., to make the pixel to pixel response as even as possible. For this purpose it is necessary to use all the sky frames taken over the night with each filter, dark subtract them, and then use a median filter to arrive at a median image for the night, which is then divided to make the average pixel value 1. Assuming the relative response of each pixel remains constant over the night, dividing the object image by this image then corrects for the pixel-to-pixel variances without changing the total number of counts.

The final step is to correct for the artefacts, A_i. These can come from either of two sources. On any chip a number of pixels can be referred to as "bad", either they are not responsive to incoming radiation, or are unpredictably responsive. In addition, over the course of time incoming cosmic rays may interact with the array, providing spurious hits. If the observer is properly over-sampling (the camera is designed so that the PSF is greater than 1 pixel), these can easily be seen as 1 pixel hot spots. All artefacts are then removed by nearest neighbor interpolation, median filtering the surrounding 8 pixels.

The standard reduction procedure for infrared observing is then

1. Sky subtract

2. Flat-field

3. Remove artefacts

At this point the individual images can be shifted to a common center and co-added. Once the data has been reduced to this point, it must be calibrated with a known source to derive photometric sources. The procedure for this is to observe an object of known brightness and non-variability, typically a high brightness dwarf star, and perform the same reduction technique. The total number of counts from star to object is then ratioed to give the final flux. This technique is useful in that it removes from consideration the quantum efficiency of the telescope and camera. However it is important to observe the star over as many different airmasses as possible to construct an accurate extinction curve so that the star flux can be corrected to be at the same airmass as the object.

The reduction procedure for the IRTF data was nearly identical except for the flat-fielding procedure. In this case "dome flats" were used to obtain the pixel-to-pixel variations. The observatory dome was observed with the lights on and off. The images for each filter were then median filtered and the variations determined by subtracting the "lights off" image from the "lights on" image and renormalizing the result.

2.5.2 HST

The dataset of this study has been augmented by the addition of images acquired with the Hubble Space Telescope (HST) in the timespan between the first refurbishment (installation of WFPC2) and second refurbishment (installation of NICMOS). Data acquired by HST has the highest spatial resolution achievable from Earth because the telescope is located in Earth orbit above virtually the entire atmosphere, so that its imaging is nearly diffraction-limited by the 2.4 meter diameter mirror.

The data was acquired with the Wide Field and Planetary Camera 2 (WFPC2), a camera designed to correct for the imperfections in the HST mirror discovered after launch. Thus image deconvolution is largely unnecessary. WFPC2 consists of four 800×800 CCD's as shown in figure 2.6 that are sensitive from 0.12 to 1.1 μm. The chip in the upper right is the Planetary Camera (PC) chip, which is designed for high resolution studies, having a sampling 2.2 times that of the other

Wide Field (WF) chips. A residual of the original WF/PC design can be seen in two special quad filters, FQUVN and FQCH4N. Both filters consist of four separate filters joined together. Because they were designed for different alignments, the filters must be tilted to get the desired filter over the desired chip. Since it may not cover the entire chip special care must be taken with the alignment. Some filters are not possible to use on the PC chip in any rotation.

All data taken with HST remains in proprietary status for one year after the observation date. Following this the data becomes public domain, and goes into an archive that can be used by any astronomer. The data can be received in raw or calibrated form, with the calibrated data already having been bias and dark-subtracted and flat-fielded.

In February 1997 HST underwent a second refurbishment, which included the installation of the Near-Infrared Camera and Multi-Object Spectrograph (NICMOS). Although the multi-object spectrograph was removed in the design process, the camera still serves as a diffraction-limited near-infrared camera with a 256×256 HgCdTe array sensitive from 0.8 to 2.5 μm.

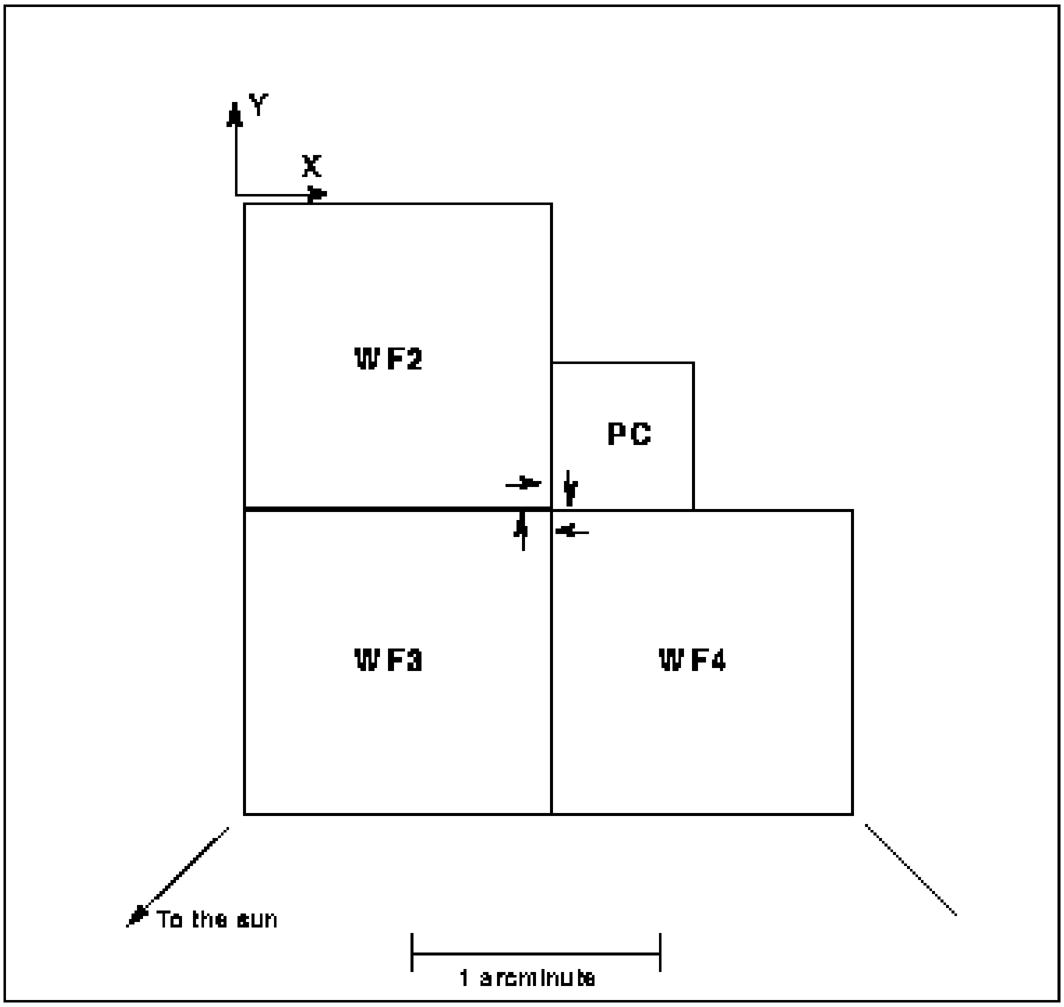

Figure 2.6: A diagram from the HST manual v4.0 (Biretta 1996) showing the layout of the four chips in the WFPC2 camera, and their orientation. Although the PC chip is in the same 800 x 800 format, it has higher resolution, which causes it to examine a smaller field of view.

Chapter 3

THE NEAR-IR ALBEDO OF URANUS IN 1996

3.1 Introduction

Since the 1970's it has been recognized that several scattering layers in the Uranian atmosphere were required to explain the observed spectral features. Binder and McCarthy (1972) postulated the existence of a CH_4 condensate layer and Savage and Caldwell (1974) showed that high altitude hazes could be used to explain an ultraviolet albedo lower than that predicted of a clear Rayleigh-scattering atmosphere. The required scattering layers are located higher in the atmosphere than the optically thick cloud deck typically used to define the bottom of the visible atmosphere. Current atmospheric models are largely based upon data taken in the next decade, both from ground-based observatories and the Voyager 2 flyby in 1985/1986. Pollack et al. (1987) used the Voyager high phase angle imaging along with microphysical coagulation models to constrain the profile of stratospheric hazes and placed limits on the size of the CH_4 ice particles. Baines et al. (1995a) analyzed the H_2 quadrupole and CH_4 absorption features measured by ground-based spectroscopy in the red to constrain the tropospheric CH_4 mixing ratio.

Prior to 1994 Uranus presented a featureless disk to ground-based observers, but this has changed in the intervening years. Hubble Space Telescope Observations of Uranus on August 14, 1994 show a high altitude haze covering the south polar region (Zellner et al. 1994). This feature was seen in subsequent ground-based observations (Baines et al. 1995b, Walter and Marley 1995), and by another HST program on July 3, 1995 (Walter et al. 1997, in preparation).

Uranus is unique among the planets of our solar system in that its rotation axis is inclined 98° to the ecliptic, resulting in essentially 42 consecutive years of continuous sunlight alternating on each hemisphere. The haze material is thought to largely consist of hydrocarbons created by UV photolysis of CH_4 (Atreya et al. 1991). The increased sunlight being received at the south pole due to the summer solstice of 1986 should have resulted in an increase in the column density of haze particles. Disk-averaged brightness changes in Uranus are documented to have previously occurred, i.e., Lockwood et al. (1983) found a 14% increase in the visual albedo between near-equatorial observations in 1963 and 1981 at a sub-earth latitude of -68°.

All these results have been derived from observations of the planet in the visible, but by observing in the near-infrared beyond 1 μm we can improve upon current atmosphere models in two distinct areas. The grains that make up the tropospheric cloud are thought to be of the order of 1 μm (Rages et al. 1991). in size, giving a scattering size parameter ($x=2\pi r/\lambda$) ranging from 2 to 7 over the 1–2.5 μm regime. The scattering efficiency Q_{ext} varies substantially over these size parameters. Mie theory can thus constrain the mean particle size. In addition, the molecular gaseous absorption bands of CH_4 and H_2 are stronger in the near-IR. This allows greater sensitivity to the properties of the stratosphere.

Here we report on observations aimed at achieving a better understanding of the overall properties of scatterers in the Uranian atmosphere, and their temporal variation. We measured the planetary geometric albedo using several narrowband filters in the near-IR, and then used this data as the primary constraint for a new atmospheric model. This is the first attempt to use near-IR data to examine the atmospheric properties since the work of Fink and Larson (1979),who examined a planetary spectrum with a FWHM resolution of 3.6 cm^{-1}. They found that the extinction in these bands from gaseous absorption is so high that Rayleigh scattering is still an important source of scattered photons even as far in the infrared as 1.5 μm. By choosing our filters to cover varying intensities of H_2 and CH_4 absorption bands as well as continuum wavelengths, we are able to probe effectively the stratosphere and upper troposphere of the atmosphere to derive our model. In section 2 we describe our observations and the photometric techniques used in our albedo measurements. We present our model and the representation of the various atmospheric constituents in section 3. Our results are given in section 4, and finally, section 5 discusses their implications.

3.2 Observations

The data presented here were acquired using the Astrophysical Research Consortium 3.5 m telescope at Apache Point Observatory in Sunspot, NM. Using the GRIM II HgCdTe 256 $\times$ 256 array, which is sensitive from 1.0-2.5 μm, we observed Uranus and the near-IR standard star Gl811.1 (Elias et al. 1982). The dates of observation, phase angles, filters used, total integration times, and median seeing FWHM are given in Table 3.1. In f/10 mode, the plate scale is 0.236$''$/pix, meaning Uranus typically subtends a diameter of 15 pixels, with a FWHM resolution disk 7 pixels in diameter. Data were sky and dark-subtracted, flat-fielded and corrected for the non-linearity of the camera. Multiple exposures in each filter were co-added. Bad pixels and cosmic ray hits were corrected for by nearest-neighbor interpolation. Continuum images from all 3 dates are shown in Figure 3.1.

Because our observations were taken near opposition, with phase angles $< 3°$ no correction for the phase angle is used when calculating the geometric albedo. The solar spectrum at 1 AU is given in the tables of Labs and Neckel (1968).

Figure 3.1: Observations of Uranus at three recent epochs by the ARC 3.5 m telescope displayed as filled contour maps. In the bottom panel is an H-band image taken on August 12, 1995, showing asymmetry in brightness in the south polar region. The middle panel is an image with the same filter taken on June 6, 1996, showing a smooth disk. On the top a narrowband 1.28 μm filter was used to image the planet on October 30, 1996, again showing a smooth disk. The images are rotated so that north is on top.

Table 3.1: Total exposure time are given in seconds. A blank space indicates that no observation was made. FWHM was measured using the standard star

Filter	August 12, 1995	June 5, 1996	October 30, 1996
1.28 μm			60
1.58 μm	360	150	
1.70 μm		125	
1.99 μm		600	
2.12 μm			600
2.25 μm		700	
2.36 μm		220	210
FWHM	1.7″	1.7″	1.5″
Phase angle	1.0°	2.2°	2.8°

3.2.1 Photometry

To find the DN for the sun we multiplied the stellar standard's DN by the ratio between the known solar flux (Labs and Neckel 1968) and the standard star, for which broadband H and K fluxes were available as well as a CO and H_2O index, to account for the stellar absorption by these molecules at narrowband filters similar to our own at 2.36 and 1.99 μm (Elias et al. 1982). For the other narrowband filters we linearly interpolated the star's magnitude using the broadband values.

The initial flux we measured includes contributions from the planetary disc as well as the smeared ring system. Photometric errors in this value can be determined by knowing the errors inherent in the observations of Uranus and the standard star, while neglecting the errors in the knowledge of the distance and radius of Uranus, which are comparatively well-established. The radius used is 25450 km, which is recommended by the International Astronomical Union

(Davies et al. 1995). While our observations probe a slightly lower pressure than the 1 bar level used to determine this radius, use of this radius is necessary for comparison with other works.

The error $\Delta\mathrm{DN}_U$ is determined by adding in quadrature the Poissonian noise with the uncertainty in measurement. For $\Delta\mathrm{DN}_*$ the Poissonian noise is replaced by the known flux uncertainty of the standard, 0.015 mag (Elias et al. 1982). The observations of October 30, 1996 were hindered by a variable sky level, so it was necessary to calibrate the planetary observations by using the known moon reflectances. We compared broadband K images of the moon Ariel taken on June 5, 1996 in photometric conditions with those taken in the October run. Ariel was the only moon that was present in both images and had published reflectances over the entire wavelength range (Brown 1983, Brown and Cruikshank 1983). For this data Ariel then replaces the standard with a three component error, the reflectance error of 10% along with the photometric errors in both observations. Resultant pre-ring-subtraction albedos and errors are listed in Table 3.2. Other photometric uncertainties less than 2% include the uncertainty in the extinction curve, non-linearity correction, the published solar fluxes, and timing errors for short exposures. The variation of the moon's reflectivity from opposition to the phase angles observed in this work can in extreme cases be as much as half a magnitude. For the 2.12 and 2.36 μm bandpasses this effect on the results is less significant due to the already high errors in photometry and modeling, but it remains an additional source of error for the 1.28 μm data.

Table 3.2: Albedos before and after ring subtraction

Filter	initial albedo	corrected albedo
	August 12, 1995	
1.58 μm	$(9.3 \pm 0.4)\times10^{-2}$	$(9.3 \pm 0.4)\times10^{-2}$
	June 5, 1996	
1.58 μm	$(8.8 \pm 0.2)\times10^{-2}$	$(8.8 \pm 0.2)\times10^{-2}$
1.70 μm	$(1.09 \pm 0.03)\times10^{-3}$	$(8.1 \pm 0.5)\times10^{-4}$
1.99 μm	$(1.6 \pm 0.03)\times10^{-3}$	$(1.3 \pm 0.1)\times10^{-3}$
2.25 μm	$(4.5 \pm 0.2)\times10^{-4}$	$(1.6 \pm 0.4)\times10^{-4}$
2.36 μm	$(5.7 \pm 0.4)\times10^{-4}$	$(2.8 \pm 0.6)\times10^{-4}$
	October 30, 1996	
1.28 μm	$(9.4 \pm 1.3)\times10^{-2}$	$(9.4 \pm 1.3)\times10^{-2}$
2.12 μm	$(6.0 \pm 0.8)\times10^{-4}$	$(3.0 \pm 0.9)\times10^{-4}$
2.36 μm	$(4.2 \pm 0.9)\times10^{-4}$	$(1.2 \pm 0.9)\times10^{-4}$

We chose seven filters that were available with the GRIM II instrument, narrowband filters centered at 1.28, 1.58, 1.70, 1.99, 2.12, 2.25, and 2.36 μm. Transmission curves at room temperature and at the detector operation temperature of 77 K were available for all filters except the 1.99 μm filter, which has identical values to the 1.58 μm filter but stretched to fit the greater FWHM. The filter centers and FWHM are given in Table 3.3.

3.2.2 Ring subtraction

For filters in which the planet is dark (typically those with albedos less than 10^{-3}), smearing of the planetary disc with the ring system due to the large PSF created a significant source of error and prevented direct removal of the rings. The ring contribution was modeled using the derived effective ring location, radius, and

Table 3.3: Filter characteristics

Name	center (μm)	FWHM (μm)
Pa β	1.2823	0.0146
Narrow cont.	1.580	0.010
Methane	1.700	0.050
Steam	1.99	0.02
H2 $\nu = 1 \rightarrow 0$ S(1)	2.122	0.028
H2 $\nu = 2 \rightarrow 1$ S(1)	2.2485	0.0239
CO Band	2.36	0.09

albedo of Nicholson and Jones (1980) scaled to the appropriate geometry. The ring system projects an ellipse upon the sky depending upon the sub-earth latitude θ at the time of observation, where a is the semimajor axis along the equatorial plane, and b = a sin θ. Then the effective cross-sectional area S is π sin θ (a_2^2 - a_1^2) where a_2 and a_1 are the Nicholson and Jones' effective ring edge radial distances, determined by the effective width. An effective spherical radius can then be determined as $R_{eff} = \sqrt{S/\pi} = \sqrt{\sin\theta(a_2^2 - a_1^2)}$. The contribution from the ring can then be determined using the relation

$$A_r = a_r \left(\frac{R_{eff}}{R_U}\right)^2 = 4.03\times10^{-4} sin\,|\theta| \tag{3.1}$$

where A_r is the contribution to the total albedo from the rings, and a_r the albedo of the ring particles themselves, a constant within 5% over the range 2.1–2.5 μm. This approach has one dominant source of error, the ring albedo for which we use $3.0 \pm 0.4\times10^{-2}$. The albedo correction for each night and corrected albedo values are given in Tables 3.2 and 3.4.

Table 3.4: Ring corrections

Date	θ	albedo correction
August 12, 1995	-51.0	$3.14 \pm 0.44 \times 10^{-4}$
June 5, 1996	-44.6	$2.83 \pm 0.40 \times 10^{-4}$
October 30, 1996	-47.9	$2.99 \pm 0.42 \times 10^{-4}$

3.3 Model

The geometric albedo model was modified from the original of McKay et al. (1989), which uses the Eddington source method of Toon et al. (1989) to compute the upward and downward monochromatic fluxes through 35 plane-parallel layers spaced approximately evenly in log P, where P is pressure. This technique is useful as it allows for rapid flux computation, and the flux errors of this approximation do not exceed 11% (Toon et al. 1989), which is typically more accurate than our knowledge of gaseous absorption coefficients and the photometry. The majority of the modifications were made my my advisor Mark Marley, with my work concentrating on developing the techniques to more accurately treat the near-infrared spectrum.

In this model, we examine the effects of six opacity sources - Rayleigh scattering, scattering and absorption from stratospheric hazes, two tropospheric clouds, and H_2 and CH_4 gas absorption. The temperature profile is that derived from the Voyager 2 RSS experiment (Lindal et al. 1987), shown in Figure 3.2. In Table 3.5 we list the free parameters explored in the analysis.

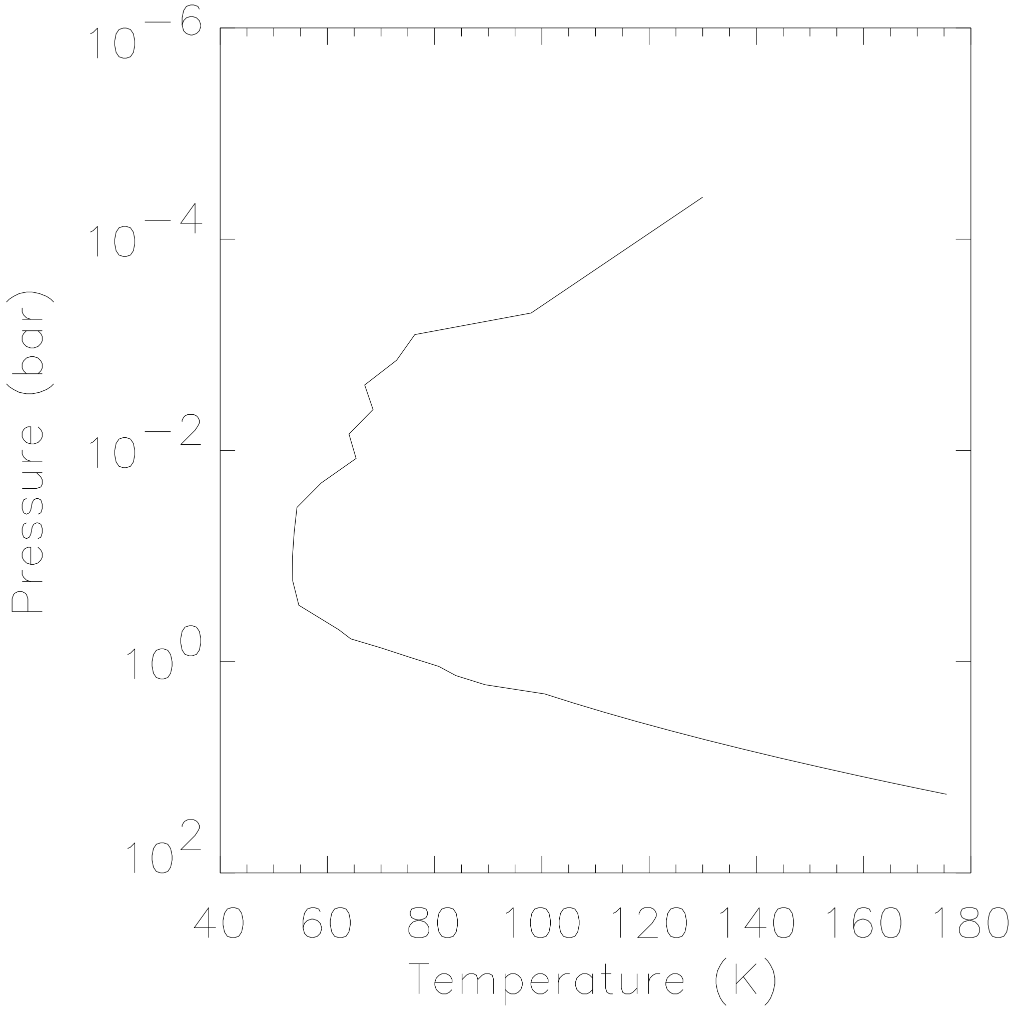

Figure 3.2: The pressure-temperature profile used by the model. Data is taken from the Voyager 2 RSS experiment results (Lindal et al. 1987).

Table 3.5: Free parameters

n_i	Haze imaginary index of refraction
f_{hze}	Haze column density scaling factor
$f_{CH_4,s}$	Stratospheric CH_4 mixing ratio
P_{cld}	Pressure of CH_4 cloudtop
τ_{cld}	Optical depth of CH_4 cloud
τ_{cld2}	Optical depth of lower cloud
$\tilde{\omega}_{cld2}$	Single-scattering albedo of lower cloud

3.3.1 Scatterers

Rayleigh scattering

Rayleigh scattering is treated as in Hansen and Travis (1974) and Raman scattering as in Rages et al. (1991), and is not allowed to increase the single-scattering albedo of any layer above 1. Contributions of the dominant constituents, H_2, He, and CH_4 gas are used, with the refractive index given in the tables of Allen (1973).

Stratospheric haze

Direct evidence for hazes in the stratosphere was first seen in high phase angle Voyager images (Pollack et al. 1987). The subsequent analysis by Rages et al. (1991) yielded a multi-layer profile with the number densities, mean modal radius, and size distribution as a function of pressure. We interpolated these values to our own grid and used this model as a baseline. Because the haze is thought to consist of higher order hydrocarbons resulting from solar UV photolysis of CH_4 photons high in the atmosphere (Pollack et al. 1987), we represented the real index of refraction of the haze in each level as that of the expected dominant source, as shown in Table 3.6. The haze particles were modeled as spherical Mie scatterers, with the mean particle size and column densities scaled in efforts to fit the observations. Because high values of the imaginary index of refraction gave albedos grossly inconsistent with the observations we adopted a value of 5×10^{-3}.

Table 3.6: Haze constituents (Rages et al. 1991)

Pressure Top (bar)	Pressure Bottom (bar)	Real index of refraction	substance
0	2.4×10^{-3}	1.42	C_4H_2
2.4×10^{-3}	12×10^{-3}	1.33	C_2H_2
12×10^{-3}		1.44	C_2H_6

CH_4 cloud

Prinn and Lewis (1973) demonstrated that there could be a thin cloud layer at 1 bar by fitting the geometric albedo in the visible and near-infrared. By comparing the spectral observations in bands both sensitive and insensitive to CH_4, Baines (1983) and Baines and Bergstralh (1986) showed that there was an order of magnitude more haze than could be accounted for in the sensitive bands, confirming it as the likely makeup of the cloud. By analysis of the bifurcation of the RSS radio signal, Lindal et al. (1987) determined the CH_4 cloud top to be at 1.2 bar. We modeled this cloud using Mie theory for a distribution of CH_4 spherical particles centered at 1 μm. Although this value is poorly constrained it contributes very little to the model error unless the true value is drastically smaller, as the total optical thickness is a free parameter, particles of this size or greater are largely forward-scattering and nearly conservatively scattering in the absence of great impurities in the cloud that are interacting at these wavelengths.

Although the formation mechanisms of the stratospheric and CH_4 hazes are different, for the CH_4 we used a log-normal size distribution equal to that in the lower levels of the stratospheric haze. The optical properties were taken from Pearl et al. (1991) for phase I CH_4 at 30K. Further constraining the absorptive characteristics of this cloud was prevented by the fact that atmosphere is already optically thick upon encountering the cloud at those wavelengths where CH_4 is absorbing (see Figure 3.3). We examined the effects of moving the cloudtop higher in the troposphere and varying the number density of particles by scaling the total optical extinction.

Lower cloud

Thermochemical arguments suggest that the lower cloud consists of H_2S ice. NH_3 condenses out near 10 bars (Weidenschilling and Lewis 1973), with a lower cloud consisting of NH_4SH. NH_3 is severely depleted in the lower troposphere (Gulkis et al. 1978), while the models of de Pater et al. (1991) show that H_2S is enriched by two orders of magnitude over solar abundance.

Herzberg (1952) analyzed the properties of molecular hydrogen in an effort to explain the results of Kuiper (1949), who measured an absorption feature at 0.83 μm, the location of the H_2 3-0 quadrupole. In his study Herzberg calculated that the visible atmosphere consisted of 2 bars of H_2. Followup work involved

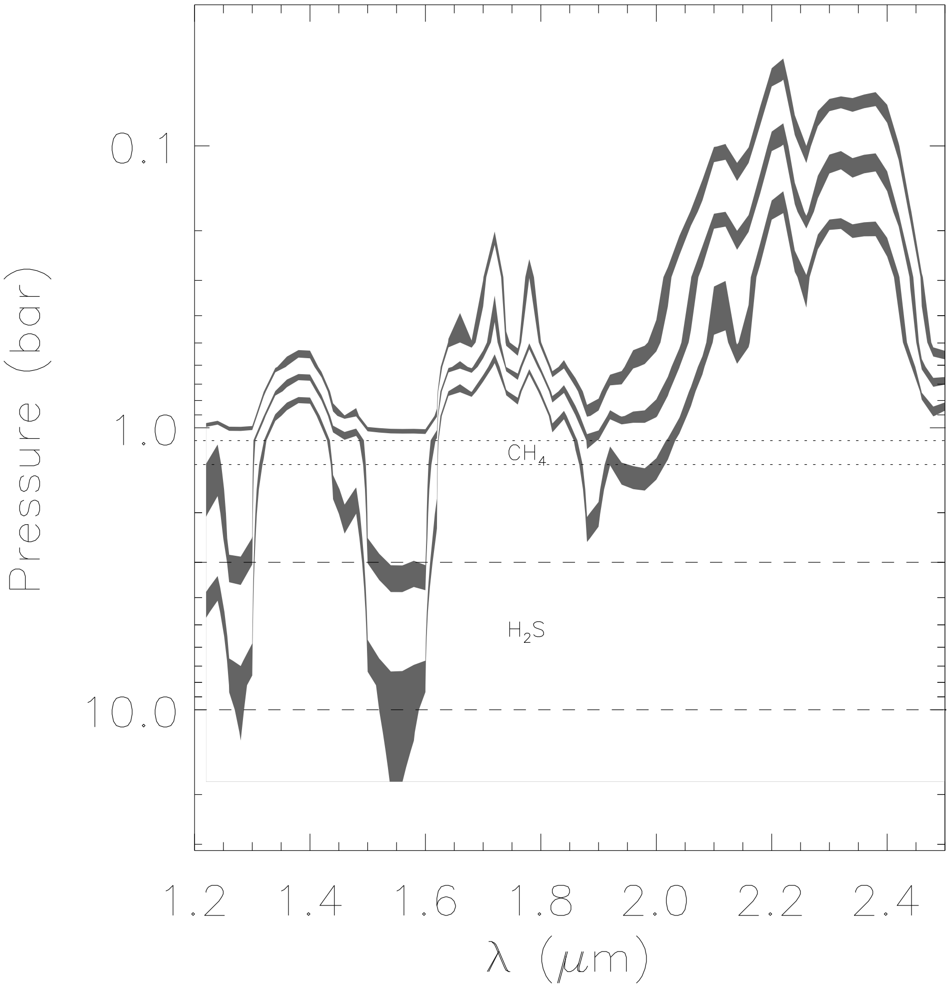

Figure 3.3: Optical depth is illustrated as a function of wavelength and pressure. From the top, the three lines represent where in the atmosphere incoming radiation encounters extinction optical depths of 1, 3, and 9. Line widths represent a $\pm$ 15% model error. The locations of the two tropospheric clouds as used in our model are indicated. Total optical thickness is computed from molecular absorption by H_2 and CH_4, stratospheric hazes, tropospheric clouds, and Rayleigh scattering.

the calculation of the equivalent width of the feature (Encrenaz and Owen 1973, Trafton 1976, Smith et al. 1980). By analyzing the observations of Trauger and Bergstralh (1981), Baines and Bergstralh (1986) were able to constrain the location of the lower cloudtop to between 2.4 and 3.2 bar. A later reanalysis using improved laboratory data changed the allowable region to be between 2.9 and 4.2 bar (Baines et al. 1995a).

Because of the uncertainties involved in higher atmospheric features, the scattering properties of this cloud were not well defined, so we took as free parameters the scattering asymmetry factor $\langle \cos \Theta \rangle$, the single-scattering albedo $\tilde{\omega}$, the column density of particles, and the pressure top of this cloud. The cloud was initially modeled as homogeneous and lying between 3 and 10 bar, with the optical depth in each layer proportional to the pressure difference in that layer.

3.3.2 Molecular absorption

$\mathbf{H_2}$

Conrath et al. (1987) determined the helium mole fraction in the upper troposphere to be 0.152 ± 0.033, which we take to be constant throughout the entire model. With CH_4 being the only other significant constituent, the rest of the atmosphere is modeled as H_2. The rotovibrational fundamental and first overtone of H_2 are located within our spectral region. We computed the absorption coefficients using codes provided by A. Borysow (Borysow 1991, Borysow 1992, Borysow and Frommhold 1989, Borysow et al. 1989, Zheng and Borysow 1995, Birnbaum et al. 1996) for H_2-H_2 and H_2-He collisions over our temperature range. These codes assume an equilibrium ortho to para hydrogen ratio, consistent with the previous observations (Hanel et al. 1986, Baines et al. 1995a). These codes are used from 1.3–1.8 μm, beyond the recommended wavelength range, however in these regions H_2 is an insignificant source of opacity.

CH_4

Methane absorption longward of 1.6 μm was treated by weighting the exponential sum absorption coefficients from the Baines et al. (1993) quasi-random narrow band model by their Gauss weights. They derived coefficients over a large pressure grid at three temperatures, 112, 188, and 295K. Because the near-IR behavior of methane is not well established at low temperatures, we use the low temperature (112K) values for all stratospheric and upper-tropospheric layers and interpolate between the 112 and 188K values otherwise. All values are interpolated on pressure and wavenumber grids, with resolution of 0.25 in log P and 10 cm^{-1} in wavenumber. Shortward of 1.6 μm we used the low temperature (190K) CH_4 absorption coefficients of Strong et al. (1993). These molecular band models were fitted to a Goody-Voigt random band model with a spectral resolution of 0.25 cm^{-1}, but are not pressure dependent.

The mixing ratio of CH_4 in the stratosphere is highly uncertain, and only upper limits can be set, assuming the fraction does not exceed that measured at the tropopause by Voyager. The tropopause saturation mixing ratio is 10^{-4}, however the RSS results show the equatorial mixing ratio to be only 30% of saturation. From spectral observation near the ν_4 fundamental band, Orton et al. (1987) set an upper limit on the disk-averaged stratospheric mixing ratio of 10^{-5}. Below the tropopause the Clausius-Clapeyron equation is followed assuming saturation until it reaches the observed tropospheric ratio of 2.3% derived from RSS results (Lindal et al. 1987). This equation relates the vapor pressure of a substance to the temperature and is of the form

$$\ln P = -\frac{\Delta H_{vap}}{RT} + C \tag{3.2}$$

where Δ H_{vap} is the molar heat of evaporation (9.2 kJ mol^{-1}) for CH_4, R the gas constant (8.314 J K^{-1} mol^{-1}), and C a constant.

3.4 Results

By obtaining albedo measurements in six separate filters we sounded various levels of the atmosphere. Figure 3.3 illustrates the effective extinction level of the atmosphere as a function of wavelength. The level where monochromatic extinction reaches optical depths of 1, 3, and 9 in our nominal model is shown. By choosing appropriate filters, various atmospheric levels can be probed. The light eventually seen takes contributions from all manner of scatterers. However, in the deepest molecular absorption bands, enough extinction has taken place so that contributions from the tropospheric clouds are negligible. In Figure 3.4 the extinction levels are computed for a clear atmosphere consisting only of gas. Beyond 2 μm our model is completely insensitive to the tropospheric scatterers.

We integrated the model results over the entire filter bandpass. A weighted average of 9 to 20 monochromatic points was used to determine the final result. Weights were chosen by using the average value of the effective transmission in each region. In Figure 3.5 the transmission of each filter is overlain with the best model albedos for comparison.

The filters can be broken up into three groups according to which region of the atmosphere they probe most effectively, the stratosphere group, the CH_4 cloud group, and the troposphere group. Figures 3.6-3.11 show the results using the albedos derived in each bandpass, obtained by varying the available relevant parameters for each band to compute the acceptable solution space. These results are contoured so that every possible value within the combined $1-\sigma$ photometric errors (see Table 3.2) and the radiative transfer code errors (which vary from 12% at continuum wavelengths to 40% in deep H_2 and CH_4 bands) is shaded.

3.4.1 Stratosphere

Since the near-infrared part of the electromagnetic spectrum is not home to any strong rotovibrational fundamentals, it is very unlikely that any haze constituent has a large imaginary index of refraction in the spectral regime covered by this work. Models with n_i less than about 1×10^{-2} were indistinguishable from conservatively scattering particles because the scattering efficiency Q_{scat} is nearly insensitive to n_i in this region whereas the absorption is insignificant. This model

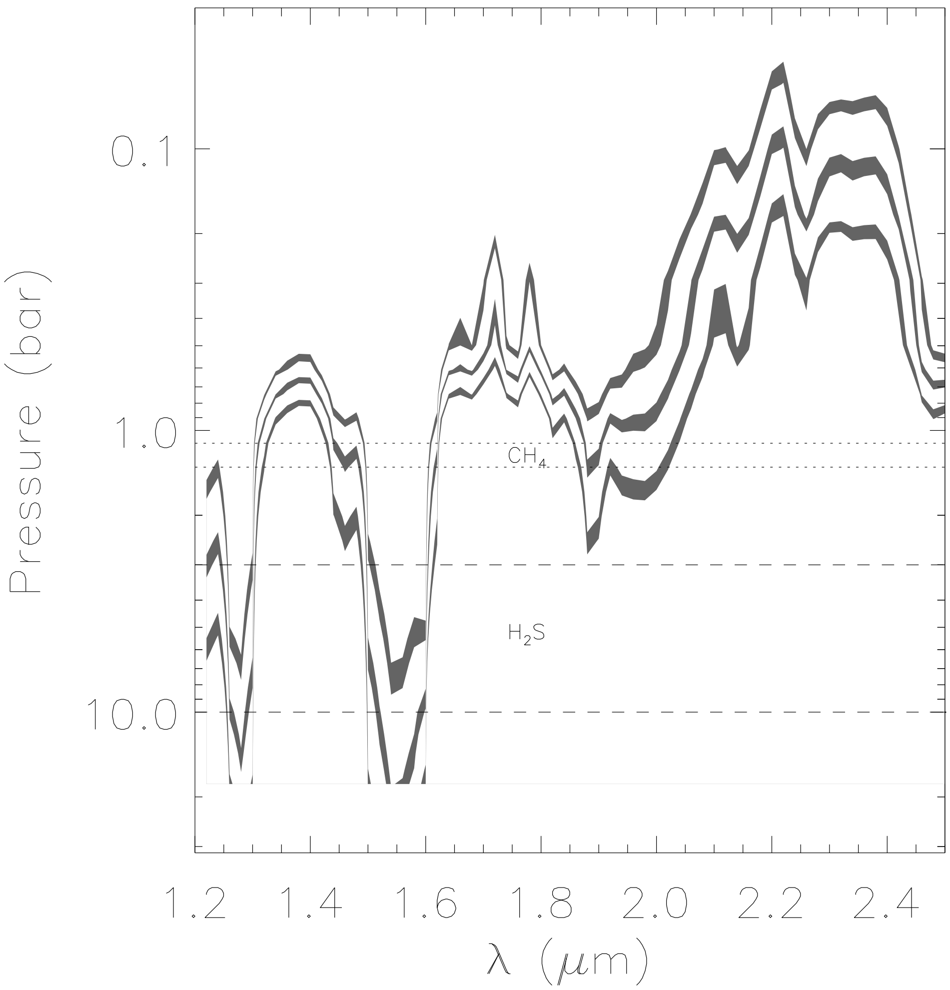

Figure 3.4: Similar to Figure 3.3, but only using the contributions from molecular absorption by H_2 and CH_4. The difference is only noticeable in the continuum regions probed by our 1.28 and 1.58 μm filters.

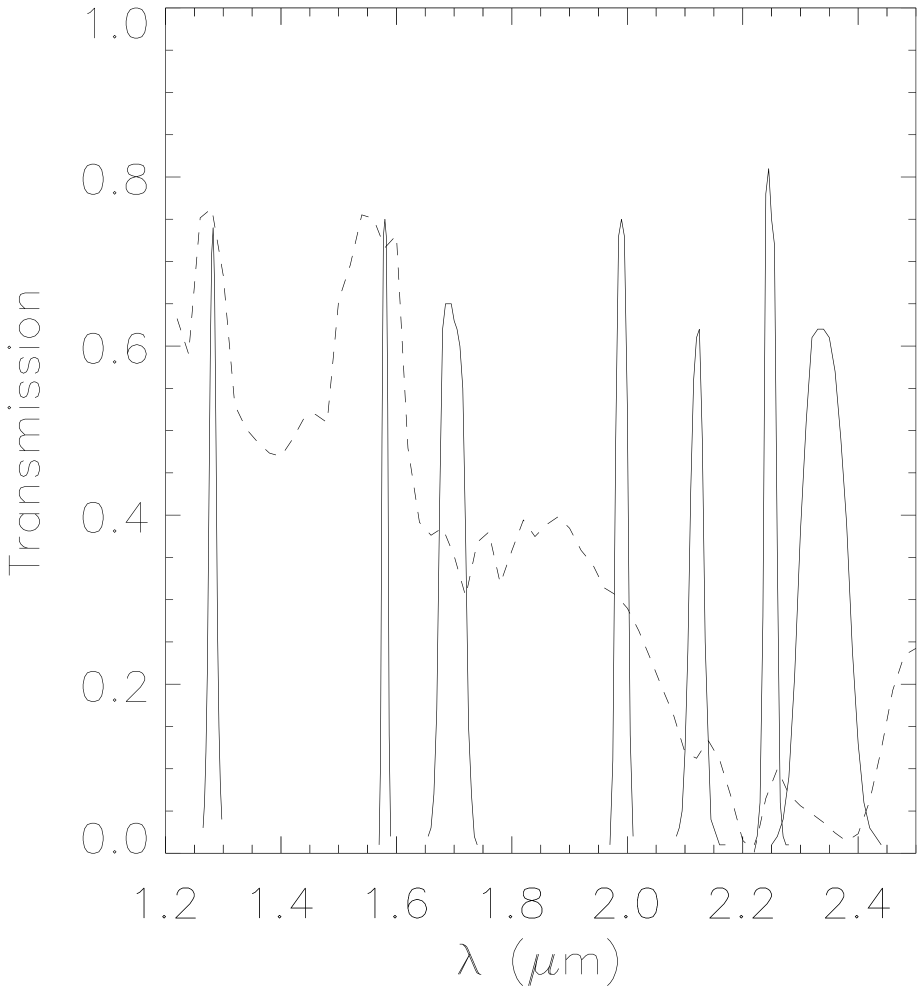

Figure 3.5: The transmission characteristics of the seven narrowband filters used in the study, centered at 1.28, 1.58, 1.70, 1.99, 2.12, 2.25, and 2.36 μm. The albedo spectrum of our best model is displayed logarithmically for comparison.

is then not sensitive to the optical characteristics of the haze. To account for this we chose a value for n_i of 5×10^{-3}.

It is difficult to determine the number of haze particles unless their relative size is known and vice-versa. An increase in mean particle size would mimic the effect of more haze, and a decrease could be interpreted as a lower column density. To test the likely effect of different particle sizes we computed the optical depth τ for a conservative Mie scatterer with various particle sizes (Figure 3.12). The total transmission $e^{-\tau}$ falls off essentially as λ^{-1}. Decreasing the mean particle size by a factor of 10 results in a decrease in scattering efficiency of 5 orders of magnitude. Because we were not sensitive enough to distinguish between the two effects, we maintained the Rages et al. (1991) particle size distribution and adjusted the number of scatterers by using a scaling factor f_{hze} to the column density.

Three program filters that overlay bands that are sensitive to CH_4 absorption, 1.70, 2.25, and 2.36 μm. We used the June 5, 1996 albedo for the 1.70 and 2.25 μm results. For 2.36 μm, an average of the June and October 1996 observations weighted by their signal to noise ratios was used. Although the 2.12 μm filter bandpass is not sensitive to CH_4, it is located at the H_2 $\nu = 1 \rightarrow 0$ S(1) transition, and as such becomes optically thick in the stratosphere. The results derived from the 2.12 μm, 2.25 μm, and 2.36 μm filters are internally consistent, but are slightly different than the 1.70 μm result, which sets an upper limit on the haze scaling factor of about 2. Given the uncertainties in CH_4 absorption coefficients at the low stratospheric temperatures, this disagreement is not surprising, and the value derived from the other filters is used because it is likely to be more internally consistent. The individual parameter spaces for the 2.25 and 2.36 μm filters are shown in Figures 3.6 and 3.7, and are combined with the 2.12 μm result, which is represented as a box, in Figure 3.8. The allowed values for the haze scaling factor (where all three solution spaces overlap) range from 15 to 25, with a best fit of 20, again using a signal to noise weighting scheme for the 3 filters. Our results are relatively insensitive to the stratospheric CH_4 mixing ratio.

3.4.2 CH_4 cloud

As seen in Figure 3.3, the 1.99 μm filter probes to the depth of the CH_4 cloud, but no further. It is possibly the most useful filter, as it is sensitive to the haze column density, the total extinction optical depth of the cloud, and its vertical location. For small values of the haze scaling factor, the cloud is the dominant source of extinction, but its importance decreases for the high scaling factor values determined from our stratospheric modeling. As the cloud moves higher, the necessary column density required to produce the observed albedo decreases, as seen in Fig. 9. Using the haze scaling factor of 20 the upper limit for the cloudtop is at 0.8 bar, but our best result comes from using the 1.1 bar quantity that is near the value of 1.2 bar derived from Voyager observations. Use of this bandpass again sets an upper limit on the amount of haze present. The last box in Figure 3.9 shows that a haze scaling factor of 40 yields an albedo higher than our observational upper

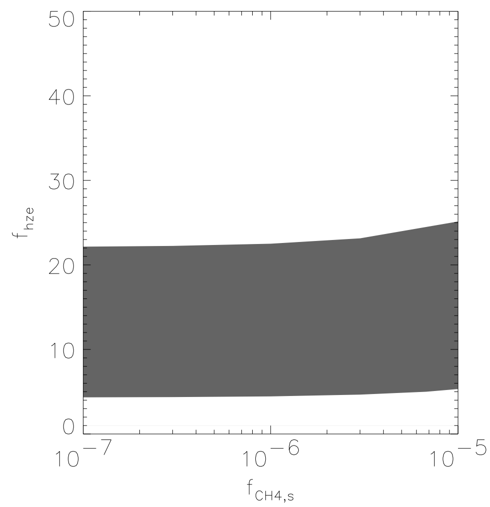

Figure 3.6: The solution space for the 2.25 μm results. The shaded regions represent the combination of parameters for the stratospheric CH_4 mixing ratio $f_{ch_4,s}$ and haze scaling factor f_{hze} that produce a geometric albedo within the model and photometric errors. Larger/smaller values of f_{hze} produce albedos larger/smaller than that measured

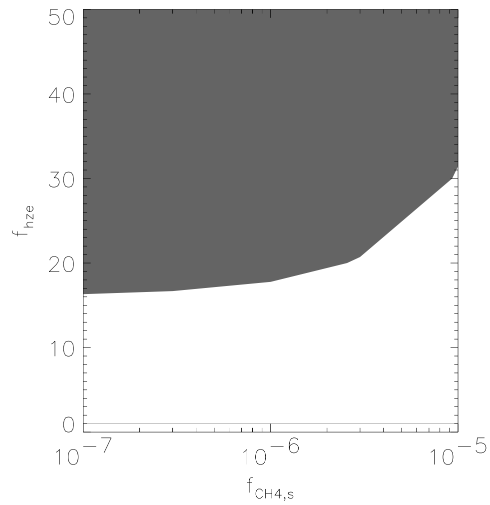

Figure 3.7: Similar to figure 6 for the 2.36 μm results.

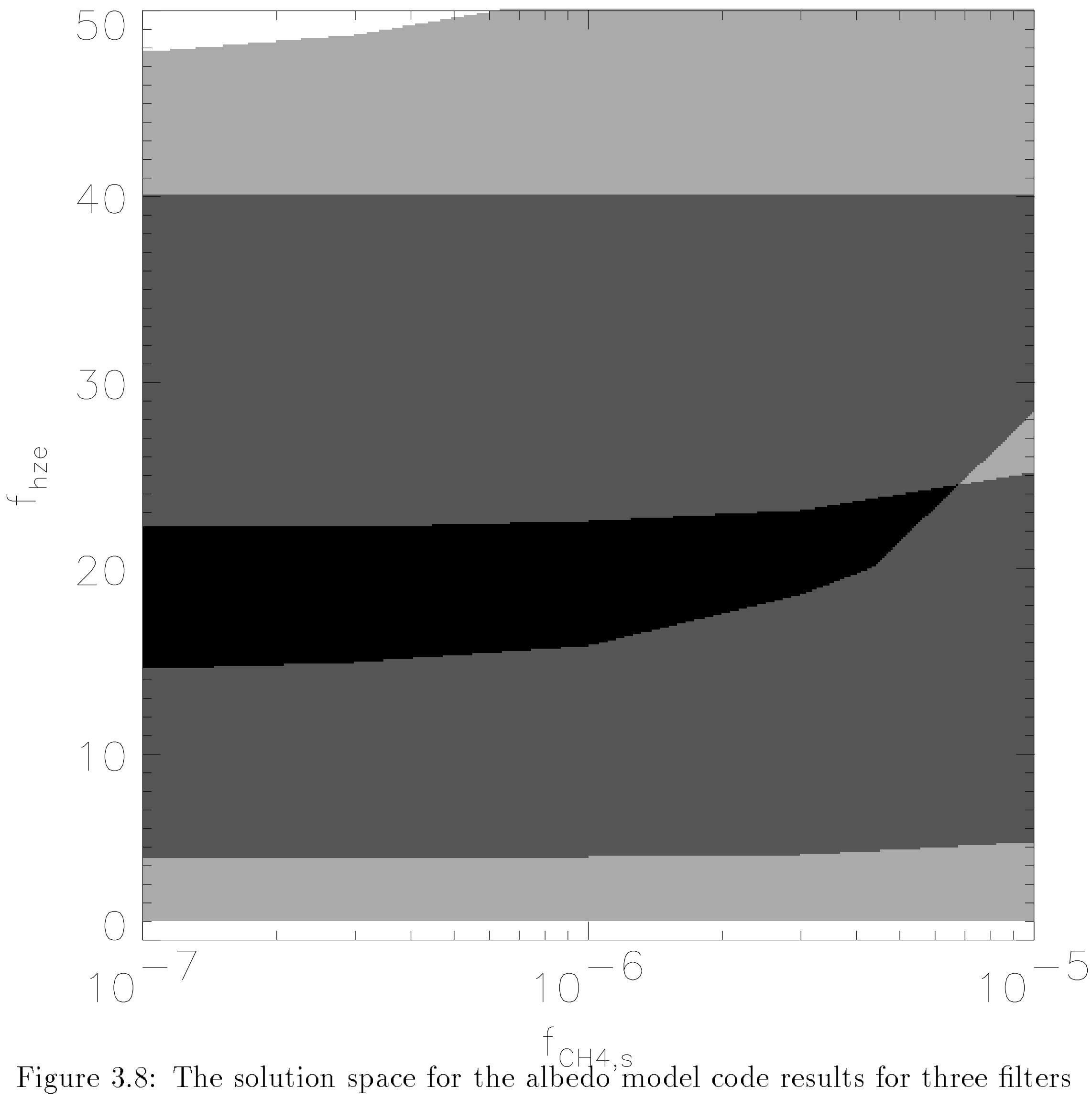

Figure 3.8: The solution space for the albedo model code results for three filters at 2.12, 2.25, and 2.36 μm as a function of the haze column density scaling factor f_{hze} and the stratospheric CH_4 mixing ratio $f_{ch_4,s}$. Darker shading represents the overlap of more allowed solutions, with the region bounding haze scaling factors of 15 and 25 representing an acceptable solution from the results of all three filters.

limit. For large values of f_{hze} the cloud optical depth is not a large contributor to the back-scattered light, explaining the lack of an asymmetry seen in the images.

3.4.3 Troposphere

The two "continuum" filters (those with almost no molecular absorption) at 1.28 and 1.58 μm are insensitive to the location of the CH_4 cloud, implying that the cloud is not optically thick at these wavelengths, and thus has a similar attenuation effect upon incoming radiation regardless of location. These bandpasses proved to be insensitive to the amount of haze, which typically contributed an optical depth on the order of 10^{-4} per baseline haze column density. The solution space of each bandpass is similar, as can be seen in Figure 3.10, where we compare the relation between the extinction of both clouds. At the nominal lower cloudtop location of 3.0 bars and any location lower in the atmosphere the relation is largely insensitive to the lower cloud, but as the cloudtop is moved to 2.0 bar (Figure 3.11) the sensitivity increases. Using the solution space created with a 3.0 bar lower cloudtop (Baines et al. 1995a) we see a linear relationship between the two cloud extinction opacities:

$$\tau_{cld2} = -6\tau_{cld} + 15 \tag{3.3}$$

If the optical depth in the 1-2 μm region can be established as being no more than 3 or 4, this would be a valuable tool towards determining the size of the cloud particles, which are indistinguishably optically thick in the visible (Baines and Bergstralh 1986, Pollack et al. 1986, Trafton 1987, Doose et al. 1988, Baines

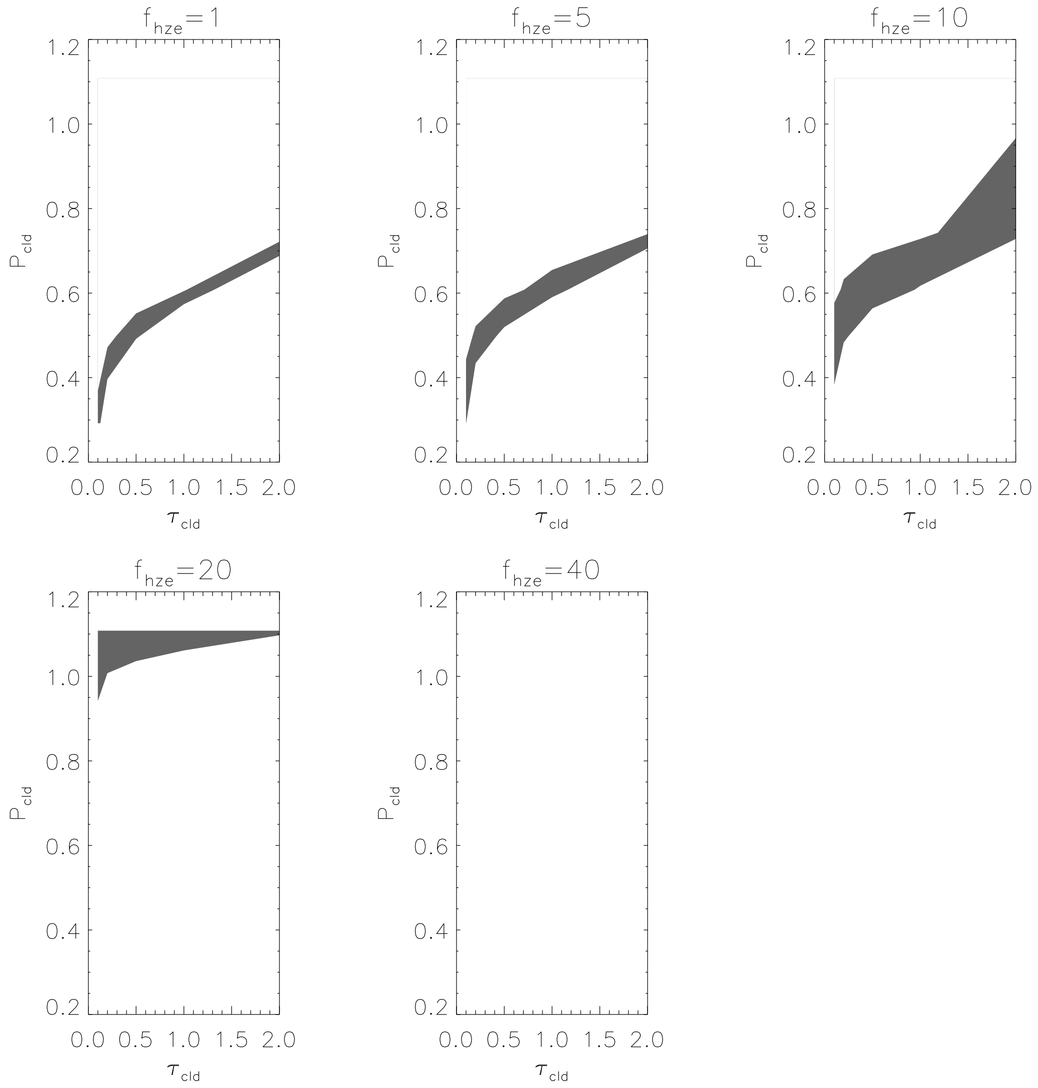

Figure 3.9: 1996 1.99 μm results from varying the methane cloudtop pressure P_{cld}, the haze column density scaling factor f_{hze}, and the cloud optical depth τ_{cld}. The cloud optical depth is relatively insensitive to low haze column densities or cloudtop pressure.

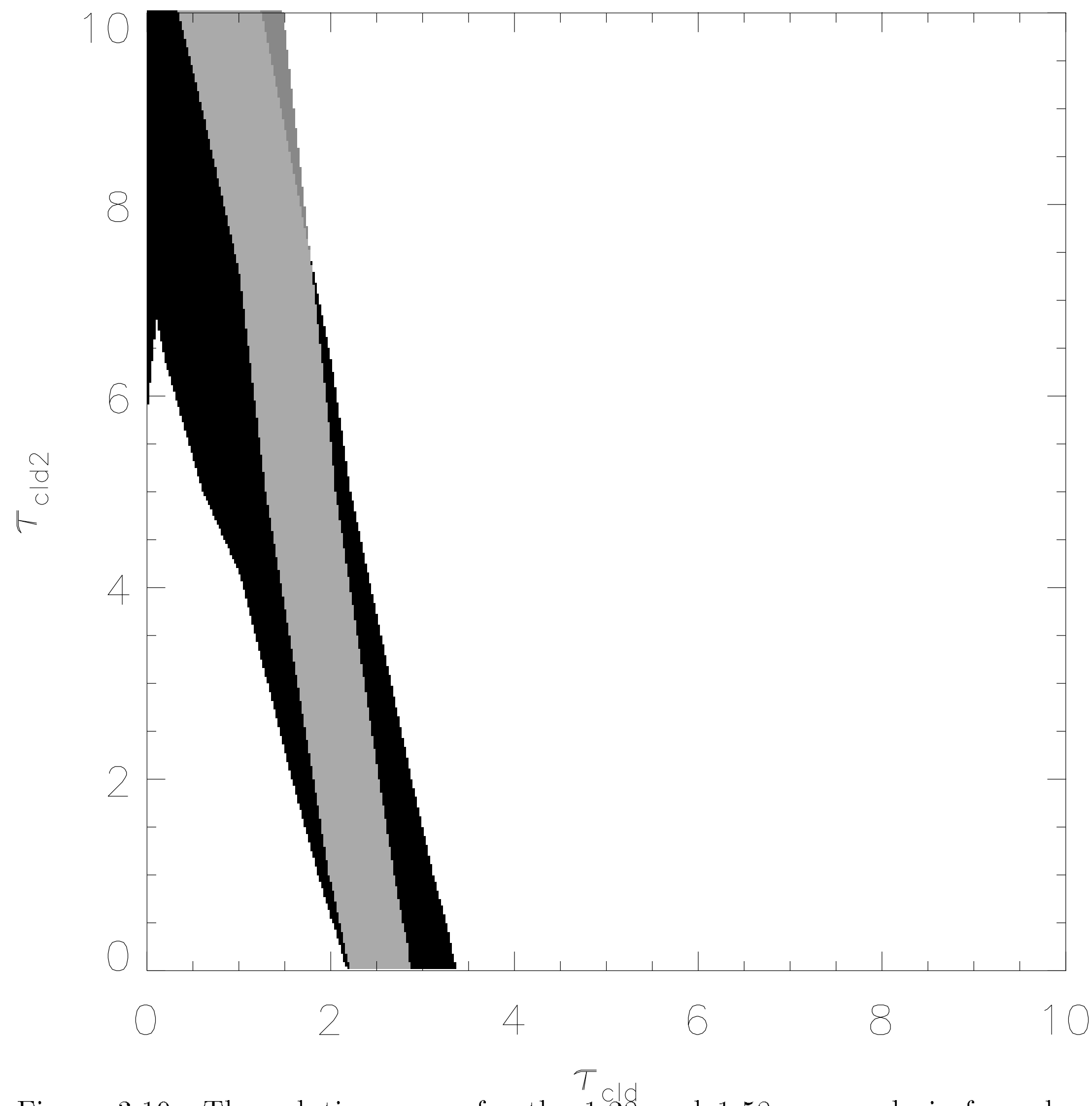

Figure 3.10: The solution space for the 1.28 and 1.58 μm analysis for a haze column density scaling factor f_{hze} of 20. The free parameters are the tropospheric cloud optical depths τ_{cld} and τ_{cld2}. Cloud locations are as shown in Figure 3.3. As in figure 8, the lighter region represents the overlap of allowed solutions for both filters, with the 1.28 μm optical thicknesses being scaled using Mie theory to match those at 1.58 μm. For our nominal model we choose τ_{cld} of 1.5 and τ_{cld2} of 6.0 as consistent with other results (Rages et al. 1991), however all solutions are equally valid.

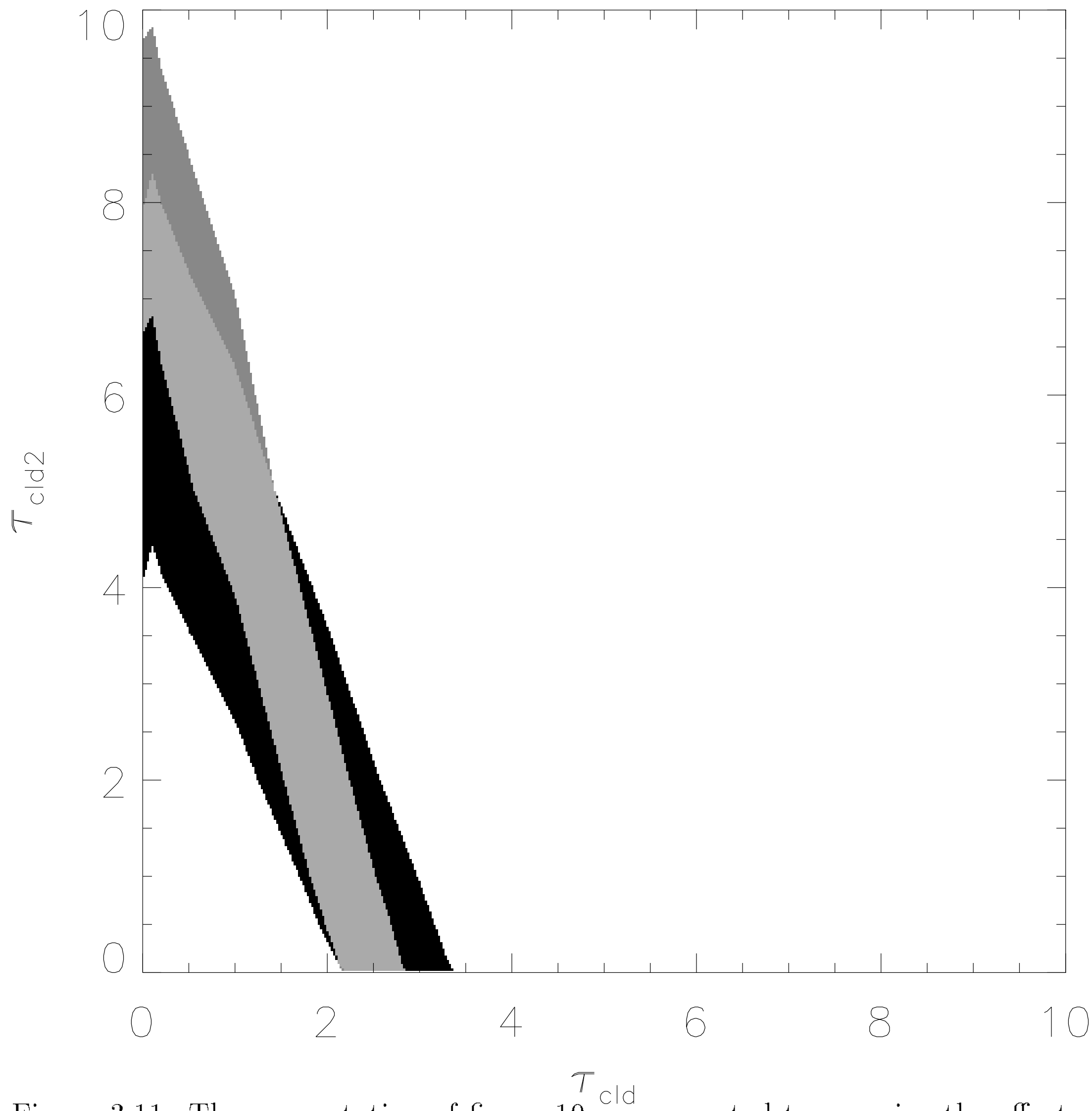

Figure 3.11: The computation of figure 10 was repeated to examine the effect of moving the lower cloud top to 2.0 bars. All results with a cloudtop lower than 3.0 bars closely resemble figure 10.

et al. 1995a, Rages et al. 1991).

3.4.4 Model comparison

In Table 3.7 we compare the parameters of our best atmosphere model with those of Rages et al. (1991) and Baines et al. (1995a). The geometric albedo spectra of our and the Baines et al. (1995a) models are shown in Figure 3.13. Labeled optical depths of the CH_4 cloud are at 1.58 μm for our model, and at 0.7 μm for the other two. The Baines model does not use the Rages haze structure, but a similar model, also derived from Voyager results by Pollack et al. (1987) with nearly the same column density of suspended particles. As seen in Figure 3.14, the extinction efficiency Q_{ext} for mean cloud particle sizes of 1 μm is greater at 1.58 μm than at 0.7 μm by approximately 20%, yielding an expected value for the total cloud optical depth of 1.6 at 1.58 μm when compared to the model of Rages et al. (1991), within the errors of both models.

Table 3.7: Model parameters

Model	n_i	f_{hze}	$f_{CH_{4},s}$	P_{cld}	τ_{cld}	τ_{cld2}	$\tilde{\omega}_{cld2}$
This work	5×10^{-3}	20	10^{-6}	1.1	1.3	6.0	0.99
Baines et al. (1995a)	0	$\approx$1	10^{-6}	1.2	0.4	10	0.90
Rages et al. (1991)	$\sim 10^{-7}$	1	N/A	1.2	1.5	∞	0.65

3.5 Discussion

We have observationally examined the properties of scatterers in the Uranian atmosphere beyond 1 μm. Our results confirm the likely seasonal nature of the

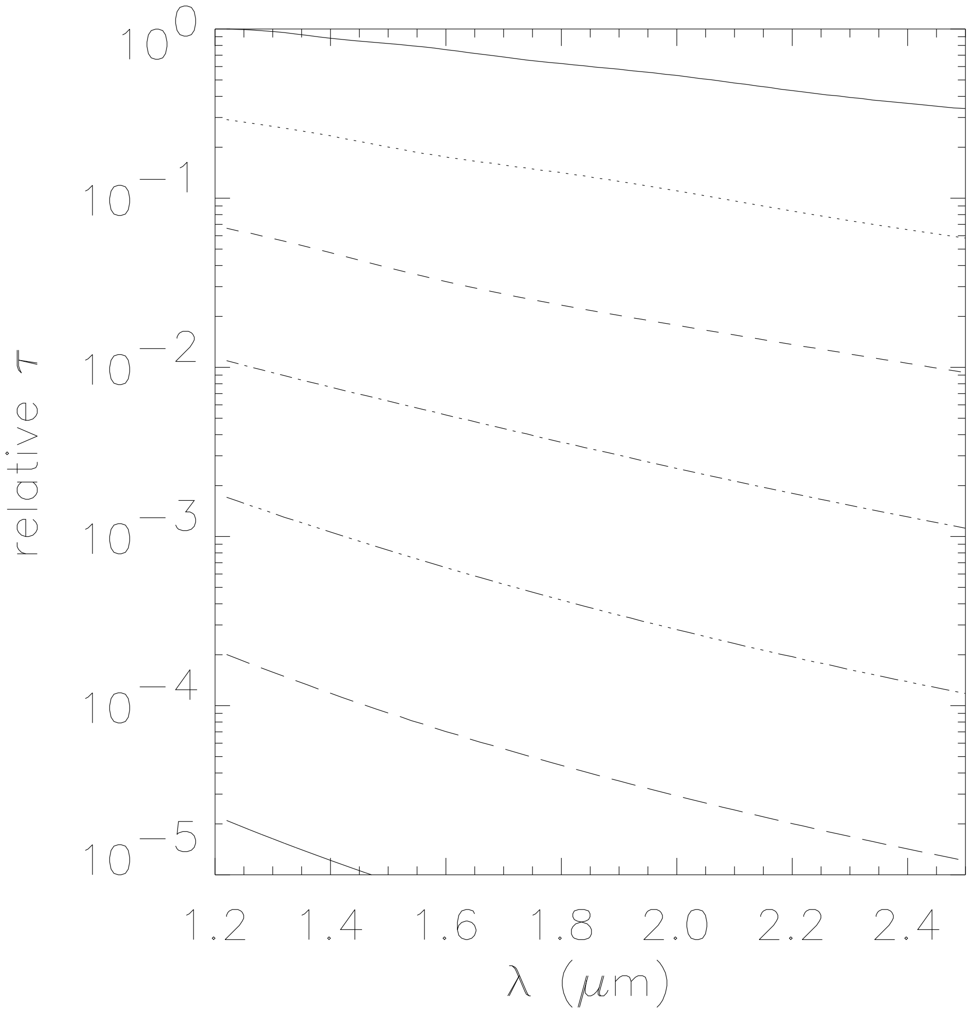

Figure 3.12: The total extinction optical depth of atmospheric aerosols as a function of particle size and wavelength as computed from Mie theory using spherical particles. From the top, lines represent the results of log r = 0.00, -0.17, -0,33, -0.50, -0.67, -0.83, and -1.00 where r is the particle radius measured in microns. The results are scaled to give a value of 1.0 for a 1 μm particle at 1.2 μm.

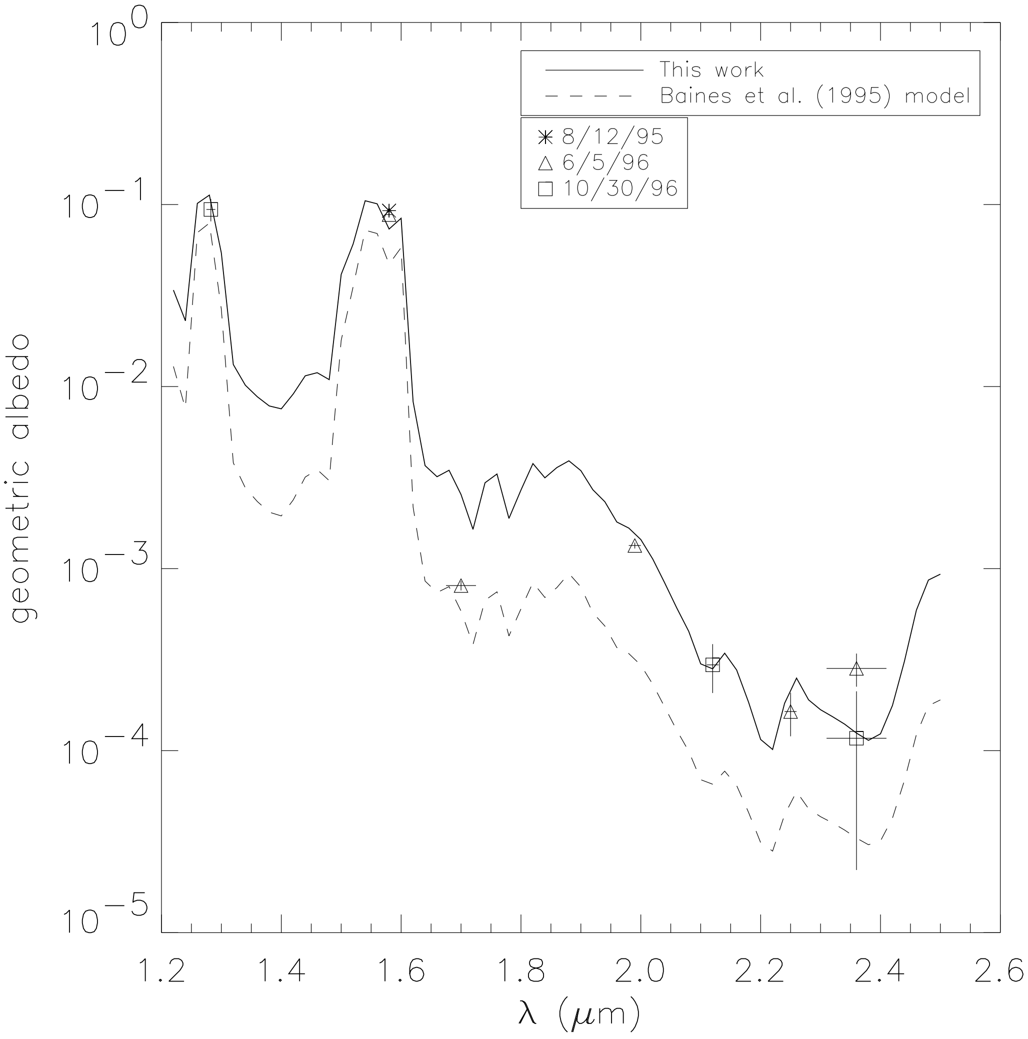

Figure 3.13: The computed geometric albedos (taken every 0.02 μm) of three models of the Uranian atmosphere in comparison with data taken on August 12, 1995, June 5, 1996, and October 30, 1996. Vertical error bars represent the photometric errors, and horizontal error bars (often smaller than the symbol) delimit the filter bandpasses. The nominal model employs the parameters described in Table 3.7 as fit to the 1996 dataset. The Baines et al. (1995a) model, derived from CH_4 and H_2 from 0.7 μm is shown to be darker than observed when extrapolated into the near-IR.

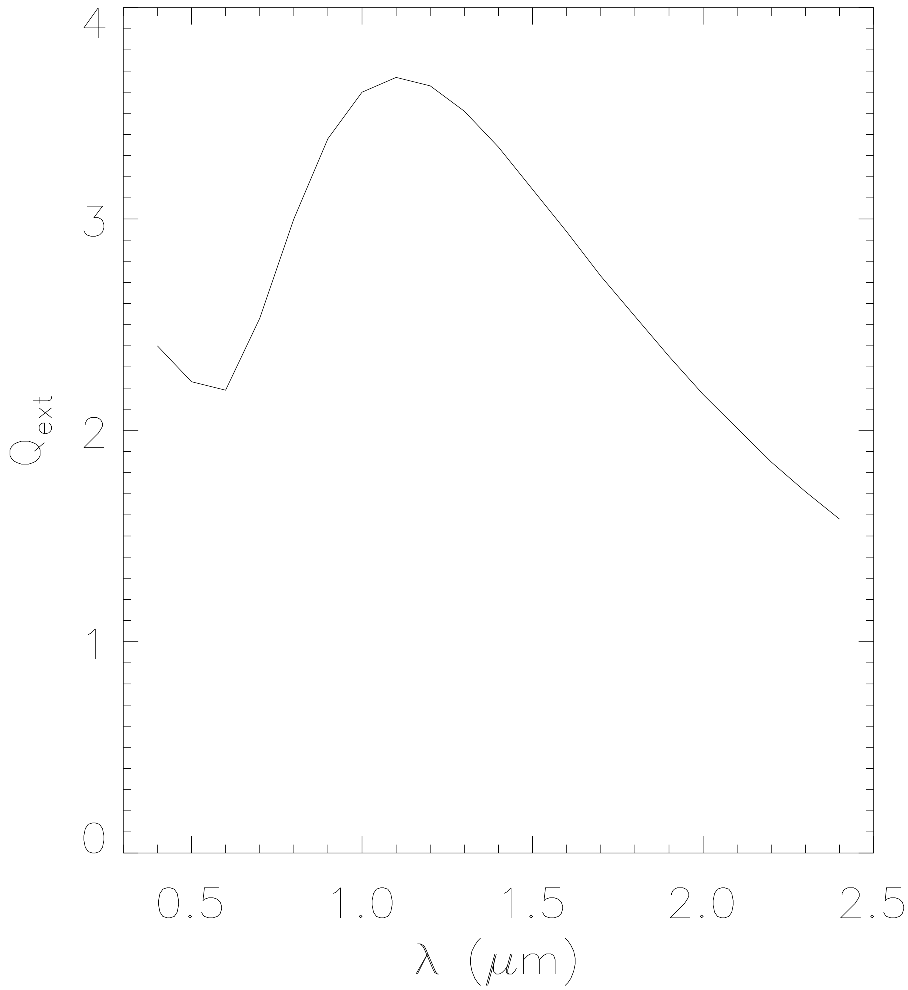

Figure 3.14: Scattering efficiency Q_{ext} over the solar spectrum as computed using Mie theory with 1 μm spherical particles. The results located at the comparison wavelengths for the optical and near-IR studies, 0.7 μm and 1.58 μm are similar.

albedo, as explored by Lockwood et al. (1983) and Hammel (1996). When Voyager encountered Uranus the planet was at summer solstice, and the planet exhibited similar temperature profiles at both polar regions (Hanel et al. 1986). Ten years later, the southern hemisphere has experienced nearly twenty years of constant insolation, which could lead to an increase in the polar haze formation rate. We show that the disk-averaged column density of haze particles above the tropospheric CH_4 cloud has indeed risen by a factor of 15 to 25 with a best fit of 20 for the solar-facing hemisphere in the intervening time. This interpretation of the increased scattering is not unique, and could also be related to an increase in the mean modal radius of the particles. However larger particles would fall more rapidly, leading to a decrease in the column density. Thus a number density change is the more likely explanation.

There is no evidence for significant haze absorption at near-IR wavelengths, rather the haze particles scatter almost conservatively. This is not unexpected, as very few candidate molecules absorb between 0.5 and 3 μm. We are not highly sensitive to the stratospheric CH_4 abundance, and show allowable mixing ratios only restricted by the upper limits of Orton et al. (1987) of 1×10^{-5}.

If there has indeed been a twentyfold increase in the haze column number density in Uranus' atmosphere, the increased absorption will warm the stratosphere. Marley et al. (1997) found that while the haze described by Rages et al. (1991) did not play a substantial role in heating the stratosphere, haze abundances an order of magnitude larger could heat the 10 to 100 mbar region by over 10 K. Thus new mid-infrared observations of Uranus should show a warmer stratosphere than that seen in the Voyage epoch. Such observations would test the hypothesis that hazes play a significant role in the stratospheric energy balance (Appleby 1986).

In the troposphere, the CH_4 cloud has remained in the same location as in the Voyager epoch. If the mean particle sizes have remained constant near 1 μm then it is likely that the column density of the cloud has remained the same as well. Properties of the lower tropospheric cloud are much more difficult to isolate, as they are dependent on our understanding of the upper cloud. If the lower cloudtop has indeed risen above the 3.0 bar predicted by other works, then the cloud is less likely to be optically thick in the near-IR.

Chapter 4

A SPATIALLY-RESOLVED MODEL OF URANUS IN 1995

4.1 Introduction

The Voyager 2 encounter in 1986 provided multi-wavelength and viewing angle observations that form the foundation for our knowledge of scatterers in the Uranian atmosphere (see Smith et al. 1986, Lindal et al. 1987, Rages et al. 1991, West et al. 1991, and Pryor et al. 1997). These works first quantified the amount and size distribution of hazes in the stratosphere and upper troposphere as well as the CH_4 cloud. In the ten years since that encounter the planet has continued to move from summer solstice to equinox for the facing southern hemisphere, which may cause a change in the recently observed southern polar cap (Zellner et al. 1994, Baines et al. 1995b, and Walter and Marley 1997) as it gradually receives less insolation. Continuous monitoring of the planet is important because of the extreme orbital inclination that makes its seasons more severe than the other Jovian planets.

Followup observations have begun in earnest in the past few years. Walter and Marley (1997) used near-infrared observations to show that in the ensuing interval the column density of haze particles increased significantly, by a factor of 20 in 1996. This and other recent observational works (Karkoschka 1994, Baines et al. 1995a) have been disk-averaged due to the low surface brightness and small angular size. The Hubble Space Telescope (HST) allows significant improvement in the study of planetary inhomogeneities.

In this study we use high-resolution data to extend the results of Walter and Marley (1997) to spatially-resolved observations of the planet. In addition we extend the time range addressed by them by using observations taken a year earlier. Section 2 addresses the observations and photometric reduction methods, while in section 3 the modeling is detailed. In section 4 we present our results and discuss their implications in section 5.

4.2 Observations

The data used in this work was acquired with two telescopes. All images taken shortwards of 1 μm ("visible") were obtained by HST on July 3, 1995 UT using WFPC2 in both the Wide Field and Planetary Camera configurations and acquired from the HST archive. The data were acquired under an observing program directed by Martin Tomasko and Erich Karkoschka. The remainder of the data ("infrared") were obtained by Heidi Hammel using NSFCAM, a 1–5.5 μm

Table 4.1: Filters and integration times

Filter name	Central wavelength (μm)	FWHM (μm)	Integration time(s)
F467M	0.4682	0.0371	8
FQCH4N-B	0.6193	0.0044	160
F673N	0.6733	0.0047	100
FQCH4N-C	0.7274	0.0051	160
J	1.26	0.31	8
H	1.62	0.28	14
K	2.21	0.39	120

camera at the IRTF on Mauna Kea, HI on August 27, 1995 UT. Table 4.1 gives the effective center, full width at half maximum (FWHM), and integration time for all filters used. The standard pipeline calibration was used for the HST data (Holtzman et al. 1995a, 1995b), while the IRTF data was calibrated using the UKIRT faint standard star FS-34 (Casali and Hawarden 1992). The planet can be seen in broadband H and K filters in Figure 4.1. Images taken in J look similar to those in H.

Each image was mapped (accuracy was better than one pixel) to determine the viewing parameters μ, μ_0, and dφ for each point on the planet. These are the scattering and incident angles measured from the zenith and the change of azimuthal angle of the outgoing ray. The zenith angles at a point can be determined from the latitude and longitude of the point and the sub-solar and sub-Earth points. From these and the scattering angle, the azimuthal angle dφ is determined for each point. The mapping procedure was modified from the algorithms of the program AMIE (Hockey and Barnet 1994), a representation of the JPL VICAR

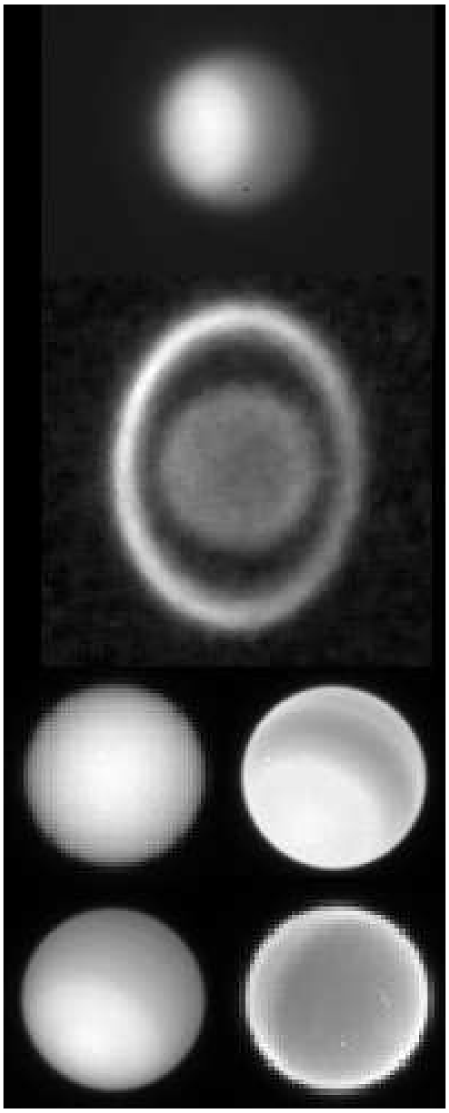

Figure 4.1: Images used in the study. At top and second from top are data in broadband H and K taken at the IRTF on August 30, 1997, while on the bottom are clockwise from top left 4682, 6193, 7274, and 6733 Å. The H image shows a distinct asymmetry in the CH_4 cloud layer centered about the south pole. The K filter overlies deep CH_4 and H_2 absorption, making the planet appear as dark as the ring system. Both the 6193 and 6733 Å images show clearly the cloud asymmetry, while the 7274 Å image is severely limb-brightened and the 4682 is a uniform Rayleigh-scattering disk.

suite of programs (Jepsen et al. 1980) in IDL. For purposes of consistency with other works the IAU-recommended polar and equatorial radii were used (Davies et al. 1995). Sub-solar and sub-Earth points were acquired from the JPL Horizons on-line ephemeris (Chamberlin et al. 1996).

The photometric calibration was then completed by converting the DN values to the absolute reflectivity I/F, which is the albedo for a point on the planet, in this case the width of a pixel (between 300-700 km for our data), and is highly dependent upon the viewing geometry and position from the planetary limb. The solar spectrum was modeled in the infrared using the spectra of Labs and Neckel (1968) and in the visible by Neckel and Labs (1984), linearly interpolating between their points to the effective center of each filter. This was merely the published center in the small bandwidth visible filters, but was determined by integrating over bandpass in the broadband K filter.

Two latitude bands were selected for study, -22.5° and -65° latitude. The reasons for this were twofold. First, these were the bands analyzed by Rages et al. (1991) in their analysis of Voyager data. Second, these lay completely outside and inside respectively of a marked cloud asymmetry discussed in a later section (and seen in Figure 4.1). All points located at the given latitude or no more than 1 FWHM away were studied to allow for image smearing. The infrared data highly oversampled the FWHM (typically 0.3–0.4″), so it was necessary to first use a median filter with a box the size of the FWHM before selecting points to

Table 4.2: Points used

λ (μm)	Points at -22.5°	Points at -65°
0.4682	29	28
0.6193	189	170
0.6733	203	186
0.7274	49	38
2.21	717	646

study. Because of the increased uncertainties of mapping points near the limb, all points with $\mu < 0.22$ (where the errors in the plane parallel approximation are greater than 1%) were not included in the modeling. It is probable that some photons from the limb were still picked up in the extreme pixels used for analysis. The total number of points used in the modeling is then given in Table 4.2. This number is significantly less for the 4682 and 7274 Å images, which were taken in the WF4 chip, unlike the rest in PC1. In addition all data was taken with a phase angle less than 1.8°, so geometric albedos were computed in all filters. The geometric albedo represents the disk-averaged reflectivity of the planet at 0° phase angle, however we computed our albedo models at the same phase angle as the observations.

Photometric errors in the resultant images were 25% in the K filter, and 5% in the HST images, dominating the uncertainties in the solar fluxes and standards.

4.3 Model

The I/F was modeled at each point using an adding-doubling code developed from scratch and based on the principles described in Hansen and Travis (1974). Each bandpass was treated using a finite number of layers, typically 7-10, for which an extinction optical depth, phase function, and single-scattering albedo was specified, and results were integrated over the known transmission curves for each filter. Extinction from six sources was included, Rayleigh scattering, hydrocarbon hazes, a CH_4 cloud, a lower optically thick cloud, CH_4 absorption, and collisionally-induced H_2 absorption. The code was tested by comparison to the work of Dlugach and Yanovitskij (1974).

In addition to the particle scattering described below, extinction due to Rayleigh scattering and molecular gas absorption was modeled in each layer. Rayleigh scattering at all wavelengths and molecular absorption by CH_4 and H_2 in the infrared was treated as in Walter and Marley (1997). In the visible, the low temperature CH_4 absorption coefficients of Karkoschka (1994) were used. H_2 absorption was neglected in this regime because the filters did not overlap relevant portions of the H_2 spectrum. In the stratosphere we used the same CH_4 mixing ratio, 10^{-6}, and follow the saturation curve in the troposphere above the CH_4 cloud as in Walter and Marley (1997). Mean filter-averaged values of the CH_4 absorption coefficient for each visible filter are given in Table 4.3. For this analysis the optical filters as well as broadband K are used. The other infrared filters are excluded because

Table 4.3: Mean CH_4 absorption coefficients (Karkoschka 1997)

λ (μm)	α_{CH_4} (km-am)$^{-1}$
0.4682	0.001
0.6193	0.59
0.6733	0.047
0.7274	3.5

they span several orders of magnitude in CH_4 and H_2 absorption and are thus not as sensitive.

Our goal with the analysis was to determine f_{hze}, a multiplicative scaling factor to the Voyager 2 haze column density (Rages et al. 1991), and τ_{cld}, the optical thickness of the CH_4 cloud. There are other scattering parameters that can be fit for, but these values are well-established in the literature in most cases and are likely to be more stable than the column density of scatterers, which is thought to be seasonally-dependent.

4.3.1 Haze layers

Depending upon the necessary resolution required either 4 or 8 haze layers were used. 8 layers were necessary in the darker bandpasses where the majority of extinction took place above the CH_4 cloud. The haze was treated using the model of Rages et al. (1991) as described in Walter and Marley (1997) to obtain a baseline optical depth, single-scattering albedo, and asymmetry parameter. We used a single Henyey-Greenstein phase function for each layer with an asymmetry parameter determined by Mie scattering.

4.3.2 CH_4 cloud layer

The optical depth of the CH_4 cloud was treated as a free parameter, but the literature was used to define the phase function and single-scattering albedo $\tilde{\omega}_{cld}$ in the visible. At 4682 Å we used a $\tilde{\omega}_{cld}$ of 0.989 (Baines et al. 1988), while characteristics of the similar cloud in Neptune are used to derive less certain values of 0.90 at 6193 Å and 0.80 at 7274 Å (Baines and Hammel 1994). At 6733 Å we used a value of 0.985, derived from approximations to Mie scattering theory given in the Appendix of Rages et al. (1991). In the deeper CH_4 band (K) the cloud is not detected and cannot be characterized. For all filters with a cloud visible (spanning 4682-7274 Å) the phase function was a double Henyey-Greenstein function, with parameter g_1=0.75, g_2=-0.18, and f=0.56 (Rages et al. 1991).

4.3.3 Clear layer

Between the two tropospheric clouds exists a clear layer, which was modeled simply as an absorbing, Rayleigh scattering region.

4.3.4 Lower cloud layer

The lower optically thick cloud (thought to consist of condensed H_2S) is more problematic to describe (de Pater et al. 1989). We used the same phase function as the CH_4 cloud. At 4682 Å the single-scattering albedo $\tilde{\omega}_{cld2}$ is 0.9985 (Wallace

1980) and at 6733 Å we used information on the similar cloud in Neptune to derive a value of 0.90 (Baines and Hammel 1994).

4.3.5 Computational methods

For each layer the phase function was computed from a weighting of the individual phase functions by total scattering optical depth. An 11×11 matrix of Gauss points was used to determine the resultant reflection matrix for each monochromatic point in the filter bandpass (separated by 1 nm in the visible and 10 nm in the infrared), and then determined for each point by cubic interpolation. These values were then integrated over the bandpasses to arrive at the final reflectivity.

Polarization effects make it necessary to use the complete 4×4 scattering matrix to treat the problem of Rayleigh scattering. Since this is computationally intensive, it is possible to use results derived with a simple 1 term single-scattering phase function in the computations and account for the errors introduced in the approximation, in all cases less than the error in the flux computation (10%) from layer to layer. Using the single term typically results in reflectivities too small, an average of 4% (Rages et al.). This problem is worse for shorter wavelengths. To account for this, all model I/F's for the 4682 Å filter were increased by 5%, and the other visible filters by 2%.

To determine the best fitting models, I/F's for each filter were computed for varying values of the free parameters f_{hze} and τ_{cld}. The quality of fit of each model was judged by a χ^2 computation. The results were then compared (next section) to confidence levels of 68, 95, and 99%, approximating 1, 2, and 3 σ fits. The final best-fitting model was arrived at by weighting each filter by its signal to noise (typically 8 in the optical and 2 in K-band when uncertainties in the gas absorption coefficients are included).

4.4 Results

The filter set of this study provides the opportunity for sensitive study of several levels of the atmosphere. Figure 4.2 illustrates the extinction level of each filter at normal incidence. The location in the atmosphere where optical depths, 1, 3, and 9 are reached is shown to illustrate the effective depth reach in the atmosphere at each wavelength. This plot does not distinguish between the differences between gas (Rayleigh) and haze (Mie) scattering, nor gaseous molecular absorption by CH_4. Overlain is the full-disk spectra of Uranus in 1993 (Karkoschka 1994).

The broadband K filter (not shown) overlays deep CH_4 and H_2 absorption bands, ensuring effective probing of the stratospheric hazes, below which few photons penetrate. The hazes are also well-sounded by the 7274 Å filter, which becomes optically thick just above the CH_4 cloud, and by the 4682 Å filter, where the hazes are much more forward-scattering than the Rayleigh phase function. The CH_4 cloud is best revealed by the weak CH_4 filter at 6193 and the continuum filter (extremely weak CH_4 absorption – see Table 4.3) at 6733 Å, which has a gas absorption optical depth of ≈ 0.7 in the cloud and clear layers. In Figure 4.3 the best-fit model (see Table 4.4) derived using all the filters is compared to the

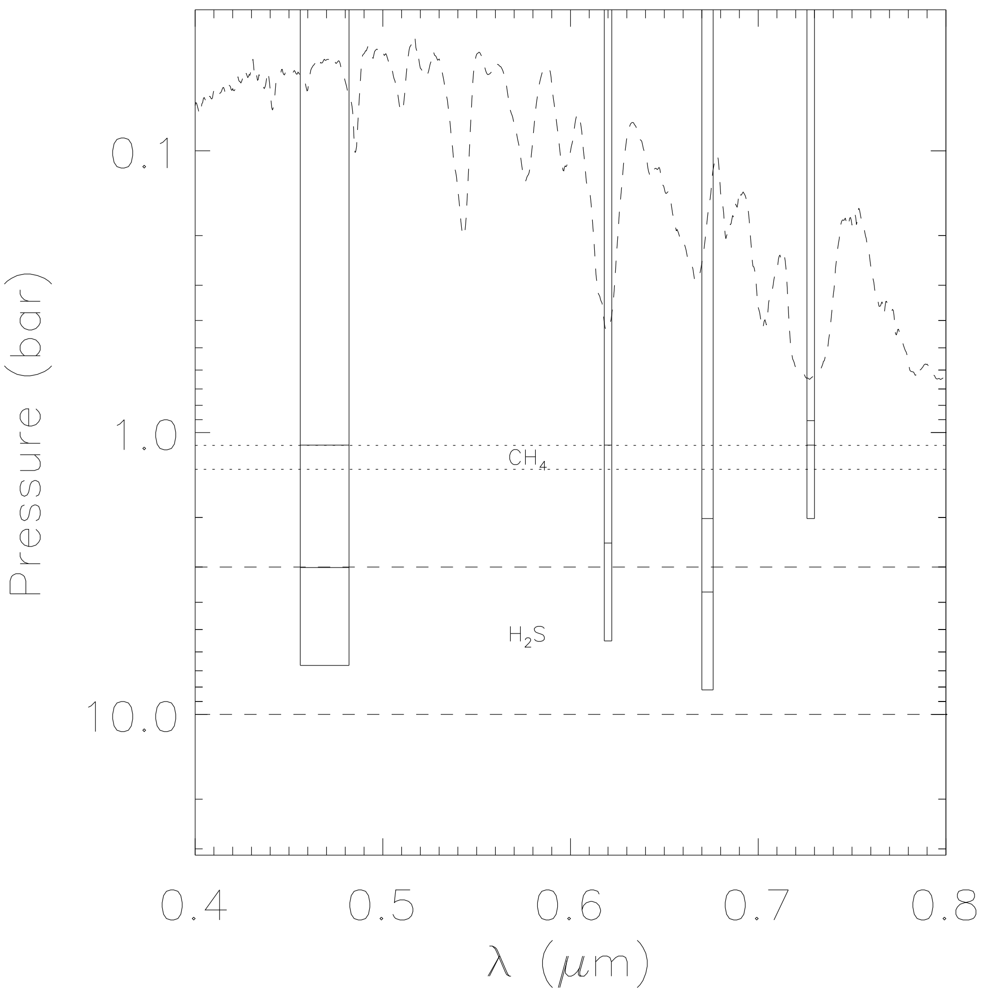

Figure 4.2: Extinction levels for the visible filters used in the study. Horizontal width represents the FWHM of the filter. Vertical length represents levels at which optical depth from all sources reaches 1, 3, and 9. No distinction is made between extinction due to scattering and absorption. Overlain linearly in both axes is the albedo spectra of Karkoschka (1994) in dashes. Also shown is the location in our model of the CH_4 and H_2S tropospheric clouds.

Table 4.4: Best model

	-22.5°	-65°
f_{hze}	8 ± 3	5 ± 2
τ_{cld}	0.2 ± 0.1	1.2 ± 0.4

scans at each filter.

4.4.1 Latitudinal scans

Hydrocarbon haze

Figures 4.4 and 4.5 show respectively the allowed solution spaces for the 4682 and 7274 Å filters at both latitudes. We varied both free parameters, the haze scaling factor f_{hze} and τ_{cld}, for these filters, however the results are very weakly sensitive to the cloud. In the 4682 Å bandpass the opacity is dominated by Rayleigh scattering and the lower cloud, while in the 7274 Å bandpass, gaseous CH_4 absorption causes the cloud to go optically thick just above the CH_4 cloud. These results when combined with those from the K filter (computed without the undetectable CH_4 cloud) yield scaling factors f_{hze} of 8 ± 3 at -22.5° and 5 ± 2 at -65°.

Methane cloud

At the time of Voyager the CH_4 cloud had very different depths at the two latitudes in question, with an optical depth of 0.66 ± 0.18 at -22.5° and 2.4 ± 0.3 at -65° latitude (Rages et al. 1991). Figures 4.6 and 4.7 display the allowed solution space for both latitudes for the weak methane 6193 Å and continuum 6733

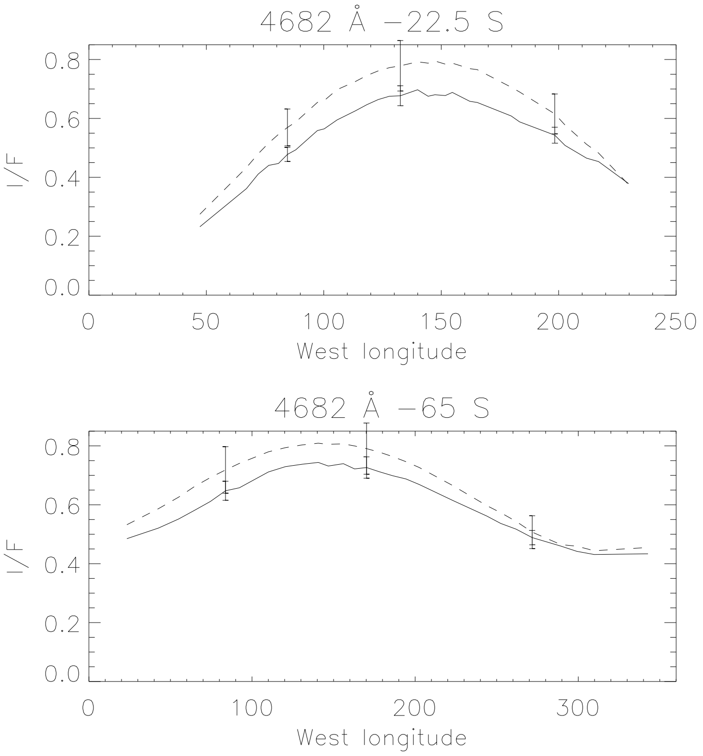

Figure 4.3: The results of the best-fit model (dashed line) are compared to the observations for each filter (solid line) at (a)-22.5° and (b)-65°. Shown are 1-σ errors of model (11%) and data (5%). Longitudes are System III.

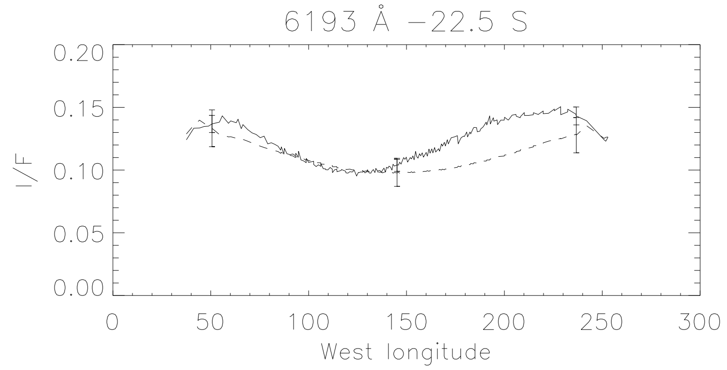
6193 Å −22.5 S
I/F
0.20
0.15
0.10
0.05
0.00
0 50 100 150 200 250 300
West longitude

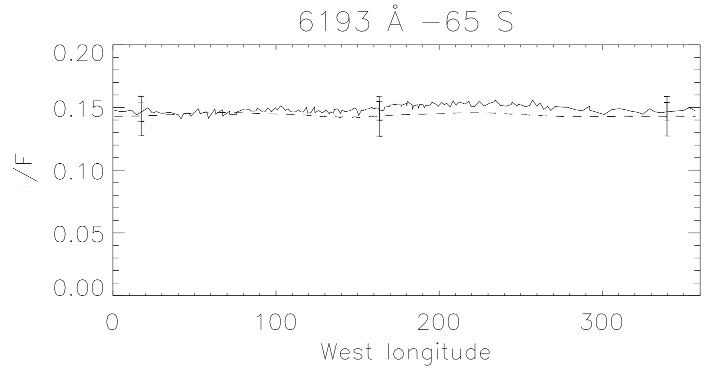
6193 Å −65 S
I/F
0.20
0.15
0.10
0.05
0.00
0 100 200 300
West longitude

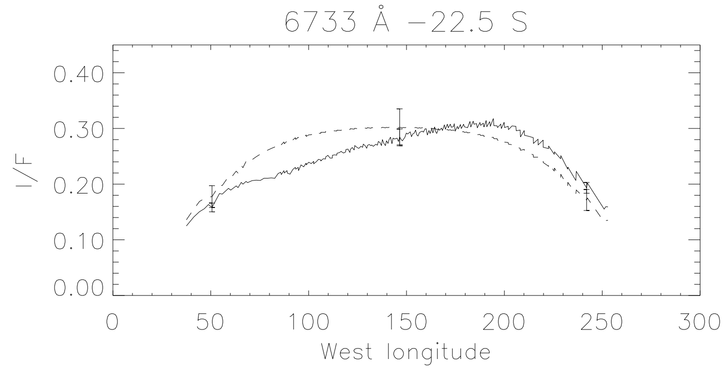
6733 Å −22.5 S
I/F
0.40
0.30
0.20
0.10
0.00
0 50 100 150 200 250 300
West longitude

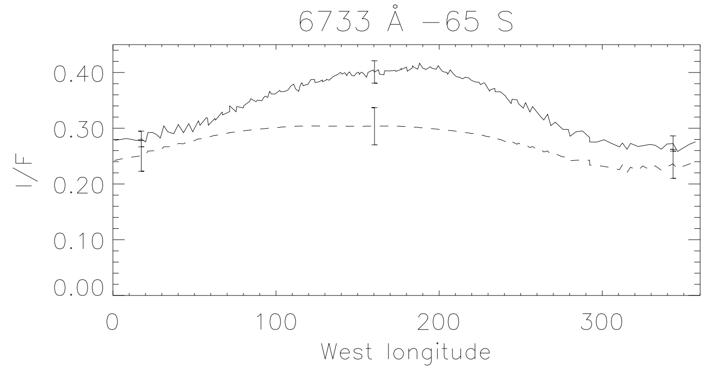
6733 Å −65 S
I/F
0.40
0.30
0.20
0.10
0.00
0 100 200 300
West longitude

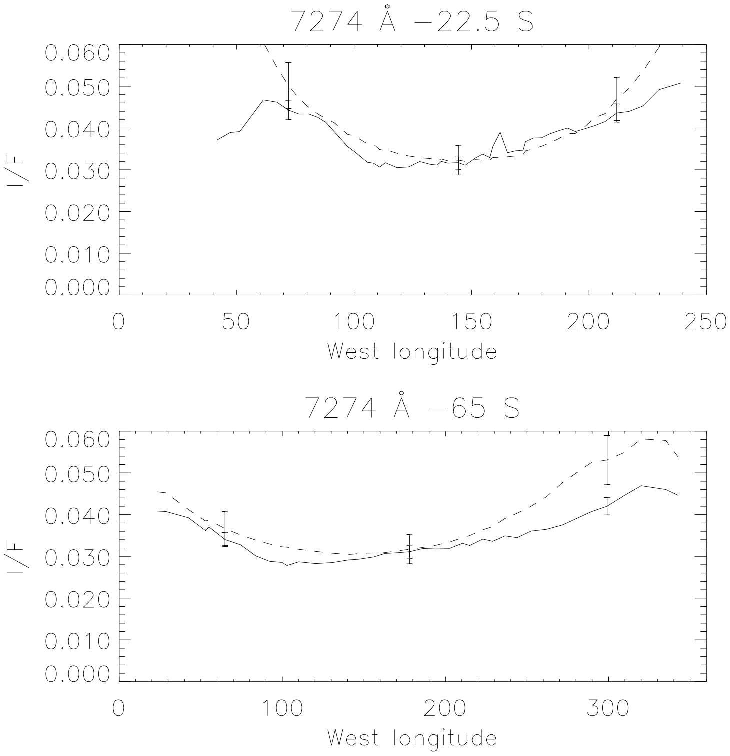

Å filters, showing that the inhomogeneity has remained the same, although the optical depth of the cloud has decreased at both latitudes, to values of 0.2 ± 0.1 at -22.5° and 1.2 ± 0.4 at -65°. Assuming these to be typical values of the interior and exterior of the cap, and that the cap extended from the south pole to approximately -40° this gives a disk-averaged optical depth of 0.6 for the Earth-facing hemisphere. The increased heating as the planet approaches equinox should lead to decreases in the cloud thickness.

Tropospheric methane mixing ratio

The value for the tropospheric CH_4 mixing ratio was determined for the best fit Voyager RSS model to be 2.3% (Lindal et al. 1987). A later analysis of weak

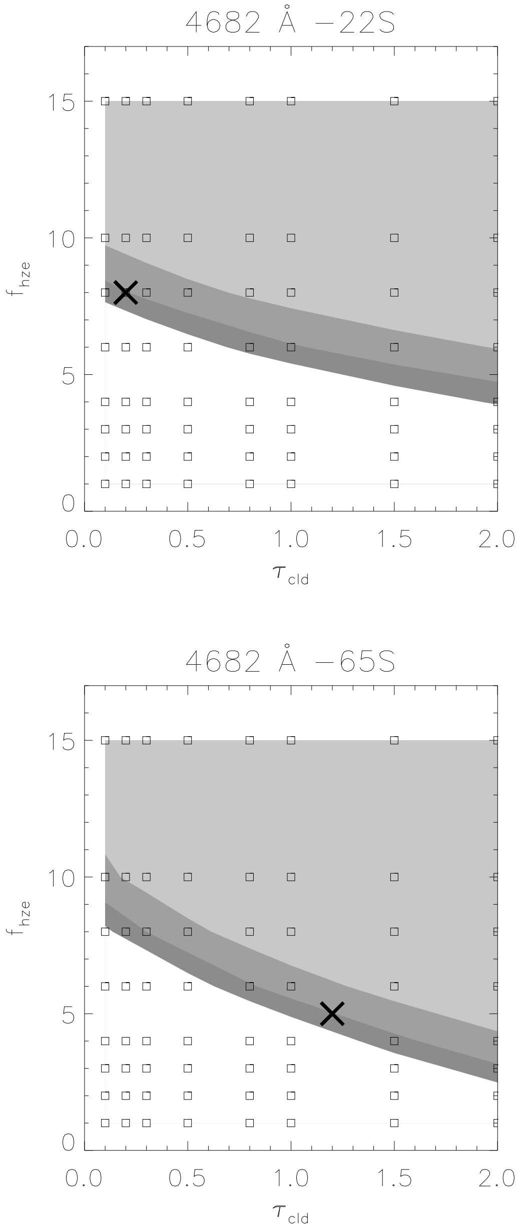

Figure 4.4: The solution space for the 4682 Å filter at (a)-22.5° and (b)-65°, computed for various values of the haze scaling factor f_{hze} and CH_4 cloud optical depth τ_{cld}. Individual points at which χ^2 fits were computed are indicated by squares. These results were then contoured to give the allowable solutions, with the lightest shade representing all 1-σ solutions, and darker shades representing 2-σ and 3-σ solutions. Those regions of parameter space in excess of 3-σ are left unshaded. This filter is much more sensitive to the column density of hazes than to the cloud density. The best fit model for the entire dataset at each latitude is shown by a cross.

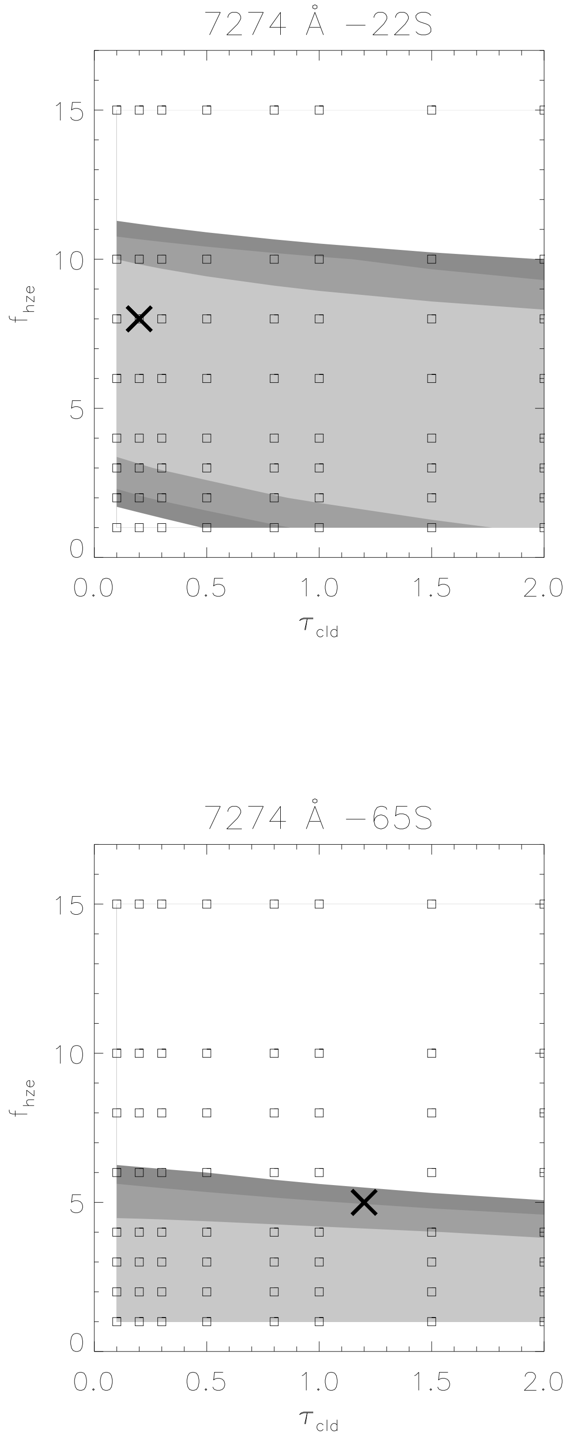

Figure 4.5: Identical to Figure 4.4 for the 7274 Å filter.

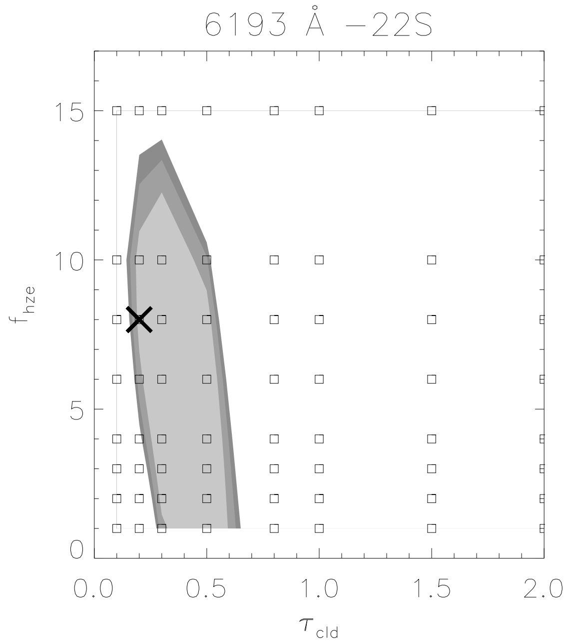

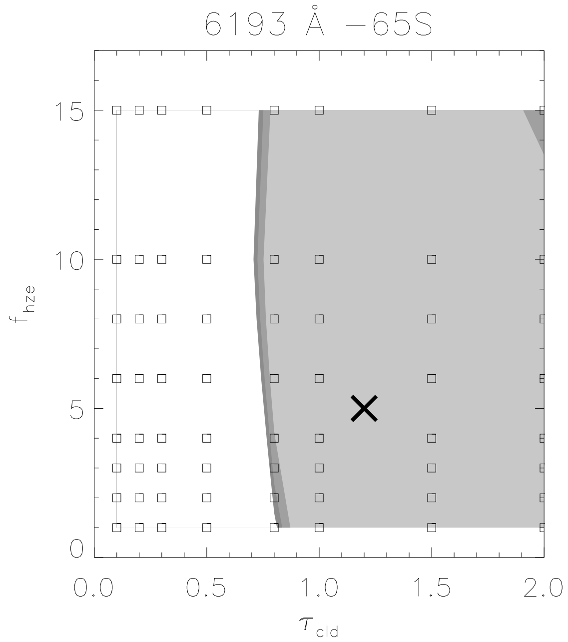

Figure 4.6: Identical to Figure 4.4 for the 6193 Å filter. At both latitudes the cloud optical depth is the driving force in determining a valid solution. At -65° the planetary inhomogeneity shows itself in a much more optically thick cloud than at -22.5°.

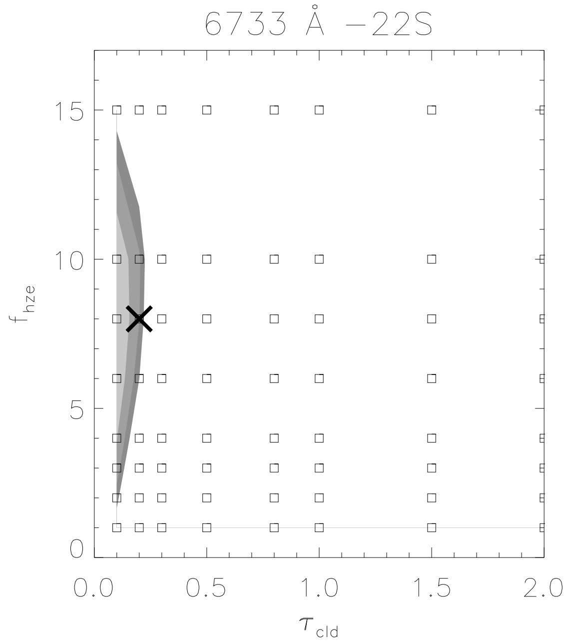

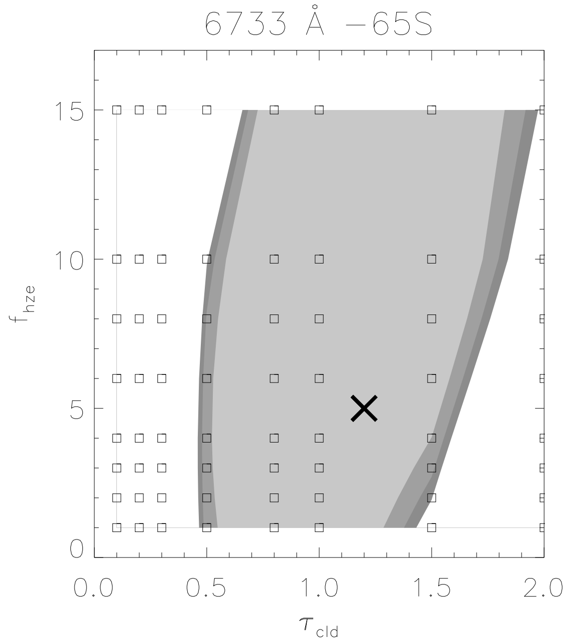

Figure 4.7: Identical to Figure 4.4 for the 6733 Å filter. Like Figure 4.6, the cloud asymmetry is a more important factor than the haze column density.

methane lines by Baines et al. (1995a) arrived at a value of $1.6^{+0.7}_{-0.5}$%. In Figure 4.8 a monochromatic run of the code compares the allowed values given at 6193 Å for both values at -22.5°. The result of using the higher mixing ratio requires an increased cloud optical depth of 0.1, unresolvable at our sensitivity.

4.4.2 Geometric albedos

The geometric albedo of the planet is known to be time-varying. Lockwood et al. (1983) showed that the y-band (550 nm) albedo increased over the timespan 1972-1981, even when the increased solar-facing cross section was taken into account. In Table 4.5 we show the geometric albedos of our work and of Karkoschka (1994) integrated over our bandpasses. In addition we include the near-infrared work of this study in broadband J, H, and K in comparison to broadband filter images from the dataset of Chapter 3. In all visible filters the value has gone down over the two year time period. This is explainable if the extent of the brighter polar cap (see Figure 4.1) has remained similar over time. As the planet moves from solstice to equinox, the projected area of this cap decreases. In fact a dedicated photometric effort in b and y bands shows a steady decrease in brightness over the past decade (Lockwood 1997). If in fact the haze has been increasing since Voyager, this can also account for a decrease in albedo. Therefore our 1995 results are consistent with a decreasing albedo.

To accurate portray the albedo over the geometry at this time every point on the HST WF 7274 Å filter was mapped to its viewing parameters. The geometric

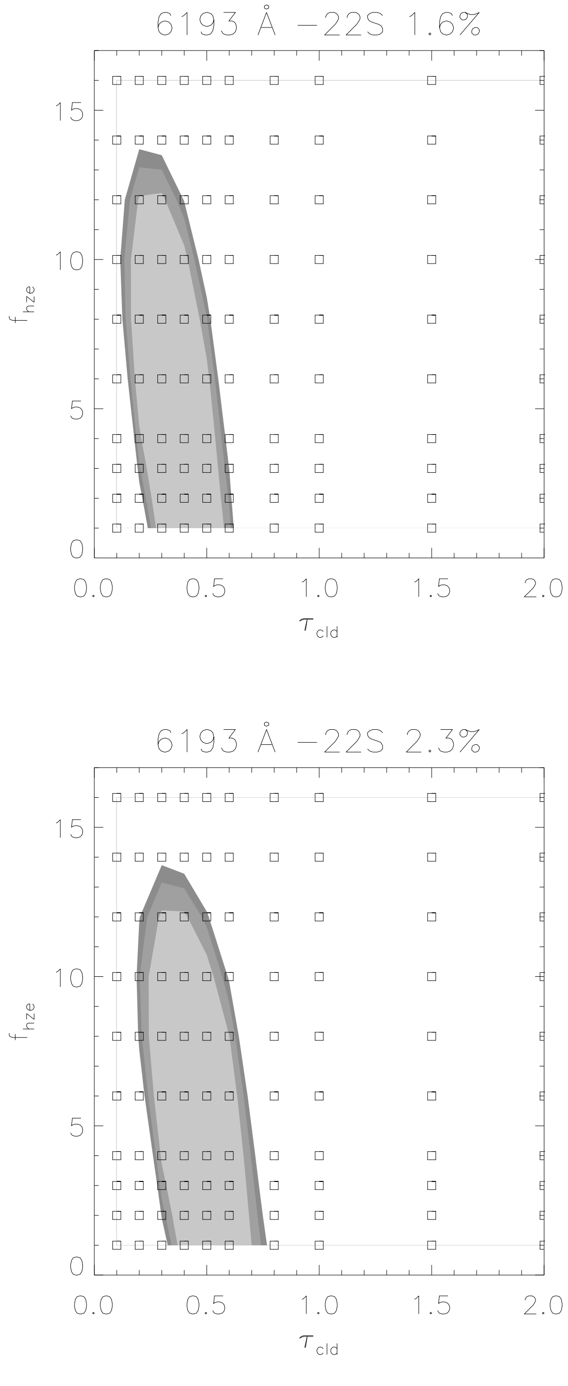

Figure 4.8: A comparison of the effects of the tropospheric CH_4 mixing ratio. In box (a) the 1.6% ratio of Baines et al. (1995a) is used to compute a monochromatic solution matrix for 6193 Å, while the Voyager mixing ratio of 2.3% (Lindal et al. 1987) is used in box (b), requiring a slightly thicker cloud to produce the observed results, however this difference is within the model error.

Table 4.5: Geometric albedos over time

λ (μm)	1993	1995	1996
0.4682	0.598 ± 0.024	0.576 ± 0.029	
0.6193	0.143 ± 0.006	0.137 ± 0.007	
0.6733	0.337 ± 0.013	0.295 ± 0.015	
0.7274	0.048 ± 0.002	0.042 ± 0.002	
1.26		0.0178 ± 0.0010	
1.62		0.0179 ± 0.0008	0.0320 ± 0.0004
2.21		0.00012 ± 0.00004	0.00029 ± 0.00004

albedo is then computed by averaging the absolute reflectivity at each point. This result for different values of f_{hze} then allows the determination of the scaling factor for 4682 Å, 7274 Å and K in 1995, $f_{hze} = 6 \pm 3$, and 4682 Å and 7274 Å in 1993, $f_{fhze} = 10 \pm 3$.

4.5 Discussion

The near-IR observations in chapter 3 suggested that the column number density of haze particles in the Uranian atmosphere had increased by a factor of 20 in 1996 over the Voyager values. This increase was extreme enough to hide the cloud asymmetry in continuum filters (their Figure 4.1). This work confirms that the haze column density is in fact a time-varying phenomenon. Atreya et al. (1991) predict a haze production at the poles 16 times greater than that at the equator, due to the increased insolation and change in zenith angle across the disk. The magnitude of this change in the intervening years is illustrated in Figure 4.9, which displays the variation of the disk-averaged haze scaling factor f_{hze}, which is a comparison to the Voyager results of Rages et al. (1991). The haze profile appears to have changed rapidly between the 1995 and 1996 observations. The observed factor of 3 increase in the haze column density was sufficient to camouflage the asymmetry in the CH_4 cloud.

The profile of Rages et al. (1991) came from a microphysical model calibrated by detection of hazes with a number density of 2-3 cm^{-3} and a mean particle size of 0.1 μm at 44 mbar. We investigated the possibility that the increased haze column densities reported here and in Walter and Marley (1997) arise from sensitivity to a different atmospheric layer than probed by Rages et al. Using the layers as defined in their work for the Voyager 2 WA Blue filter we computed the values for their 19° phase angle observations using both the baseline haze and a model where the haze column abundance below 200 mbar is increased by a factor of 10. As seen in Figure 4.10 the Rages et al. baseline haze model better fits the data. The disparity would be greater if the column density from 44 to 200 mbar was also increased. Hence the variation in best-fit haze profile since Voyager represents a true time-variation, and not an observational one.

While the haze column density has increased, the column density of the CH_4 cloud has taken the opposite turn since Voyager. The total optical thickness at -22.5 and -65 ° latitude has decreased significantly in the interim, dropping from a mean disk-averaged value of 1.5 to 0.6. In 1996 the best fitting value was 1.5, however this was determined at 1.58 μm. This is not easily compared to values

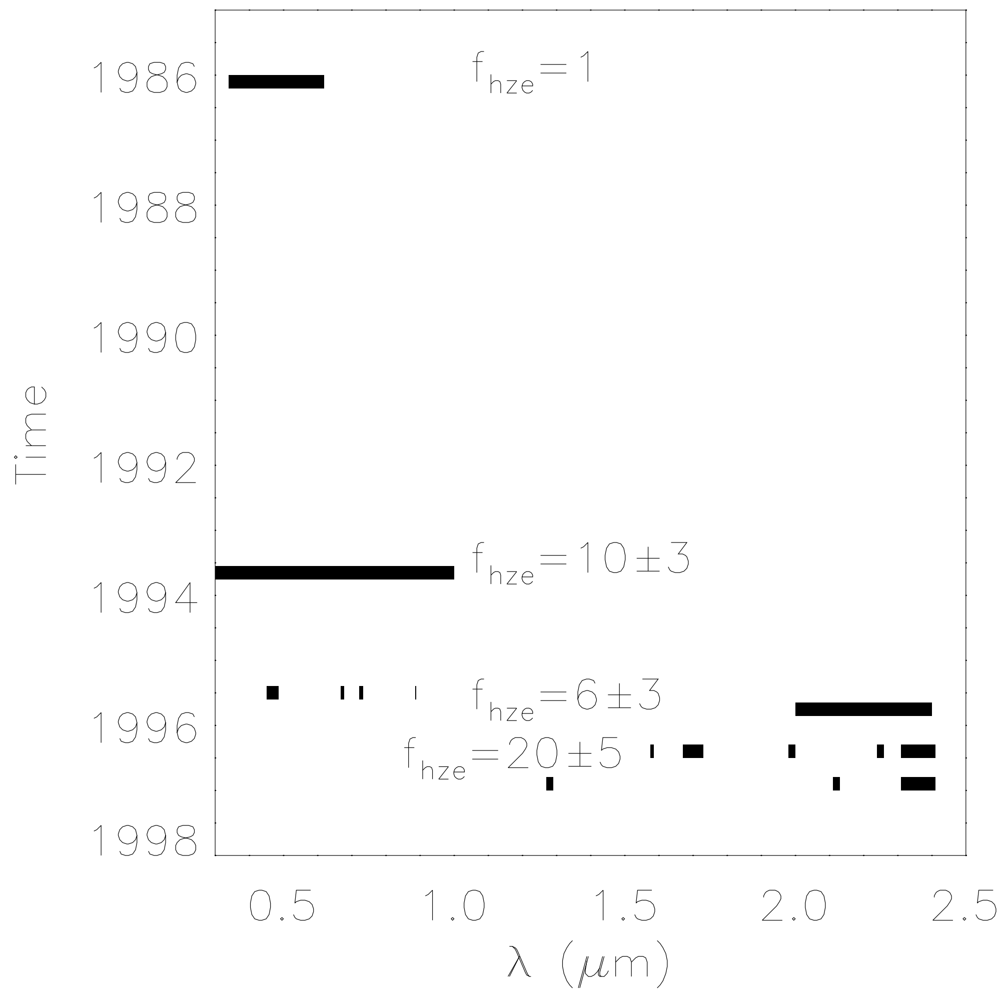

Figure 4.9: The column density of haze particles over the time period since Voyager. All known studies are included, including the baseline haze f_{hze}=1 of Rages et al. (1991) determined from 7 Voyager 2 filters in the optical, the spectroscopy of Karkoschka (1994), this work, and the near-IR imaging of Walter and Marley (1997). Shown additionally are those portions of the spectrum used to derive the values. The amount of haze has varied considerably over this time period, with significant variation taking place between 1995 and 1996.

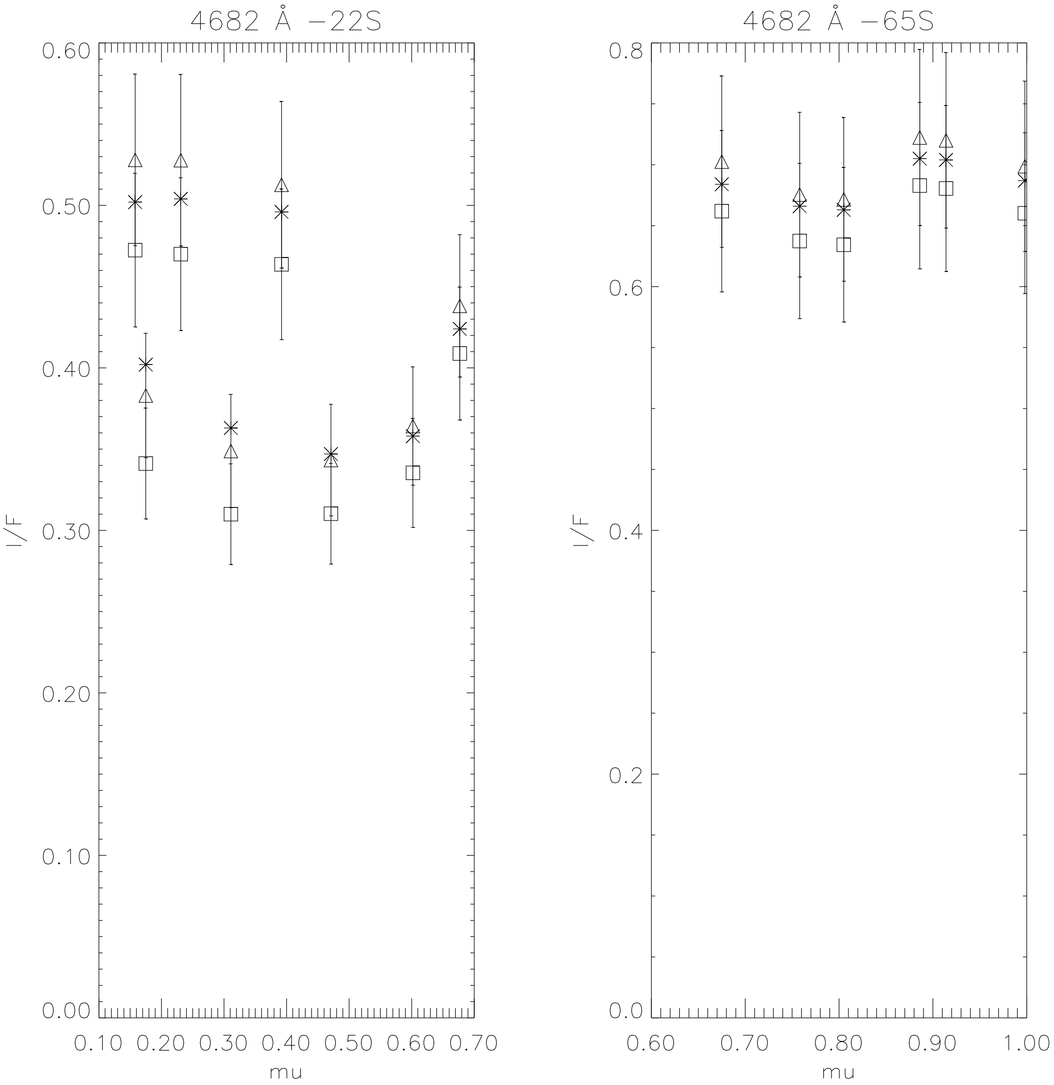

Figure 4.10: Comparison of our haze models to that of Rages et al. (1991). Asterisks represent individual data points at (a) -22.5° and (b) -65° taken at 19° phase angle by Voyager 2's WA Blue filter (center 474 nm). Triangles represent a fit computed by our code with the exact Rages model at 4700 Å, while squares are the values produced by increasing the haze below 200 mbar by an order of magnitude. Errors are 12%, from the modeling and photometry. At -22.5° the baseline haze model clearly is the better fit, although this is not as certain at -65°.

derived in the optical, since the cloud, whether pure CH_4 or a mixture of CH_4 and higher order hydrocarbons as modeled by Rages et al. (1991) is likely to be non-grey.

In the region of the CH_4 cloud deck, the temperature profile as seen by Voyager (Lindal et al. 1987) is very steep. It is also possible that the constant insolation received on the southern hemisphere has increased the tropospheric temperature profile by a few degrees, causing an imbalance in the production and evaporation of cloud particles, leading to a net loss. As Uranus continues towards equinox continuing observations are needed to examine these effects to see if the cloud thickness continues to decrease as expected.

Chapter 5

TEMPORAL EFFECTS ON THERMAL EMISSION

5.1 Introduction

One of the biggest unexplained problems in the Uranian atmosphere is energy and mass transport (Lunine 1993). The stratosphere is 15K warmer than predicted by models, and hazes observed by Voyager do not seem to be responsible (Marley et al. 1997). Either there is a yet undiscovered opacity source residing in the stratosphere, our understanding of the composition is flawed, or there is some other undiscovered heat source.

Uranus is unique among the planets of our solar system in that its rotation axis is inclined 98° to the ecliptic, resulting in essentially 42 consecutive years of constant sunlight alternating on each hemisphere. When Voyager 2 surveyed the Uranian system in 1986, the planet was at winter solstice, yet within the measurement errors, the poles and equatorial region had similar temperature profiles.

Because of the long (1.6 Uranian years) radiative time constant, nearly a full seasonal lag is expected, causing the poles to be effectively at equinox and equal in temperature. However the fact that the equator was in equilibrium with the poles while receiving less annual sunlight suggests a powerful method of dynamic meridional heat transport.

To explain the excessive heating, 15% of the incident solar radiation must be deposited in the stratosphere (Appleby 1986). Although modeling by Marley et al. (1997) shows that the stratospheric hazes seen at the time of Voyager cannot be responsible for the extra absorption, recent discoveries of temporal variation of scatterers in the Uranian atmosphere points to a yet-incomplete picture.

In the previous two chapters results were presented that suggest in 1995 and 1996 the column density of scatterers above the CH_4 cloud increased by an order of magnitude since Voyager while the column density of cloud particles decreased. Because the production of haze particles is fueled by UV photolysis of stratospheric CH_4 this can be explained by the increased sunlight received by the facing southern hemisphere. This rise in deposition of solar energy could also serve to increase the upper tropospheric temperature, causing a melting of cloud particles.

Marley et al. (1997) derived a temperature profile for Uranus constrained by Voyager 2 observations. This chapter seeks to produce a profile consistent with the recent observations to predict the spectrum of the planet in the thermal infrared to aid future observers, and discusses some of the observational issues.

5.2 Atmosphere Model

The radiative-convective equilibrium model was modified from that of Marley et al. (1997). Their work is the first attempt at a self-consistent radiative-convective model for the atmosphere since that of Appleby in 1986. The model is based upon one derived for the atmosphere of Titan (McKay 1989). There are 42 plane-parallel layers spaced equally in log P from 2.5 μbars to 20 bars. Calculations take place in the thermal infrared over 56 spectral intervals in the thermal IR between 5.7 and 3300 μm, and 36 intervals in the reflected solar spectrum from 0.275 to 4.22 μm.

The model is allowed to relax to radiative equilibrium, with the temperature profile adjusted until the flux in and out of each layer are equivalent. The radiative transfer equation is then solved up to eight times, once for each k-coefficient (see chapter 2) with the resultant flux a weighted sum of each computation.

When radiative equilibrium is achieved, the lapse rate of each layer starting at the bottom is examined. If it exceeds the adiabatic lapse rate the layer is considered to be convective, its temperature is adjusted to reflect that fact, and the model is recomputed. Up to two convective regions are allowed for by the model, which are not constrained by radiative equilibrium.

For each layer of the model three parameters need to be calculated, the total optical depth τ, mean single-scattering albedo $\tilde{\omega}$, and mean asymmetry parameter $< \cos\Theta >$. The final two are calculated by weighting by the optical depth from each source. In the thermal infrared the wavelengths involved are much longer than the particle sizes, so scattering is neglected.

Rayleigh scattering and H_2 opacities are calculated as in previous chapters. Hydrocarbons are somewhat more complicated because these calculations are over specific spectral intervals, not monochromatic as in previous chapters. A full and rigorous treatment of these gasses would require integration over tens of thousands of individual lines. Clearly a statistical treatment is required, and so k-coefficients are used.

In the optical the haze parameters are calculated as in previous chapters, with the scaling factor f_{hze} determined by the observations. In the thermal IR indices of refraction of liquid C_2H_2 and C_2H_6 (in their appropriate atmospheric regions) are input into the Mie code to derive Q_{abs} (Khanna et al. 1988, Marley et al. 1997).

The two tropospheric clouds are slightly more complicated. Column densities are determined by scaling the input optical depths using assumed particle sizes of 1 μm and Q_{abs}=2, the limit for geometrical optics with no scattering, appropriate for a scattering parameter $x \gg 1$.

Single scattering albedos are highly dependent on wavelength. Most previous work in establishing these value for the Uranian atmosphere has been for $\lambda < 0.6\mu$m. Beyond that in many cases absorption from CH_4 and H_2 above the cloud decks makes characterization of this property impossible, yet unnecessary for studying solar deposition.

For the CH_4 cloud the fit of Baines et al. (1988) is used between 0.35 and 0.55 μm,

$$\tilde{\omega}_{cld} = \left(1 + 0.131 \left(\frac{0.35}{\lambda}\right)^{8.36}\right)^{-1}, \tag{5.1}$$

0.9 for $0.55 < \lambda < 0.65\mu$m (Baines et al. 1995), 0.8 for $0.65 < \lambda < 0.85\mu$m (determined for the similar cloud in Neptune by Baines and Hammel 1994), and 0.95 for longer wavelengths. The last is speculation, but at longer wavelengths Mie theory predicts largely non-absorbing particles unless the particle is highly interacting (large imaginary index of refraction n_i). At these wavelengths few solar photons penetrate to these depths, so it is an acceptable approximation for the whole near-IR.

In the case of the H_2S cloud the work of Wallace (1980) is used, $\tilde{\omega}_{cld2} = 0.9985, \lambda < 0.64\mu$m. Between 0.64 and 0.80 μm again it is necessary to turn to the work of Baines and Hammel (1994) for Neptune,

$$\tilde{\omega}_{cld2} = \left(1 + 0.106 \left(\frac{\lambda}{0.35}\right)^{3.66}\right)^{-1}. \tag{5.2}$$

Longward of this is again mostly speculation. Marley et al. (1997) find some absorption to be necessary beyond 0.8 μm and use a value of 0.8. The study described in chapter 3 did not require as much absorption in the near-infrared, thus the value 0.9 is adapted.

In the thermal infrared both clouds are treated using Mie theory with the well-established optical constants of CH_4 and H_2S (McKay et al. 1989, Marley et al.

1997). The CH_4 profile used is similar to that in Chapter 3, with the adaptation of the Baines et al. (1995) 1.6% tropospheric mixing ratio in the lower troposphere and 10^{-5} in the stratosphere.

5.3 Temperature Profile and Spectrum

Two temperature profiles have been computed with this model, one using the conditions present during the Voyager epoch, and one using those present during the 1995 observations, presumably still the case as of this writing. As explained by Marley et al. (1997), current models fail to reproduce the stratospheric temperature profile, typically deriving temperatures 10–15 K cooler. This can be improved by depositing 10 erg cm^{-2} sec^{-1} at 10 mbar using a Chapman energy deposition profile (Chamberlain and Hunten 1987) with a scale height of 35 km, however this does not have a noticeable effect above 1 mbar, where mid-infrared observations centered on hydrocarbon fundamental bands tend to probe.

In Figure 5.1 the inability of models to reproduce the observations can be seen in the solid line, a temperature profile computed for this work, compared to the dashed line, the Voyager RSS results (Lindal et al. 1987). The stratospheric profile is even cooler than that in Marley et al. (1997) due to decreasing the stratospheric CH_4 mixing ratio from 10^{-4} to 10^{-5}, a value allowed by chapter 3. A mixing ratio of 10^{-4} produces albedos that are too low, while using a value less than 10^{-5} creates and even greater discrepancy between the model and observed stratospheric temperatures.

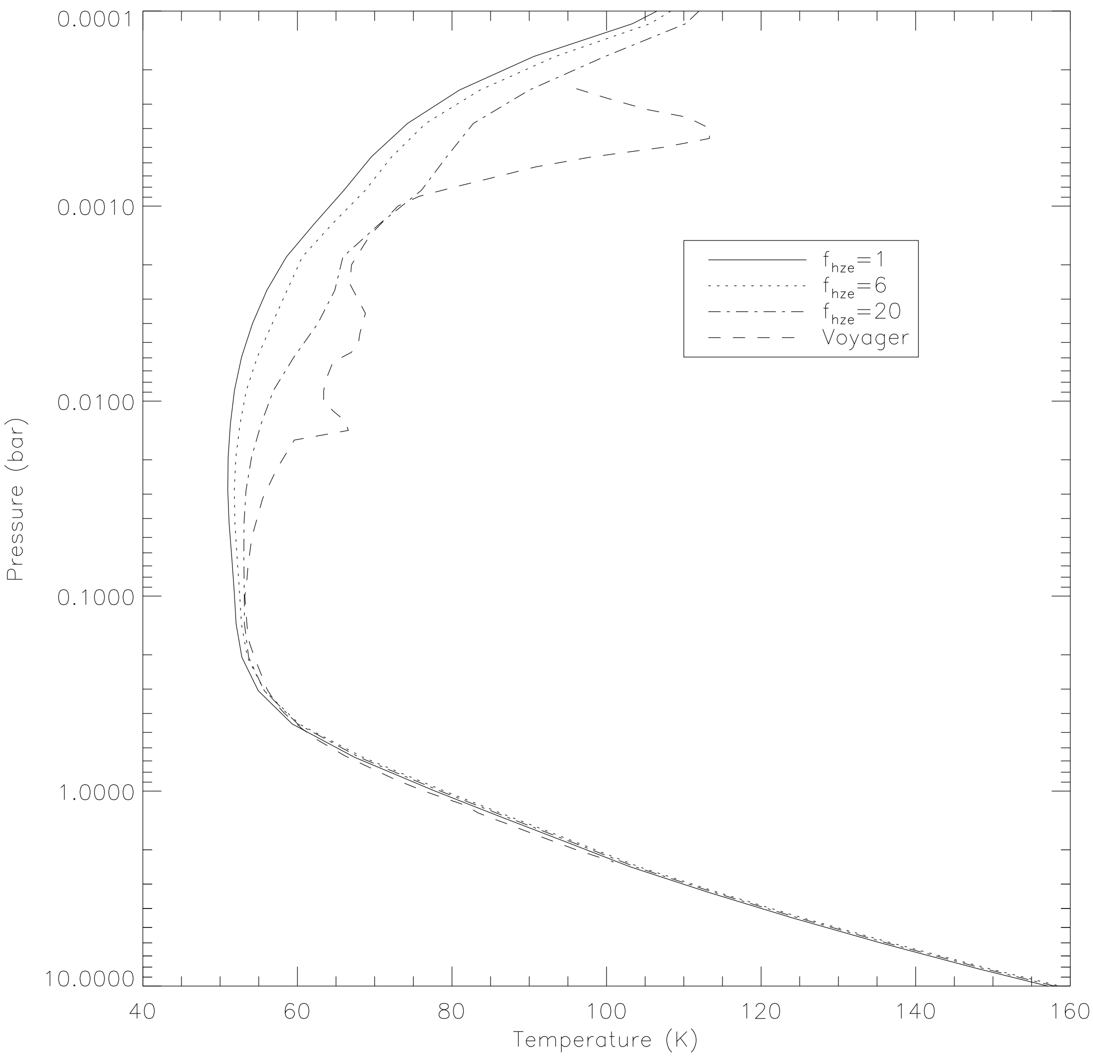

Figure 5.1: The solid line represents the model temperature profile for the Voyager epoch, with haze scaling factor f_{hze} of 1 and CH_4 cloud optical depth of 1.5. Voyager RSS results (Lindal et al. 1987) are given for comparison in the dashed line. Model temperature profiles for 1995 and 1996 are included as the dotted and dash-dot lines, showing an increase in the haze column density is an effective heat source for the stratosphere.

The reasons for this discrepancy are as yet not understood, although the bumps visible near 5 and 12 mbar could be related to discrete condensation layers beyond the vertical resolution of this model. Mid-infrared observations are sensitive mainly to the region above 1 mbar as well as the lower stratosphere/upper troposphere. This discrepancy can be quantified in Table 5.1 (and seen in Figure 5.2), where the brightness temperatures of the Voyager and post-Voyager epochs are compared to mid-IR and microwave observations taken in the first half of 1980's. The discrepancy is mainly visible shortward of 14 μm, where the fundamental transitions of C_2H_2, C_2H_6, and CH_4 lie, causing observations to probe the much hotter upper stratosphere. In the longer window the main opacity source is H_2, causing these regions to probe the cold upper troposphere where the H_2 optical depth reaches unity.

In comparing the Voyager epoch to 1995, the optical depth of the CH_4 cloud decreased from 1.5 to 0.6. This causes the troposphere to heat by approximately 1 K because a smaller number of cloud particles are not as effective in shielding the incoming photons from lower regions. Since the majority of thermal emission of Uranus comes from this region, an increase in the effective temperature would be expected. This is reasonable, as Friedson and Ingersoll (1987) predict seasonal temperature changes of this magnitude. Because of the seasonal lag brought on by poor radiative transport at such cold temperatures, an increase in temperature of the largely facing southern hemisphere is consistent as it moves away from

Table 5.1: Brightness temperatures are given for Voyager epoch ground-based observations and models for Voyager epoch, 1995, and 1996. Data are from: 8-23 μm taken on May and June 1985 by Orton et al. (1987, 1990), 30-61 μm taken on April 1985 and referenced by Conrath et al. (1991), 224 μm taken on May 1980 by Hildebrand et al. (1985), 371 and 1320 μm taken on April 1982 and April 1994 by Orton et al. (1986), and 2632 μm taken on June 1984 by Muhleman and Berge (1989).

Model center (μm)	$T_{B,voy}$	$T_{B,1995}$	$T_{B,1996}$	Observation (μm)	$T_{B,obs}$
2500.000	121.70	123.39	122.69	2632.00	128.6 ± 2.0
1333.333	97.19	98.63	98.05	1320.00	91.3 ± 2.1
666.667	76.06	77.32	76.88		
363.636	63.94	64.96	64.72		
222.222	59.10	60.00	59.90	224.10	60.7 ± 1.5
153.846	57.54	58.38	58.34		
117.647	57.20	58.02	58.00		
95.238	57.26	58.08	58.06		
80.000	57.53	58.35	58.31		
68.966	57.93	58.75	58.69		
60.606	58.41	59.23	59.14	60.13	60.9 ± 0.2
54.054	58.87	59.70	59.59	53.73	60.9 ± 0.1
48.780	59.15	59.96	59.84	48.64	61.5 ± 0.1
44.444	58.86	59.66	59.55		
40.816	57.55	58.33	58.27	40.31	60.3 ± 0.2
37.736	55.28	56.04	56.11		
35.088	53.17	53.93	54.23	35.03	54.6 ± 0.4
32.787	52.07	52.85	53.45	32.46	54.0 ± 0.5
30.769	51.63	52.48	53.43	30.67	53.6 ± 0.4
28.986	51.44	52.40	53.69		
27.397	51.41	52.43	53.87		
25.974	51.43	52.42	53.81		
24.691	51.48	52.42	53.67		
23.529	51.55	52.45	53.56		

(table continues)

Model center (μm)	$T_{B,voy}$	$T_{B,1995}$	$T_{B,1996}$	Observation (μm)	$T_{B,obs}$
22.472	51.64	52.50	53.48	22.55	54.2 ± 0.6
21.505	51.74	52.57	53.44	21.39	53.7 ± 0.3
20.619	51.85	52.66	53.44	20.81	54.2 ± 0.3
19.802	51.97	52.77	53.47	19.94	55.2 ± 0.4
18.868	52.07	52.86	53.54	18.78	55.0 ± 0.5
17.857	51.90	52.71	53.60	17.62	56.4 ± 0.4
16.949	51.77	52.66	53.86		
16.129	51.85	52.71	53.86		
15.209	52.12	52.93	53.82		
14.286	52.47	53.29	54.16		
13.514	54.92	56.18	58.36	13.44	72.7 ± 0.5
12.945	53.79	55.03	56.90	12.97	68.2 ± 0.6
12.500	55.15	55.96	56.29	12.38	64.7 ± 1.0
12.048	57.12	57.93	58.17	12.14	66.7 ± 0.8
11.554	59.42	60.17	59.88	11.43	68.6 ± 1.0
11.025	60.62	61.39	61.05	10.84	70.2 ± 1.0
10.537	58.56	59.36	59.11		
10.101	62.39	63.21	62.83		
9.709	67.49	68.35	67.90	9.66	79.4 ± 1.3
9.302	72.31	73.18	72.71	9.31	83.4 ± 1.4
8.889	73.33	74.00	73.63	8.95	84.9 ± 0.8
8.565	69.81	70.33	70.07	8.72	84.4 ± 1.2
8.299	72.42	73.05	72.73		
8.000	75.03	75.50	76.09		
7.692	85.08	85.54	86.51		
7.407	80.53	80.99	81.97		
7.143	81.50	81.81	81.65		
6.897	81.24	81.47	81.29		
6.689	79.23	79.47	79.36		
6.452	106.55	107.55	107.11		
6.154	108.58	109.64	109.18		
5.865	112.20	113.30	112.83		

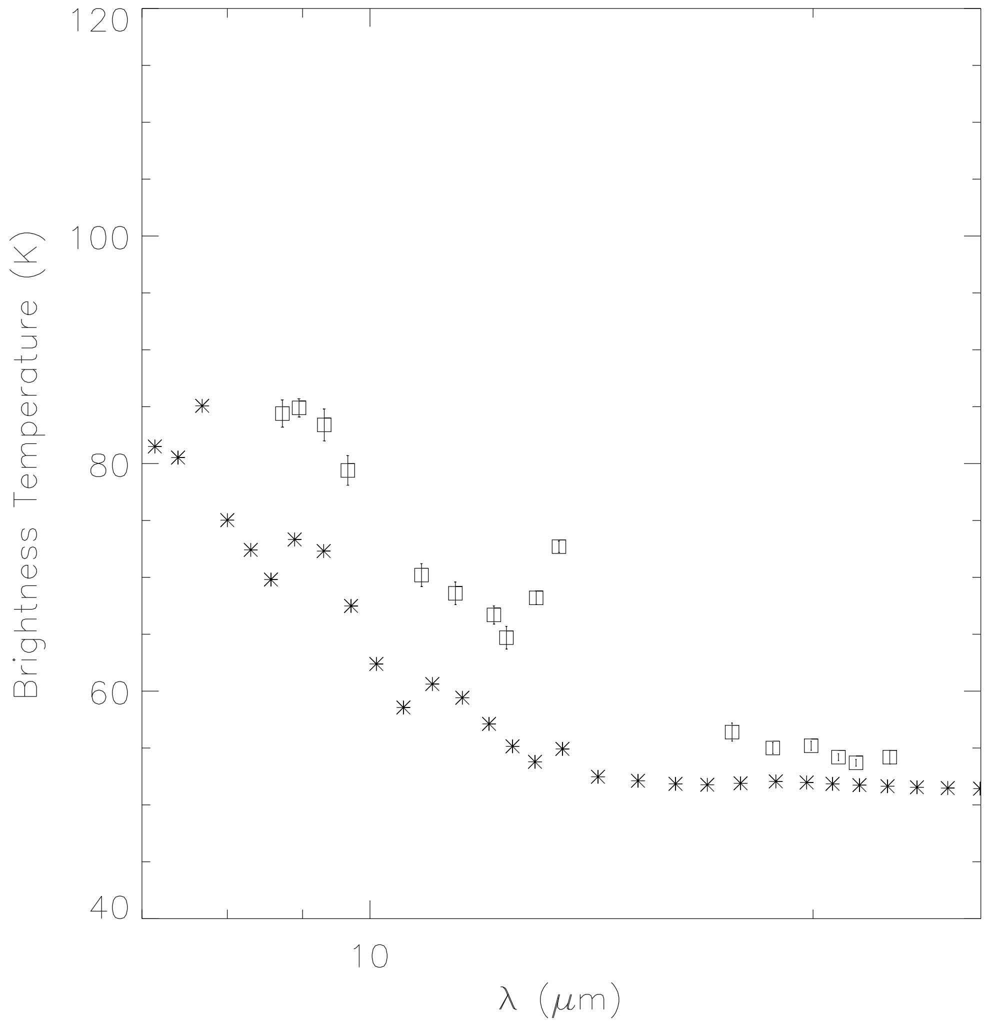

Figure 5.2: In asterisks are the model predictions for the brightness temperatures from 7-26 μm, as compared to the observations (displayed as squares) of Orton et al. (1987, 1990). Bandwidths of the observations ranged from 0.4–6%. The fits are much more robust at longer wavelengths, where most radiation to space comes from the upper troposphere, while at shorter wavelengths the problems with energy absorption in the stratosphere cause model temperatures much cooler than predicted. The model does correctly predict trends in the spectrum.

summer into fall. In fact this heating may also be somewhat responsible for the decrease in cloud particles.

In the stratosphere and upper troposphere the new model is computed with 6 times the column density of haze particles as seen by Voyager. This is the 1995 value, and is more likely to be the current case than the value of 20 in 1996 as reported in Chapter 3. The reasoning behind this lies in the blocking of the cloud asymmetry in the 1996 data by the large haze column density. Recent HST observations (Karkoschka, personal communication) show the return of the asymmetry, implying the production of haze particles has diminished in the ensuing year.

A haze scaling factor of 6 also causes an increase in heating in the stratosphere, as the non-conservative scattering particles absorb some of the incoming photons. Tests showed the temperature increases from the increase in haze particles and decrease in cloud particles to be largely independent of each other.

As seen in Table 5.1, the increased heating predicts an increase in the brightness temperatures in all wavelengths. Although the model accuracy is poor in the upper atmosphere, if the unknown heating source has remained stable, an increase in the brightness temperature compared to the Voyager epoch observations ought to be detectable. In any case the planet should exhibit an increase in effective temperature.

It is easier to detect a 1 or 2 K increase in brightness temperature than one might initially suspect. In the windows through which ground-based astronomy can be performed, thermal emission is located on the blue or steep side of the Planck function. This has been examined in detail in regards to the detection of seismic waves from the Comet Shoemaker/Levy 9 impacts with Jupiter (e.g., Hunten et al. 1994 and Walter et al. 1996). The relationship between temperature, frequency, and blackbody emission is

$$\frac{d\ln B_\nu}{d\ln T} = \frac{x}{1-e^{-x}} = x, \tag{5.3}$$

for x = hν / kT $\gg$ 1, where B_ν is as described in Chapter 2. In all the sample filters discussed later x is in excess of 10, and increase of 1 K typically leads to $\sim$ 25% more flux, well within the efforts of dedicated photometry. For 2 K increases this value is $\sim$ 60%.

5.4 Theory

The radiance escaping from the top of an atmosphere can be described as

$$I_\nu \propto \int B_\nu(T(\tau_\nu))e^{-\tau_\nu} d\tau_\nu, \tag{5.4}$$

where I_ν is the monochromatic radiance, B_ν the Planck function, T the temperature, and τ the optical depth, defined as dτ = $\kappa\rho$ dz with κ the mass absorption coefficient, ρ the density and dz the relative height in the atmosphere.

In order to make this a linear problem it is necessary to compare the derived temperature profile to a reference profile, giving the equation

$$\Delta I \propto \int K(\nu, z) f(z) dz, \tag{5.5}$$

with K(ν,z) defined as $\frac{dB}{dT}$ e$^{-\tau_\nu}$ and f as dT. Δ I and Δ T are the result of subtractions from the assumed model. In matrix form this is ΔI = Kf. Here ΔI, the radiance, is the data matrix. K is the model, known in this case as the contribution function (as plotted in Figure 5.1), which shows the effective contribution to the outgoing flux as a function of height. Finally the parameter to be solved for is f.

Because this is an overdetermined problem, with data available at several wavelengths and only the temperature to be derived it can be solved for if the model matrix is not singular.

$$f = (K^T K + \gamma I)^{-1} K^T \Delta I, \tag{5.6}$$

where γ is the result of a rolloff filter intended to minimize the contribution given by those eigenvalue below the noise level.

5.5 Proposed Observations

Determining the temperature profile of an atmosphere is a difficult subject. As a first approximation brightness temperatures derived from different wavelengths can be assigned to the depths from which they arise. A rigorous approach however requires sounding measurements from as many atmospheric levels as possible. The most basic technique involves find the pressure level where a spectral band achieves unit optical depth and then assigning the band brightness temperature to that level. As figure 5.1 shows however, the contribution at a particular wavelength can be spread across many pressure levels.

In any branch of science predictions are useless if they can't be confirmed. The best method to confirm the temperature profile of a planet to observe it in a part of the spectrum where its emission spectrum dominates the reflected sunlight spectrum. This is in the mid-infrared (also known as the thermal infrared). Through Wien's law, an effective temperature of 59.1 K (Pearl et al. 1990) equates to a peak emission near 50 μm. However Uranus can be observed quite a bit shortward of this, with the higher brightness temperature blueward of 14 μm serendipitously extending the observation range even further.

Because the mid-infrared is home to the fundamental rotovibrational bands of most molecules that are present in the earth's atmosphere (e.g., CO_2, H_2O), it is difficult to observe from the earth's surface. Fortunately there are two windows through which observations are possible, 8-14 and 17-26 μm. The second window is very slightly water vapor dependent, so it's important to observe at high elevation such as Mauna Kea, above most of the offending water. Major observational programs of Uranus in the mid-infrared have not been attempted since the end of the Voyager 2 encounter (Orton et al. 1987), and the IRIS camera on Voyager probed further out in the infrared, from 50-100 μm.

Each of the two available observational windows allows study of different portions of the atmosphere. The 17-26 μm region is key for resolving the stratospheric questions because the emission seen forms in the 50-500 mbar region of the atmosphere, just above and below the tropopause. This part of the spectrum is dominated by pressure-induced absorption (PIA) from H_2. As a homonuclear molecule H_2 does not have a permanent dipole moment, however a dipole can momentarily be induced by collision with another molecule. With the number mixing ratio of H_2 being 85% in the atmosphere of Uranus, this can become a significant opacity source. H_2 has two forms for which the characteristic behaviors are slightly different. The molecule is in the para state when the spins of the two H molecules are antiparallel or even. When they are parallel or odd the molecule is said to be in the ortho state. The transitions that exist in the spectrum of interest are the S(0) 0-2 transition of para hydrogen centered at 28.2 μm and the S(1) 1-3 transition of ortho hydrogen centered at 17.0 μm. Because of the short timespan involved in the creation of the dipole, the wings from these lines are broad enough to cover the entire window. Since optical depth for molecular hydrogen reaches unity near the tropopause, this is where a study of these lines would probe.

The other terrestrial window of interest allows probing of this region as well as the upper stratosphere, because although PIA is important here, hydrocarbons provide a significant portion of the overall opacity as well. Both ethane with an emission band centered at 12.2 μm and acetylene with a band at 13.7 μm exist in the stratosphere as optically thin hazes as well as in gaseous form. These are created by the breaking apart of methane by UV photons between 0.1 to 1 mbar. In addition, CH_4 has an important fundamental transition at 7.8 μm.

The remainer of this chapter discusses the issues involved in imaging the planet in the thermal infrared. For illustration purposes I have assumed using the MIRAC camera (Hoffmann et al. 1993, Hoffmann et al. 1994) on the 3 meter IRTF telescope on Mauna Kea, HI. These numbers will improve as the new generation of 6-10 meter telescopes comes on line in the next few years, several of which are being designed to have mid-infrared observing capabilities.

Special techniques have been developed for mid-IR observing. An excellent discussion of these can be found in Fisher (1994). To briefly summarize, it is necessary to chop the telescope secondary mirror at a rate of many Hertz to quickly obtain a sky image for each object image. This is necessary because i) the sky background dominates even the brightest mid-IR object, and ii) the sky background properties in the mid-IR change drastically on the order of seconds. Another correction is necessary to account for the different optical paths both images have traversed. After every group of observations (typically 5-10) the telescope is then nodded slightly off target, and a new set of images is taken with chopping. The brings down the duty cycle immensely, but if the object is significantly smaller than the field of view this can be counteracted by directing the throws to have the object in all four beams in different corners of the image.

Depending upon the composition and opacity distribution of the atmosphere, emission seen at a particular wavelength does not form at a single level. Figure 5.1 shows the contribution function for several of the filters to be used at two incident angles. Measurements at several wavelengths can be used to invert the integral, solving for temperature as a function of height. The top of Figure 5.1 shows the contribution functions for normal incidence (i.e. 0°) while the bottom is calculated for solar incidence of 78°. At normal incidence the long wavelength filters probe the upper troposphere, while shorter filters probe the upper stratosphere. The ability to resolve the limb-darkening of the planet increases the temperature resolution, shedding insight on a broader region of the atmosphere where optical depth of unity is reached higher.

To obtain the proper resolution it is important to have near diffraction-limited seeing, which gives 2 resolution elements across the planet's diameter and 5 on the disk in the 17-26 μm window. Considitons are somewhat better in the shorter window due to the wavelength dependence, where useful data can be obtained even in non-ideal conditions. A primary difficulty in mid-infrared observing is tracking due to the short observation times. In order to assure the continued tracking of a dim mid-IR object such as Uranus it is necessary to regularly image it in bright bandpasses. The best candidates for this are either the longest wavelength available (20.6 μm on MIRAC2), climbing the steep end of the Planck function, or at a wavelength with an extraordinarily high brightness temperature. The M filter, centered at 4.8 μm is especially valuable in studies of giant planet. The reason for this is the lack of strong opacity sources, allowing the deepest regions of the planet to be sounded. In both these filters 3σ images can be acquired with

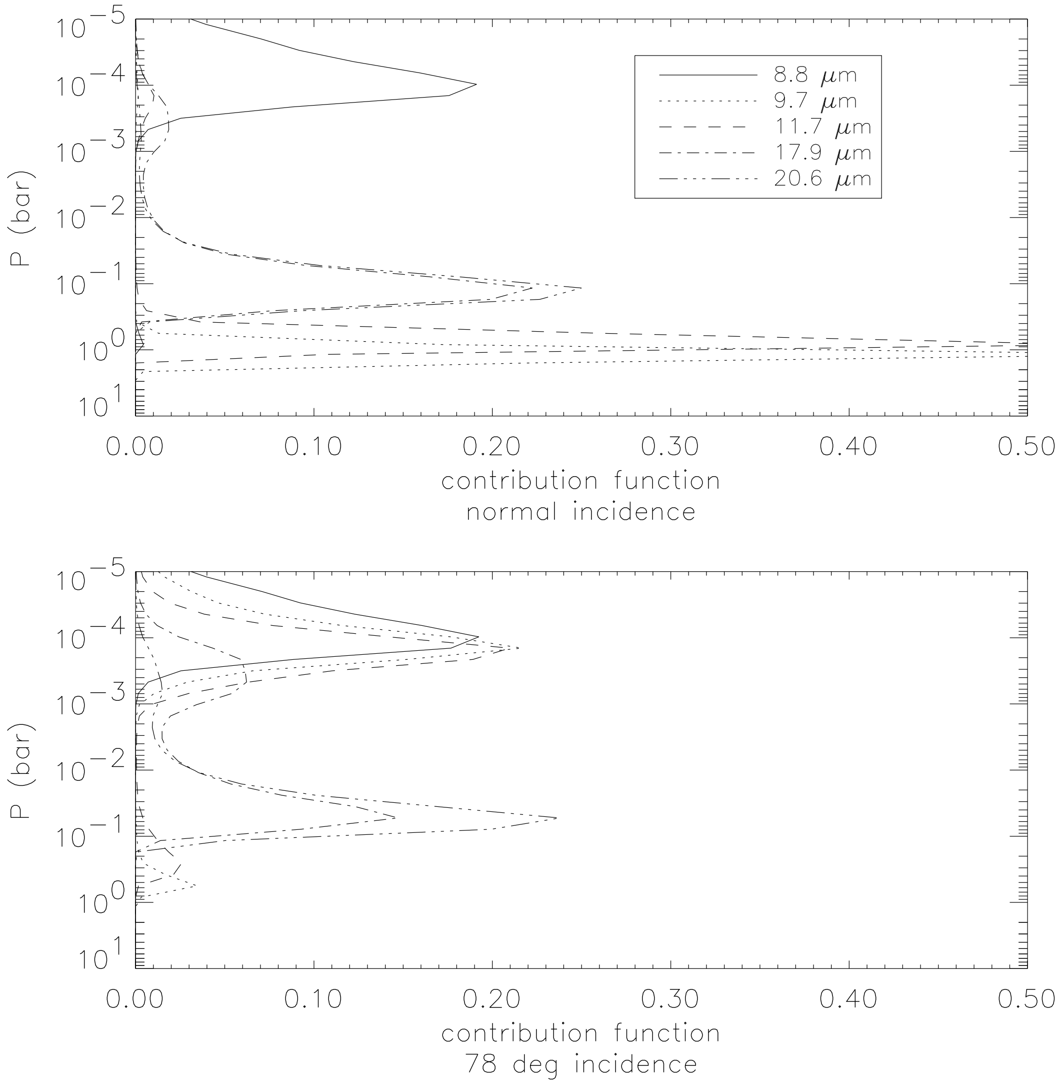

Figure 5.3: The contribution function for several mid-infrared filters is shown for normal incidence at 78° zenith angle (near the limb). The contribution function represents how much each level of the atmosphere contributes to the outgoing radiation. Near the limb an optical depth of unity is reached higher in atmosphere, and thus a different atmosphere level can be probed. Observations at the center and limb of a particular latitude can then be used to model a greater portion of the atmosphere.

observation times of less than 30 seconds. By comparing the observed brightness temperatures from Table 5.1 to the empirically determined noise equivalent flux density, observing in all four beams and allowing for calibrations and tracking, the planet can be observed to 5σ in 8.8 and 9.7 μm, 10 σ in 11.7 μm, and 20 σ in 17.9 μm in 10 hours of telescope time. Observations similar to these should be performed every few years to properly track the temperature fluctuations.

Chapter 6

CONCLUSIONS

6.1 Review

This work contains a multi-wavelength study of the conditions in the visible Uranian atmosphere in 1995 and 1996, 9 and 10 years after the visit by Voyager 2. In the first project Uranus was imaged using the ARC 3.5 Meter Telescope at Apache Point Observatory in seven narrowband filters centered from 1.28 to 2.36 μm in June and October 1996. The geometric albedos of the planet in these filters served as the baseline for a disk-averaged model of the planet's atmosphere. Results show that the column number density of haze particles in the stratosphere and upper troposphere above the CH_4 cloud increased by a factor of 20 from the Voyager profile derived by Rages et al. (1991). In addition, the best fit for the CH_4 cloud location showed it remained in the same place as seen by Voyager, its optical depth at 1.58 μm was 1.5, and the haze particles were virtually conservative scatterers in the near-infrared.

The second project combined outside datasets consisting of image of Uranus taken in the summer of 1995. Heidi Hammel contributed her J, H, and K broadband images taken from NASA's 3 meter Infrared Telescope Facility at Mauna Kea Observatory. From the Hubble Space Telescope archive were acquired 5 images of the planet. The high resolution of this dataset allowed study of the spatial distribution of scatterers in the atmosphere, so an adding-doubling code was applied to the project. Characteristics of atmospheric scatterers were computed by modeling the absolute reflectivity I/F along scans of the planet at -22.5 and -65° south latitude, which lay completely outside and inside of the observed polar cap. This cap is shown to result from an asymmetry in the CH_4 cloud thickness. The haze scaling factor at both wavelengths is much smaller than in 1996, with derived values of 8 and 5 for the latitudes studied with a disk-averaged value of 6. Although this is smaller than in 1996 it is still measurably larger than during the Voyager epoch. Comparison of these models with the published geometric albedos in 1993 (Karkoschka 1994) shows a similar increase in the intervening time. Although the cloud asymmetry viewed by Voyager remained, at both latitudes the column density of particles has decreased, from an optical thickness of 0.66 to 0.2 at -22.5° and 2.4 to 1.2 at -65° latitude.

The final chapter discussed the likely effects of these changes on the temperature profile and its detectability through imaging in the thermal infrared. Between 1986 and 1995 a universal brightness temperature increase of 1-2 K is predicted due to the increase in haze particles and decrease in CH_4 cloud particles.

The major results of this work is the variability of the haze column density, proven through observations at two separate times modeled with two separate techniques. As discussed in the last chapter it is clear that something significant happened between 1995 and 1996 to increase the haze column density by an additional factor of 3, which is shown in 1997 HST observations to apparently have diminished again. It is with some skepticism that the results are presented solely due to the lack of knowledge of a process that could produce the observed results. Once produced the haze particles slowly drop until evaporating in the upper troposphere. This time scale is thought to be about a Uranian year (84 Earth years), which should mask extreme changes in the column density (Atreya et al. 1991). This is left as the biggest unexplained question of this work.

As Uranus continues towards equinox there are (at least) two competing effects that will determine its observable conditions. First the planet should continue to heat another degree or so due to the inefficiency of the radiative cooling to space as it moves away from solstice. Second the orientation towards Earth of the planet is changing so that less of the polar cap will remain visible. As a result the observed albedo should continue to decrease in continuum bands while remaining the same or slightly increasing in deep gas absorption bands (due to the high haze column density and the hotter temperatures).

As described in the next section, the possibility exists to address many of these questions in the upcoming years. To aid this it is important to discuss some of the weaknesses of this work. The scattering properties of hazes and clouds are often difficult to disentwine. Here are some of the assumptions in the work that could be better investigated:

1. Constituent single-scattering albedos are fixed from other works, or inferred in many places.

2. The haze particles are assumed to be Mie scatterers with the size distribution discovered by Voyager 2.

3. Phase functions are only determined to first order.

4. Polarization effects on Rayleigh scattering are not robustly modeled.

5. The same radius of Uranus is used to model each bandpass, although the areas they probe can differ on the order of hundreds of kilometers.

6. A plane-parallel atmosphere in hydrostatic equilibrium was assumed.

7. The internal heat flow and any near-IR thermal emission was neglected in the visible spectrum studies.

8. Atmospheric dynamics of hazes were not investigated.

6.2 Future Work

The decade from 1995-2005 promised great advances in infrared astronomy as several unprecedented detectors come online. The first of these was the launch of the European Space Agency's Infrared Space Observatory (ISO) into Earth orbit in 1995 (Helou and Kessler 1995). ISO was designed to observe from 2.5–240 μm with a 60 cm mirror. Observations of Uranus have been made already (for example Encrenaz et al. 1997) throughout the thermal infrared.

The second major advance is the refurbishment of HST in 1997 to include the NICMOS camera (Near-Infrared Camera and Multi-Object Spectrometer), allowing diffraction-limited imaging in the near-infrared from 0.8–2.5 μm (Thompson 1994). Because of difficulties with the camera coolant an emphasis has been put to service NICMOS proposals in the next year. Several proposals have already been approved to use NICMOS to observe Uranus.

In the near future mid-infrared cameras will be coming on line at several of the world's largest ground-based observatories among them the 10 meter Keck Telescope (Jones and Puetter 1993). NASA is also involved in two other big projects. The Stratospheric Observatory For Infrared Astronomy (SOFIA) is a 2.5 meter telescope mounted on a Boeing 747, designed to fly high in the atmosphere above most atmospheric contaminants to observe from 1–600 μm (Erickson and Davidson 1995). SOFIA is scheduled for first use in 2001, with a 20 year lifetime. Above the atmosphere completely NASA's last Great Observatory, the Space InfraRed

Telescope Facility (SIRTF) is also scheduled for launch into earth orbit in 2001. SIRTF is designed to observe from 3–180 μm with a 85 cm mirror and a projected 2.5 year lifetime (Werner 1995).

All of these instruments will presumably be used to observe Uranus, at an ideal time in its history as scientists continue to track the planet over one of its years. Recent HST observations (Hammel 1996) show individual cloud features on the disk, the first such features ever seen. With the availability of observing in the mid and far-infrared the thermal structure will be better established. The next step is to expand beyond the disk-averaged radiative-convective models of the present to take advantage of this resolution. In addition the effects of non-spherical particles should be incorporated, particularly when modeling the hazes. More modeling of the production and destruction of haze particles as well as their reflection spectrum would greatly reduce the errors in this and other studies, as would the continuation and improvement of measurements of low-temperature spectrum of CH_4.

Observing programs need not be based in space to yield important information on the planet. Data like that acquired at the IRTF will be more readily available from ground-based observatories, with advances in adaptive optics allowing for even higher resolution, near $0.1''$, imperative for the small ($3.7''$ at opposition) Uranian disk. Even if no major space-based studies are carried out over a period of several years it still is important to carry out a continuous monitoring program to look for other storms like the one that between the 1995 and 1996 data. A simple and yet valuable way to perform this would be yearly J, H, and K photometry of the planet, which is much more sensitive to large changes in the CH_4 cloud (J and H) and haze (K) structure than the better-established optical programs. Ideally narrowband imaging at a variety of continuum and methane bands similar to this work should be performed with some regularity. Wherever possible ground-based observations should be obtained simultaneously with the space-based observations to strengthen the temporal interpretation of the data.

The primary emphasis should be however on mid-infrared imaging to study the emission of the planet, which can better measure heating deviations than scattered sunlight. Without the necessity to consider scattering, results derived there have fewer free parameters and are therefore more accurate. Then the reflected solar spectrum as well as thermal emission can be used in tandem to investigate the changes in this planet. There are several questions that remain unanswered, the source of large short-term storms, the reason Uranus' near-negligible internal heat in comparison to its planet companions, as well as the stratospheric heating problem.

With the recent discoveries (in excess of 20 at this time) of giant planets surrounding nearby dwarf stars it is imperative to gain a greater understanding of our solar system laboratory if we hope to infer the properties of other solar systems. The most important knowledge that can be gained about Uranus as well as the other planets is to understand their composition, as well as the evolutionary process that allowed them to arrive at this state, and what we expect in the future. Understanding the effects that hazes and clouds have on a planetary energy budget leads to more knowledge of atmospheric structure and evolution. Comparing the role of particulates in a large variety of atmospheres gives a greater body of knowledge from which to use to study our own planet.

REFERENCES

Allen, C. W., 1973, *Astrophysical quantities*, Athlone Press, London.

Appleby, J., 1986, *Icarus,* **65**, 383.

Atreya, S. K., Sandel, B. R., and Romani, P. N., 1991, in *Uranus*, Eds. J. T. Bergstralh, E. D. Miner, and M. S. Matthews, 110, Univ. of Arizona Press, Tucson.

Baines, K. H., 1983, *Icarus,* **56**, 543.

Baines, K. H., and Bergstralh, J. T., 1986, *Icarus,* **65**, 406.

Baines, K. H., and Hammel, H. B., 1994, *Icarus,* **109**, 20.

Baines, K. H., Mickelson, M. E., Larson, L. E., and Ferguson, D. W., 1995, *Icarus,* **114**, 328.

Baines, K. H., Terrile, R. J., Smith, W. H., Schempp, W. V., Cochran, W. D., Trafton, L. M., and Smith, B. A., 1988, *Uranus Colloquium*, 3.10.

Baines, K. H., West, R. A., Giver, L. P., and Moreno, F., 1993, *J. Geophys. Res.,* **98**, 5517.

Baines, K. H., Yanamandra-Fisher, P., Lebofsky, L. A., Momary, T. W., and Golisch, W., 1995, *Bull. Am. Astron. Soc.,* **27**, 1088.

Bergstralh, J. T., Miner, E. D., and Matthews, M. S., eds., 1991, *Uranus*, Univ. of Arizona Press, Tucson.

Binder, A. B., and McCarthy, D. W., 1972, *Astrophys. J. Lett.,* **171**, L1.

Biretta, J. A., 1996, *WFPC2 instrument manual*, STSci, Baltimore.

Birnbaum, G., Borysow, A., and Orton, G., 1996, *Icarus,* **123**, 4.

Borysow, A., 1991, *Icarus,* **92**, 273.

Borysow, A., 1992, *Icarus,* **96**, 169.

Borysow, A., Frommhold, L., and Moraldi, M., 1989, *Astrophys. J.,* **336**, 495.

Borysow, A., and Frommhold, L., 1989, *Astrophys. J.,* **341**, 549.

Brown, R. H. 1983. *Icarus,* **56**, 414.

Brown, R. H., and Cruikshank, D. P., 1983, *Icarus,* **55**, 83.

Casali, M. M., and Hawarden, T. G., 1992, *JCMT-UKIRT newsletter*, **3**, 33.

Chamberlin, A. B., Yeomans, D. K., Chodas, P. W., Giorgini, J. D., Jacobsen, R. A., Keesey, M. S., Lieske, J. H., Ostro, S. J., Standish, E. M., and Wimberly, R. N., 1996, *Bull. Am. Astron. Soc.,* **29**, 1014.

Conrath, B. J., Gautier, D., Hanel, R., Lindal, G., and Marten, A., 1987, *J. Geophys. Res.,* **92**, 15,003.

Conrath, B. J., Pearl, J. C., Appleby, J. F., Lindal, G. F., Orton, G. S., and Bézard, B., 1991, *Uranus*, University of Arizona Press, Tucson

Davies, M. E., Abalakin, V. K., Bursa, M., Lieske, J. H., Morando, B., Morrison, D., Seidelmann, P. K., Sinclair, A. T., Yallop, B., and Tjuflin, Y. S., 1995, *Celest. Mech. Dynam. Astron.*, **63**, 127.

de Pater, I., Romani, P. N., and Atreya, S. K., 1989, *Icarus,* **82**, 288.

de Pater, I., Romani, P. N., and Atreya, S. K., 1991, *Icarus,* **91**, 220.

Dlugach, J. M., and Yanovitskij, E. G., 1974, *Icarus,* **22**, 66.

Doose, L. R., Tomasko, M. G., and Eibl, A. M., 1988, *Bull. Am. Astron. Soc.,* **20**, 817.

Elias, J. H., Frogel, J. A., Matthews, K., and Neugebauer, G., 1982, *Astron. J.,* **87**, 1029.

Encrenaz, T., Bezard B., Feuchtgruber H., Lellouch E., de Graauw T., Kessler M. F., Griffin M. J., and Atreya S. K., 1997, *Bull. Am. Astron. Soc.,* **29**, 994.

Encrenaz, T., and Owen, T., 1973, *Astron. Astrophys.,* **28**, 367.

Erickson, E. F., and Davidson, J. A., 1995, in *Airborne astronomy symposium on the galactic ecosystem: from gas to stars to dust*, Eds. M. R. Haas, J. A. Davidson, and E. F. Erickson, 707, Astronomical Society of the Pacific, San Francisco.

Fink, U., and Larson, H. P., 1979, *Astrophys. J.,* **233**, 1021.

Fisher, B. M., 1994, Ph.D. Thesis, University of California, San Diego.

Friedson, J., and Ingersoll, A. P., 1987, *Icarus,* **69**, 135.

Gulkis, S., Olsen, E. T., Klein, M. J., and Thompson, T. J., 1983, *Science,* **221**, 453.

Hammel, H. B., 1996, *Bull. Am. Astron. Soc.,* **28**, 1056.

Hanel, R. A., Conrath, B. J., Flasar, F. M., Kunde, V. G., Maguire, W., Pearl, J. C., Pirraglia, J. A., Samuelson, R., Cruikshank, D., Gautier, D., Gierasch, P., Horn, L., and Schulte P., 1986, *Science,* **233**, 70.

Hansen, J. E., and Travis, L. D., 1974, *Space Sci. Rev.*, **16**, 527.

Helou, G., and Kessler, M. F., 1995, in *Airborne astronomy symposium on the galactic ecosystem: from gas to stars to dust*, Eds. M. R. Haas, J. A. Davidson, and E. F. Erickson, 659, Astronomical Society of the Pacific, San Francisco.

Herzberg, G. 1952, *Astrophys. J.,* **115**, 337.

Hildebrand, R. H., Loewenstein, R. L., Harper, D. A., Orton, G. S., Keene, J., and Whitcomb, S. E., 1985, *Icarus,* **64**, 64.

Hockey, T. and Barnet, C., 1994, *Bull. Am. Astron. Soc.,* **26**, 184.

Hoffmann, W. F., Fazio, G. G., Shivanandan, K, Hora, J.L. and Deutsch, L.K., 1993, *Proc. SPIE, Infrared Detectors and Instrumentation*, **1946**, 449.

Hoffmann, W. F., Fazio, G. G., Shivanandan, K, Hora, J.L. and Deutsch, L.K., 1994, *Infrared Phys. Technol.*, **35**, 175.

Holtzman, J. A., Hester, J. J., Casertano, S., J. T. Trauger, J. T., Watson, A. M., Ballester, G. E., Burrows, C. J., Clarke, J. T., Crisp, D., Evans, R. W., Gallagher III, J. S., Griffiths, R. E., Hoessel, J. G., Matthews, L. D., Mould, J. R., Scowen, P. A., Stapelfeldt, K. R., and Westphal, J. A., 1995, *Publ. Astron. Soc. Pacific,* **107**, 156.

Holtzman, J. A., Burrows, C. J., Casertano, S., Hester, J. J., Trauger, J. T., Watson, A. M., and Worthey G., 1995, *Publ. Astron. Soc. Pacific,* **107**, 1065.

Hunten, D. M., Hoffmann, W. F., and Sprague, A. L., 1994, *Geophys. Res. Lett.*, **21**, 1091.

Jepsen, A. L., Mosher, J. A., Yagi, G. M., Avis, C. C., Lorre, J. J., and Garneau, G. W., 1980, *J. British Interplanetary Society*, **33**, 315.

Jones, B., and Puetter, R., 1993, *Proc. SPIE, Infrared Detectors and Instrumentation*, **1946**, 610.

Karkoschka, E., 1994, *Icarus,* **111**, 174.

Karkoschka, E., 1997, `http://www.stsci.edu/ftp/instrument_news/WFPC2/Wfpc2_phot/wpfc2_sol_phot.html`.

Khanna, R. K., Ospina, M. J., and Zhao, G., 1988, *Icarus,* **73**, 527.

Kuiper, G. P., 1949, *Astrophys. J.,* **109**, 540.

Labs, D., and Neckel, H., 1968, *Z. Astrophys.*, **69**, 1.

Lindal, G. F., Lyons, J. R., Sweetnam, D. N., Eshleman, V. R., Hinson, D. P., and Tyler, G. L., 1987, *J. Geophys. Res.,* **92**, 14,987.

Lockwood, G. W., 1997, *Bull. Am. Astron. Soc.,* **29**, 993.

Lockwood, G. W., Lutz, B. L., Thompson, D. T., and Warnock III, A., 1983, *Astrophys. J.,* **266**, 402.

Lunine, J. I., 1993, *Ann. Rev. Astron. Astrophys.*, **31**, 217.

Marley, M. S., McKay, C. P., and Pollack, J. B., 1997, *Icarus,* submitted.

McKay, C. P., Pollack, J. B., and Courtin, R., 1989, *Icarus,* **80**, 23.

Muhleman, D. O., and Berge, G. L., 1991, *Icarus,* **92**, 263.

Neckel, H., and Labs, D., 1984, *Solar Phys.*, **90**, 90,205.

Nicholson, P. D., and Jones, T. J., 1980, *Icarus,* **42**, 54.

Orton, G. S., Aitken, D. K., Smith, C., Roche, P. F., Caldwell, J., and Snyder, R., 1987, *Icarus,* **70**, 1.

Orton, G. S., Baines, K. H., Caldwell, J., Romani, P., Tokunaga, A. T., and West, R. A., 1990, *Icarus,* **85**, 257.

Orton, G. S., Griffin, M. J., Ade, P. A. R., Nolt, I. G., Radostitz, J. V., Robson, R. I., and Gear, W. K., 1986, *Icarus,* **67**, 289.

Pearl, J., Ngoh, M., Ospina, M., and Khanna, R., 1991, *J. Geophys. Res.,* **96**, 17,477.

Pearl, J. C., Conrath, B. J., Hanel, R. A., and Pirraglia, J. A., 1990, *Icarus,* **84**, 12.

Pollack, J. B., Rages, K., Baines, K. H., Bergstralh, J. T., Wenkert, D., and Danielson, G. E., 1986, *Icarus,* **65**, 442.

Pollack, J. B., Rages, K., Pope, S. K., Tomasko, M. G., Romani, P. N., and Atreya, S. K., 1987, *J. Geophys. Res.,* **92**, 15,037.

Prinn, R. G., and Lewis, S. J., 1983, *Astrophys. J.,* **179**, 333.

Pryor, W. R., West, R. A., and Simmons, K. E., 1997, *Icarus,* **127**, 508.

Rages, K, Pollack, J. B., Tomasko, M. G., and Doose, L. R., 1991, *Icarus,* **89**, 359.

Savage, B. D., and Caldwell, J. J., 1974, *Astrophys. J.,* **187**, 197.

Smith, B. A., Soderblum, L. A., Beebe, R., Bliss, D., Brown, R. H., Collins, S. A., Boyce, J. M., Briggs, G. A., Brahic, A., Cuzzi, J. N., and Morrison, D. 1986, *Science,* **233**, 43.

Smith, W. H., Macy, W., and Pilcher, C. B., 1980, *Icarus,* **43**, 153.

Strong, K., Taylor, F. W., Calcutt, S. B., Remedios, J. J., and Ballard, J., 1993, *J. Quant. Spectrosc. Radiat. Trans.*, **50**, 363.

Thompson, R. I., 1993, *Proc. SPIE, Instrumentation in Astronomy VIII,* **2198**, 1202.

Toon, O. B., McKay, C. P., Ackerman, T. P., and Santhanam, K., 1989, *J. Geophys. Res.,* **94**, 16,287.

Trafton, L. M., 1976, *Astron. Astrophys.,* **207**, 1007.

Trafton, L. M., 1987, *Icarus,* **70**, 13.

Trauger, J. T., and Bergstralh, J. T., 1981, *Bull. Am. Astron. Soc.,* **13**, 732.

Wallace, L., 1980, *Icarus,* **43**, 231.

Walter, C. M., and Marley, M. S., 1995, *Bull. Am. Astron. Soc.,* **27**, 1089.

Walter, C. M., Marley, M. S., Hunten, D. M., Sprague, A. L., Wells, W. K., Dayal, A., Hoffmann, W. F., Sykes, M. V., Deutsch, L. K., Fazio, G. G., and Hora, J. L., 1996, *Icarus,* **121**, 341.

Weidenschilling, S. J., and Lewis, J. S., 1973, *Icarus,* **20**, 465.

Werner, M. W., 1995, in *Airborne astronomy symposium on the galactic ecosystem: from gas to stars to dust*, Eds. M. R. Haas, J. A. Davidson, and E. F. Erickson, 701, Astronomical Society of the Pacific, San Francisco.

West, R. A., Baines, K. H., and Pollack, J. B., 1991, in *Uranus*, Eds. J. T. Bergstralh, E. D. Miner, and M. S. Matthews, 296, Univ. of Arizona Press, Tucson.

Zellner, B., Seidelmann, P. K., Pascu, D., Kowal, C., Wells, E., and Currie, D., 1994, *Bull. Am. Astron. Soc.,* **26**, 1163.

Zheng, C., and Borysow, A., 1995, *Icarus,* **113**, 84.

Appendix A

The Uranian Atmosphere Model

The atmosphere model used in chapter 3 is given below. The first table gives the pressure and temperature in the Uranian atmosphere from the Voyager 2 RSS occulation experiment (Lindal et al. 1987). In the second table is the characteristics of the Uranian haze determined from high phase angle Voyager 2 imaging (Rages et al. 1991). For each layer is given the pressure at the top and bottom, the height above the optically thick lower cloud, the column density in that layer, and the mean particle size and log-normal dispersion σ.

Table A.1: Voyager 2 occultation results

Pressure (bar)	Temperature (K)
4.00000E-05	130.
5.00000E-04	98.0000
8.00000E-04	76.3000
1.40000E-03	72.9122
2.40000E-03	66.9569
4.10000E-03	68.5185
7.00000E-03	64.0233
1.19000E-02	65.3555
2.03000E-02	58.8650
3.46000E-02	54.3255
5.90000E-02	53.8148
1.00500E-01	53.4966
0.171300	53.5254
0.292100	54.6702
0.497900	62.1293
0.608100	64.3560
0.742700	70.1039
0.907200	75.3328
1.10800	80.7672
1.35340	83.9635
1.65300	89.4127
2.01900	100.5290
2.46600	105.913
3.01190	111.639
3.67880	117.648
4.49330	123.942
5.48810	130.520
6.70320	137.383
8.18730	144.531
10.00000	151.966
12.0000	158.991
14.0000	165.114
16.0000	170.558
18.0000	175.469
20.0000	179.952

Table A.2: Rages haze model

P_{top}	P_{bottom}	Height (km)	N (cm^{-2})	r (μm)	σ
0.5010E-01	0.6610E-01	343.0	0.1072E+07	0.2054E-01	1.060
0.6610E-01	0.8710E-01	329.0	0.2804E+07	0.2083E-01	1.062
0.8710E-01	0.1150	315.0	0.5798E+07	0.2099E-01	1.067
0.1150	0.1510	300.0	0.8990E+07	0.2055E-01	1.014
0.1510	0.2000	286.0	0.1362E+08	0.2073E-01	1.023
0.2000	0.2630	273.0	0.1718E+08	0.2143E-01	1.082
0.2630	0.3470	260.0	0.2095E+08	0.2185E-01	1.070
0.3470	0.4570	247.0	0.2342E+08	0.2141E-01	1.104
0.4570	0.6030	235.0	0.1720E+08	0.2528E-01	1.333
0.6030	0.7940	224.0	0.1491E+08	0.3063E-01	1.368
0.7940	1.050	213.0	0.1190E+08	0.3629E-01	1.369
1.050	1.380	203.0	0.1020E+08	0.4247E-01	1.367
1.380	1.820	194.0	0.8101E+07	0.4905E-01	1.361
1.820	2.400	185.0	0.6499E+07	0.5596E-01	1.354
2.400	3.160	177.0	0.5011E+07	0.7760E-01	1.368
3.160	4.170	169.0	0.4426E+07	0.9830E-01	1.357
4.170	5.500	162.0	0.4018E+07	0.1059	1.357
5.500	7.240	155.0	0.4030E+07	0.1151	1.354
7.240	9.550	148.0	0.3898E+07	0.1260	1.347
9.550	12.60	141.0	0.3213E+07	0.1372	1.337
12.60	16.60	135.0	0.3575E+07	0.1518	1.325
16.60	21.90	128.0	0.2996E+07	0.1665	1.312
21.90	28.80	122.0	0.2905E+07	0.1820	1.302
28.80	38.00	116.0	0.2829E+07	0.1977	1.294
38.00	50.10	110.0	0.2756E+07	0.2137	1.287
50.10	66.10	104.0	0.2677E+07	0.2305	1.280
66.10	87.10	98.00	0.2348E+07	0.2465	1.274
87.10	115.0	93.00	0.2497E+07	0.2641	1.268
115.0	151.0	87.00	0.2372E+07	0.2815	1.261
151.0	200.0	81.00	0.2350E+07	0.2991	1.256
200.0	263.0	75.00	0.2212E+07	0.3167	1.252
263.0	347.0	69.00	0.2151E+07	0.3348	1.249
347.0	457.0	63.00	0.1992E+07	0.3528	1.243
457.0	603.0	57.00	0.1892E+07	0.3712	1.240
603.0	794.0	50.00	0.1796E+07	0.3909	1.240
794.0	1050.	42.00	0.1699E+07	0.4125	1.241
1050.	1380.	34.00	0.1490E+07	0.4348	1.241
1380.	1820.	25.00	0.1342E+07	0.4566	1.240
1820.	2400.	16.00	0.1238E+07	0.4786	1.241
2400.	3160.	5.000	0.1128E+07	0.5007	1.244

Appendix B

Viewing Geometry

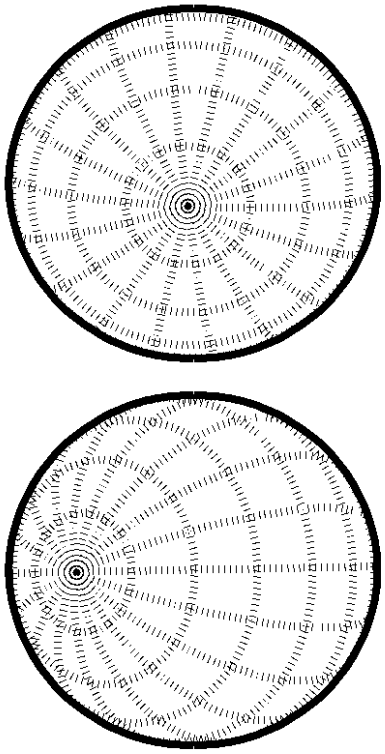

Figure B.1: The figure shows Uranus as seen from the earth in (top) January 1986 (when visited by Voyager 2) and (bottom) August 1995. The south pole is clearly visible as the locus of all meridians in both diagrams, with the grid markings representing 20° in latitude and longitude. The cloud asymmetry extends from the pole to ≈ -40° latitude

Appendix C

Thermal Atmosphere Model

The atmosphere model used in chapter 5 is given below. In order are the pressure of the levels used in the atmosphere, the spectral intervals used in computing deposition of solar flux, and the used distribution of the most common hydrocarbons in the atmosphere at the average pressure in each layer.

Table C.1: Pressure levels

Level	Pressure (bar)	Level	Pressure (bar)
43	2.000E+01	21	8.813E-03
42	1.482E+01	20	5.943E-03
41	1.098E+01	19	4.008E-03
40	8.131E+00	18	2.703E-03
39	6.024E+00	17	1.823E-03
38	4.463E+00	16	1.229E-03
37	3.306E+00	15	8.291E-04
36	2.449E+00	14	5.591E-04
35	1.814E+00	13	3.771E-04
34	1.344E+00	12	2.543E-04
33	9.957E-01	11	1.715E-04
32	6.715E-01	10	1.157E-04
31	4.529E-01	9	7.800E-05
30	3.054E-01	8	5.260E-05
29	2.060E-01	7	3.547E-05
28	1.389E-01	6	2.392E-05
27	9.368E-02	5	1.613E-05
26	6.318E-02	4	8.000E-06
25	4.261E-02	3	4.000E-06
24	2.873E-02	2	3.000E-06
23	1.938E-02	1	2.500E-06
22	1.307E-02		

Table C.2: Optical and near-infrared spectrum interval centers

Interval	Wavelength (μm)
1	0.275
2	0.325
3	0.375
4	0.425
5	0.475
6	0.525
7	0.575
8	0.640
9	0.715
10	0.789
11	0.850
12	0.891
13	0.935
14	0.998
15	1.073
16	1.144
17	1.213
18	1.292
19	1.381
20	1.484
21	1.580
22	1.678
23	1.779
24	1.899
25	2.015
26	2.077
27	2.133
28	2.201
29	2.264
30	2.370
31	2.509
32	2.857
33	3.201
34	3.335
35	3.709
36	4.222

Table C.3: Model hydrocarbon mixing ratios

Average Pressure (bars)	CH_4	C_2H_2	C_2H_6
0.274E-05	2.0E-07	1.3E-18	2.9E-17
0.348E-05	2.3E-07	5.5E-18	9.5E-17
0.583E-05	3.2E-07	1.7E-16	1.6E-15
0.117E-04	5.1E-07	8.7E-15	4.3E-14
0.198E-04	7.3E-07	1.1E-13	3.8E-13
0.294E-04	9.5E-07	9.9E-13	2.4E-12
0.436E-04	1.2E-06	9.1E-12	1.5E-11
0.647E-04	1.6E-06	8.3E-11	9.9E-11
0.959E-04	2.1E-06	7.6E-10	6.4E-10
0.142E-03	2.7E-06	7.0E-09	4.1E-09
0.211E-03	3.5E-06	4.9E-08	2.5E-08
0.313E-03	4.6E-06	1.0E-07	4.4E-08
0.464E-03	6.0E-06	1.0E-07	3.5E-08
0.687E-03	7.8E-06	7.7E-08	2.8E-08
0.102E-02	9.4E-06	3.5E-08	2.2E-08
0.151E-02	1.0E-05	1.1E-08	1.7E-08
0.224E-02	1.0E-05	3.7E-09	1.4E-08
0.332E-02	1.0E-05	1.2E-09	1.1E-08
0.493E-02	1.0E-05	3.9E-10	8.5E-09
0.731E-02	1.0E-05	1.3E-10	6.7E-09
0.108E-01	1.0E-05	4.1E-11	3.3E-09
0.161E-01	1.0E-05	1.3E-11	6.1E-10
0.238E-01	1.0E-05	4.4E-12	5.2E-11

Average Pressure (bars)	CH4	C2H2	C2H6
0.353E-01	1.0E-05	1.4E-12	4.3E-12
0.524E-01	1.0E-05	4.6E-13	3.6E-13
0.777E-01	1.0E-05	1.5E-13	3.0E-14
0.115E+00	1.0E-05	4.9E-14	2.6E-15
0.171E+00	1.0E-05	4.9E-14	2.6E-15
0.253E+00	1.0E-05	4.9E-14	2.6E-15
0.376E+00	1.6E-05	4.9E-14	2.6E-15
0.557E+00	8.3E-05	4.9E-14	2.6E-15
0.826E+00	6.2E-04	4.9E-14	2.6E-15
0.116E+01	2.6E-03	4.9E-14	2.6E-15
0.157E+01	7.3E-03	4.9E-14	2.6E-15
0.212E+01	1.3E-02	4.9E-14	2.6E-15
0.286E+01	1.6E-02	4.9E-14	2.6E-15
0.386E+01	1.6E-02	4.9E-14	2.6E-15
0.521E+01	1.6E-02	4.9E-14	2.6E-15
0.704E+01	1.6E-02	4.9E-14	2.6E-15
0.950E+01	1.6E-02	4.9E-14	2.6E-15
0.128E+02	1.6E-02	4.9E-14	2.6E-15
0.173E+02	1.6E-02	4.9E-14	2.6E-15